Title: Astrocytic hemoglobin is an H_2O_2-decomposing peroxidase and therapeutic target for Alzheimer's disease

Authors: Woojin Won[1]†, Elijah Hwejin Lee[2,3]†, Lizaveta Gotina[2,3], Heejung Chun[1], Uiyeol Park[2], Daeun Kim[1], Tai Young Kim[1], Jiwon Choi[2], Yoowon Kim[2], Sun Jun Park[2,3], Mridula Bhalla[1,4], Jiwoon Lim[1,4], Jong-Hyun Park[2,3], Soo-Jin Oh[2], Hoon Ryu[2,3], Ae Nim Pae[2,3], Ki Duk Park[2,3]* and C. Justin Lee[1,4]*

Affiliations:

[1]Center for Cognition and Sociality, Institute for Basic Science (IBS); Daejeon 34126, Republic of Korea.

[2]Center for Brain Disorders, Brain Science Institute, Korea Institute of Science and Technology (KIST); Seoul, 02792, Republic of Korea.

[3]Division of Bio-Medical Science & Technology, University of Science and Technology (UST); Daejeon, 34113, Republic of Korea.

[4]IBS School, University of Science and Technology (UST); Daejeon 34113, South Korea.

† These authors contributed equally to this work.

*Correspondence to:

C. Justin Lee, PhD
E-mail: cjl@ibs.re.kr
Center for Cognition and Sociality, Institute for Basic Science (IBS); Daejeon 34126, Republic of Korea.

Ki Duk Park, PhD
E-mail: kdpark@kist.re.kr
Center for Brain Disorders, Brain Science Institute, Korea Institute of Science and Technology (KIST); Seoul, 02792, Republic of Korea

ABSTRACT

Hemoglobin (Hb) is well-known for transporting oxygen in red blood cells within blood vessels. However, its role in the brain has been largely unknown. Here, we report that Hb, found in hippocampal astrocytes of both animal models and Alzheimer's disease (AD) patients, displays significant antioxidant effects through its H_2O_2-decomposing peroxidase activity. To counteract the harmful effects of aberrant H_2O_2-production in AD, we developed KDS12025, a BBB-permeable small molecule that effectively enhances the H_2O_2-decomposing activity of Hb by 100-fold, even at very low level of Hb. KDS12025 reduces H_2O_2 in astrocytes and reverses memory impairment in AD models. Gene-silencing of Hbβ abrogates the enhancing effect of KDS12025 in both culture and animal models of AD. We propose boosting Hb's peroxidase activity as a new therapeutic approach for AD treatment.

Introduction

Hemoglobin (Hb) is a well-known heme-containing protein recognized for its role in transporting oxygen and carbon dioxide in the bloodstream (*1*). Intriguingly, Hb has also been observed in the brain, but its function remains enigmatic (*2, 3*). When cell-free Hb leaks out during hemorrhage events, it exacerbates neurotoxicity by releasing iron and heme, which lead to inflammation and the generation of free radicals (*1, 4*). Yet, in cultured astrocytes, the administration of Hb paradoxically exerts a protective role, potentially suppressing amyloid β (Aβ)-mediated inflammatory activation and oxidative stress (*5, 6*). While the cellular and molecular mechanism underlying the antioxidant effect is unidentified in the brain, several studies conducted outside the brain have reported Hb's peroxidase-like activities in the presence of H_2O_2 (*7-9*). This enzymatic function raises the possibility that Hb could act as an H_2O_2-decomposing peroxidase within the brain.

Our recent research highlights the aberrant H_2O_2 production by severe reactive astrocytes, a pathological form of astrocytes, as a key factor for the neurodegeneration in Alzheimer's disease (AD) (*10, 11*). This excessive H_2O_2 not only contributes to the cellular and molecular hallmarks of neurodegenerative diseases such as AD but also poses a therapeutic challenge, as it demands a selective reduction of excessive H_2O_2 without disrupting the delicate redox balance essential for normal brain function (*12, 13*). To address this challenge, we have been advocating for a paradigm shift from traditional Aβ-focused interventions to those targeting the oxidative stress implicated in AD, specifically by modulating the level of astrocytic excessive H_2O_2 (*10*). However, conventional antioxidants fall short due to their high reactivity, impractically high concentration requirements, poor cellular uptake, and low bioavailability to modulate astrocytic excessive H_2O_2 (*13*). Previously, we employed 2-hydroxy-5-[2-(4-trifluoromethyl-phenyl)-ethylamino]-benzoic acid (HTPEB) (*10, 14*) as a potent H_2O_2 scavenger in astrocyte, but its cellular and molecular mechanism was not fully identified. Our previous work using plant-derived horseradish peroxides (HRP)-based H_2O_2 assay with HTPEB hinted at its potential as a chemical enhancer of peroxidase activity (*10*), paving the way for the development of new chemical enhancers for astrocytic peroxidase, Hb in neurodegenerative diseases. In this study, we set out to elucidate the astrocytic Hb's peroxidase activity and develop a chemical enhancer to enhance its activity as a novel strategy to treat neurodegenerative diseases including AD.

Hemoglobin shows H_2O_2-decomposing activity

To test whether the Hb has an H_2O_2-decomposing activity, we performed well-established H_2O_2 assays using Amplex Red or ROS-Glo (Fig. 1, A and B). HTPEB showed H_2O_2 scavenging in the Amplex Red assay, which includes HRP (Fig. 1, A and C). However, HTPEB's H_2O_2 scavenging activity was not demonstrated in the ROS-Glo as in the Amplex Red assay, which does not include HRP (Fig. 1, C and D). These results imply that HTPEB was not a direct H_2O_2 scavenger, and its activity was dependent on the presence of an enzyme. The discrepancy between the two assays led us to investigate the role of HRP in the observed activity. Replenishing HRP, whose histidine residue interacts with the heme group (*15*) to form a transitional complex with H_2O_2 (*16*), to ROS-Glo assay fully restored HTPEB's H_2O_2 decomposition (Fig. 1E), indicating that HTPEB facilitates HRP-mediated H_2O_2 breakdown. The half-maximal effective concentration (EC_{50}) of HRP was considerably lower with HTPEB (0.028 U/ml) compared to HRP alone (0.062 U/ml) (Fig. 1F). Also, the activity rate increased from 0.0076 to 0.016 U/s, doubling its enzymatic speed with HTPEB (Fig. 1F). H_2O_2 reduction time (τ) decreased from 13.7 to 8.57 minutes (Fig. 1G). These findings indicate that HTPEB is a chemical enhancer of peroxidase activity and requires HRP for its action.

While HRP is a plant-derived heme-containing peroxidase commonly used in research, it does not exist in animals (*15, 17*). Therefore, we examined whether animal heme-containing enzymes such as bovine catalase (CAT), bovine glutathione peroxidase (GPx), and human Hb (*18, 19*) could mimic the HTPEB-mediated enhancement of HRP's peroxidase activity. To test this idea, we substituted HRP with Hb, CAT, and GPx in H_2O_2 assays. Overall, we observed that Hb, a tetrameric heme-containing protein, significantly facilitated H_2O_2 decomposition 2-fold with HTPEB, shifting its EC_{50} value from 7.96 to 3.97 U/ml (Fig. 1H). Contrarily, CAT, a heme-containing enzyme known for its robust H_2O_2 decomposition (*19*), did not show enhancement with HTPEB (Fig. 1I). This could be due to its inherent maximal catalytic activity, potentially linked to the presence of a tyrosine residue (*20, 21*). GPx, a heme-lacking and selenium-containing peroxidase (*19*), interestingly showed a decrease in activity in the presence of HTPEB, possibly due to HTPEB's competition with GPx's substrate glutathione, highlighting the complexity of enzyme-drug interactions (Fig. 1J). These results indicate that HTPEB enhances the H_2O_2-decomposing activity of heme-containing proteins like Hb. Taken together, these results strongly suggest a peroxidase-like activity of Hb.

Development of a potent BBB-permeable H_2O_2-decomposing chemical enhancer for Hb

We found that HTPEB enhanced the peroxidase-like activity of Hb, but also showed poor blood-brain barrier (BBB)-permeability and low solubility in aqueous solutions (table S3). Therefore, we conducted a systematic investigation of the relationship between different functional groups within HTPEB and their roles in modulating the compound's activity to overcome the limitation of HTPEB by developing improved small molecules. HTPEB, consisting of a salicylic acid moiety connected to 2-(4-(trifluoromethyl)phenyl)ethylamine (table S1), was analyzed alongside salicylic acid, p-cresotic acid, mesalazine, and 2-(4-(trifluoromethyl)phenyl)ethylamine for their effects on Hb in a dose-response manner (table S1). Notably, only mesalazine showed a dose-dependent effect, suggesting that its pharmacological activity is related to the amine functional group with a lone pair of electrons. This result suggests that the electron-donating amine group directly bound to an aromatic ring may be a critical determinant in the pharmacological activity of HTPEB, offering insights into the structural basis for its potency.

To develop a small molecule that enhances pharmacological properties and amplifies Hb peroxidase-like activity, we synthesized a series of strategically designed HTPEB derivatives, all retaining the essential *N*-phenethylaniline core (fig. S1). By modifying the carboxylic acid and hydroxyl groups with an electron-donating methylamine group, we calibrated the compound's activity to specifically enhance the peroxidase-like action of Hb (table S2 and fig. S2), resulting in KDS12017 (compound 8a) with a higher potency (EC_{50} = 0.09 μM) in comparison with HTPEB (EC_{50} = 0.15 μM) (Fig. 1, K and L). Further, by substituting the electron-pulling trifluoromethyl for an electron-pushing ortho-methoxy group, KDS12025 emerged as the most potent derivative (EC_{50} = 0.04 μM), with a 5-fold increase in potency over HTPEB (Fig. 1, K and L). Unlike the direct H_2O_2 scavengers like sodium pyruvate (*22*), these compounds did not directly degrade H_2O_2 in the absence of HRP (Fig. 1M). Through a structure-activity relationship analysis, we developed KDS12025 as the most potent enhancer of the peroxidase-like activity of Hb.

Next, we conducted an isothermal calorimetric (ITC) assay to assess the binding between Hb and the most active compound KDS12025. The result revealed a compound binding energy (ΔG_{bind}) of -7.07 kcal/mol, which is mainly due to enthalpic contributions like hydrogen bonding and hydrophobic interactions, suggesting a significant binding affinity between Hb and KDS12025 (Fig. 1N). Complementary molecular docking analysis suggested a strong interaction (ΔG_{bind} of -16.5 kcal/mol) between KDS12025 and the Hbβ subunit within a wide

134 cleft next to the heme molecule, formed by residues 42-50 (Fig. 1O). Numerous hydrophobic
135 interactions of the methoxy group and the presence of a hydrogen bonding network between
136 the *N*1 amine group, distal histidine H63, and heme point to the importance of these groups for
137 the molecule's activity (Fig. 1O). Potent compounds HTPEB, KDS12008, and KDS12017
138 were also predicted to bind to this Hbβ-specific site (ΔG_{bind} of -13.27, -12.99 and -14.28
139 kcal/mol, respectively) (fig. S3, A and B). Conversely, the derivatives that showed low potency
140 in the enzyme assays (table S2) demonstrated significantly weaker ΔG_{bind} (fig. S3, C to H). In
141 the case of HRP binding mode prediction, KDS12025 and HTPEB fit in the narrow catalytic
142 pocket (fig. S4). Collectively, the results of molecular docking and enzyme assays demonstrate
143 that *N*-phenethylaniline small molecules retain the crucial amine group function and potently
144 bind to Hbβ.

145 We further evaluated the pharmacology of KDS12025, noting its high bioavailability of
146 87.43% and significant BBB-permeability, confirmed by parallel artificial membrane
147 permeability assay (PAMPA) (*23*) with a permeability of $P_e = 67.43 \times 10^{-6}$ cm/sec (table S3).
148 We examined the 97 kinases (KINOMEscan) and off-target selectivity of KDS12025 with 87
149 primary molecular targets including G-protein coupled receptors (GPCRs), kinases, non-kinase
150 enzymes, and various ion channels. An evaluation of off-target selectivity revealed favorable
151 off-target selectivity at 1 μM KDS12025 (fig. S5). The off-target selectivity of KDS12025,
152 coupled with its potent antioxidant activity, shows a high possibility for reduced side effects
153 commonly associated with highly reactive ROS scavengers. Taken together, these results
154 indicate that KDS12025 shows favorable drug-like properties.

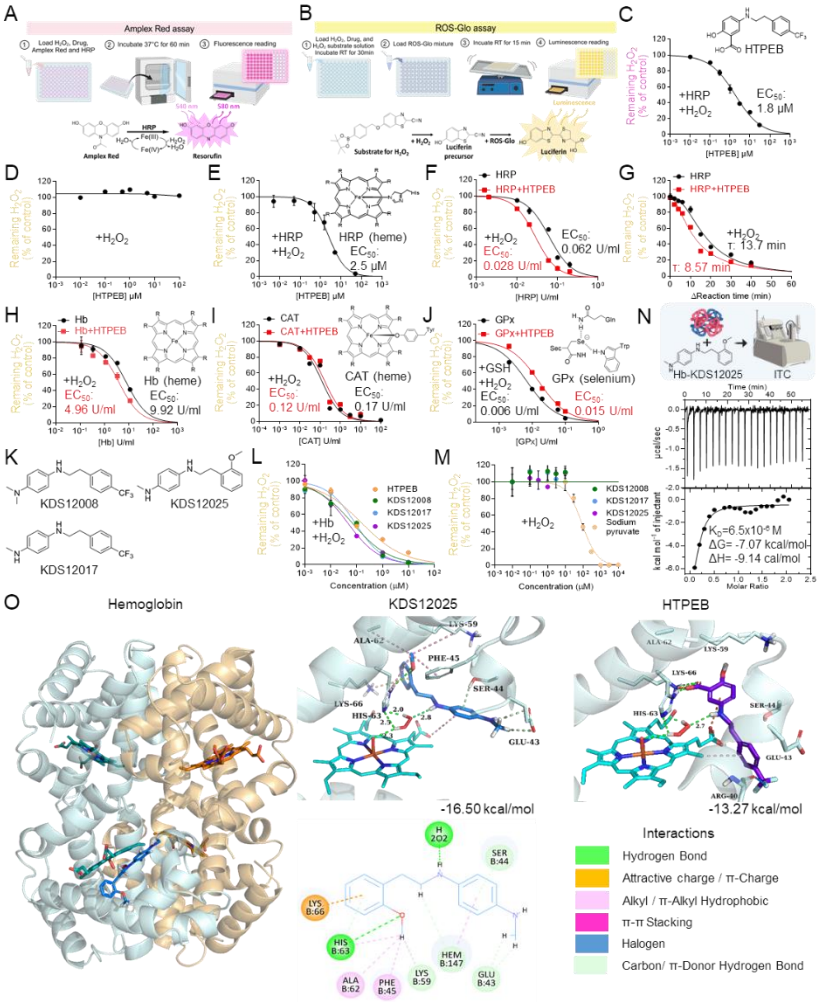

Fig. 1. Hemoglobin's peroxidase-like activity: developing an enhancer for decomposition of H_2O_2. (A) Schematic diagram of HRP-dependent Amplex Red H_2O_2 assay. **(B)** Schematic diagram of ROS-Glo H_2O_2 assay (HRP-independent). **(C)** The dose-dependent response curve of an HTPEB in Amplex Red H_2O_2 assay. **(D)** The dose-dependent response curve of an HTPEB in ROS-Glo H_2O_2 assay without HRP **(E)** The dose-dependent response curve of HTPEB in ROS-Glo assay with the same amount of HRP as used in the Amplex Red assay. **(F)** The dose-dependent response curve of HRP in ROS-Glo H_2O_2 assay with or without an HTPEB. **(G)** Reaction time-dependent response curve in ROS-Glo H_2O_2 assay with and without an HTPEB. **(H to J)** The dose-dependent response curve of various endogenous peroxidase families (Hb, CAT, GPx) in ROS-Glo H_2O_2 assay with or without an HTPEB. **(K)** Chemical structure of KDS derivatives, KDS12008, 17, and 25. **(L)** The dose-dependent response curve of HTPEB, KDS12008, 17, and 25 in ROS-Glo H_2O_2 assay with Hb. **(M)** The dose-dependent response curve of KDS12008, 17, 25, and sodium pyruvate in ROS-Glo H_2O_2 assay to assess direct H_2O_2 scavenging. **(N)** ITC analysis depicting the binding interaction between Hb and KDS12025. **(O)** Binding mode and calculated binding energy (ΔG_{bind}) of KDS12025 and HTPEB with Hb proposed by docking simulations.

KDS12025 enhances Hb peroxidase activity

We quantified the enhancement of peroxidase activity in HRP and Hb by KDS12025, measuring the fold increase over a 30-minute enzyme assay. Remarkably, KDS12025 significantly facilitated HRP and Hb enzymatic activities to a 5-fold increase over the vehicle, outperforming HTPEB's 3-fold enhancement, suggesting that KDS12025 has a potential capacity to promote peroxidase function (Fig. 2, A and B). Then, we investigated whether Hb possesses inherent peroxidase capabilities and the necessity of an enhancer like KDS12025 for this function, by allowing Hb and H_2O_2 to react before subsequently measuring the remaining H_2O_2 levels (Fig. 2C). At low concentrations (0.01~1U/ml), Hb showed no significant peroxidase activity, but preincubation with enhancers like KDS12025 and HTPEB significantly enhanced this function (Fig. 2D). As Hb's concentration increased (11 or 112 U/ml), its peroxidase activity improved, with KDS12025 showing greater potency than HTPEB (Fig. 2D). When comparing the H_2O_2 decomposition of Hb in a dose-dependent manner, we found that under the presence of KDS12025, Hb's EC_{50} for H_2O_2 decomposition was 4.7-fold lower than vehicle conditions (Fig. 2E). Furthermore, for the EC_{20}, the required Hb concentration was 98-fold lower with KDS1205 than vehicle conditions (Fig. 2E). Overall, these results indicate that KDS12025 remarkably enhances the H_2O_2-decomposing activity of Hb about 100-fold, boosting its peroxidase function even at extremely low Hb concentrations.

Subsequently, we tested whether Hb might also function as catalase, which decomposes H_2O_2 into oxygen and water, while also evaluating the role of KDS12025 in this biochemical reaction. We observed a strong oxygen liberation by CAT, but only a negligible oxygen liberation by Hb (fig. S6). To accurately measure the oxygen liberation, we captured and analyzed the liberated oxygen bubbles under the microscope (Fig. 2, F and G) and an inverted cylinder (Fig. 2H). We found that CAT produced numerous bubbles, whereas HRP and Hb produced a minimal number of oxygen bubbles (Fig. 2, F to H). Furthermore, neither KDS12025 nor HTPEB enhanced oxygen liberation by CAT (Fig. 2, F to H), aligning with the results from the enzyme activity assay (Fig. 1I). Taken together, these results demonstrate that Hb is not a catalase, and KDS12025 does not facilitate CAT activity.

Next, to assess whether KDS12025 interferes with Hb's oxygen-carrying capability in the blood, we examined respiratory functions in behaving mice, utilizing the automated phenotyping system for respiration and metabolism in mouse cages (Fig. 2I). This analysis showed that dose-dependent administration of KDS12025 did not affect oxygen consumption,

carbon dioxide production, or the volume respiratory exchange ratio (VCO_2/VO_2) of mice during both dark and light circadian cycles (Fig. 2, J to L). These results indicate that the oxygen- and carbon dioxide-carrying function of Hb was not affected by KDS12025. Also, there was no significant change in energy expenditure, total food consumption, or total drink consumption of mice (fig. S7). Taken together, these results imply that KDS12025 enhances Hb's peroxidase activity without altering the respiratory function of Hb or the overall metabolism in mice.

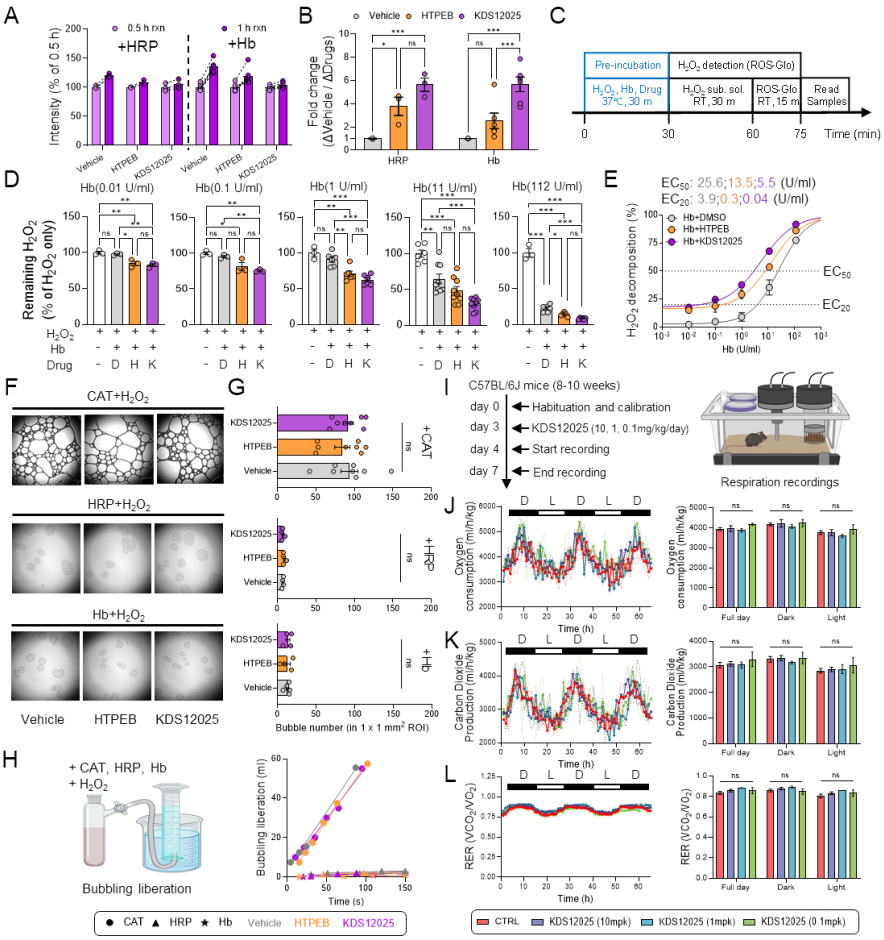

Fig. 2. KDS12025 enhances Hb peroxidase activity. (A) Paired comparison of H_2O_2 decomposition by HRP and Hb with drug treatment over 0.5 hours using ROS-Glo assay. **(B)** Fold change in H_2O_2-decomposing facilitation by HRP and Hb with drug treatment. **(C)** Timeline of Hb's intrinsic peroxidase function and drug enhancement effects. **(D)** Investigation of Hb's intrinsic peroxidase function with pre-incubation and the drug's role as a peroxidase enhancer at various Hb concentrations. Abbreviations indicate D, DMSO; H, HTPEB; K, KDS12025. **(E)** Dose-response curve of Hb's peroxidase activity indicating EC_{20} and EC_{50} values. **(F)** Observation of bubbles generated from CAT, HRP, and Hb in reaction with H_2O_2 and drugs (vehicle, HTPEB, KDS12025) under microscope. **(G)** Count the number of bubbles generated from CAT, HRP, and HB per 1 x 1 mm^2 area. **(H)** Schematic images of bubble liberation measurement from CAT, HRP, and Hb reaction with H_2O_2 and quantified bubble liberation volume with the cylinder. **(I)** Timeline of Phenomaster experiments with the administration of KDS12025 (10, 1, 0.1 mg/kg/day). **(J)** Measurement of oxygen consumption during the day (dark, 'D') and night (light, 'L') cycles, with a summary graph provided. **(K)** Measurement of carbon dioxide production and a summary graph. **(L)** Measurement of RER (VCO_2/VO_2) and a summary graph. Data are presented as the mean ± s.e.m. *P < 0.05, **P < 0.01, ***P < 0.001; ns, not significant. Additional statistics are provided in table S7.

193 **KDS12025 effectively reduces aberrant H_2O_2 *in vitro***

194 Since it has been previously reported that primary cultured astrocytes express Hb (*3*), we
195 tested whether the KDS12008, 17, and 25 enhance the H_2O_2-decomposing peroxidase activity
196 in cultured astrocytes. We used a fluorescence probe, 2′,7′-dichlorodihydrofluorescein diacetate
197 (DCFDA), and a newly developed H_2O_2-specific circularly permuted GFP sensor (oROS-G)
198 (*24*) to measure H_2O_2 levels in cultured astrocytes (fig. S8. A and B). To mimic AD-like
199 conditions characterized by aberrant H_2O_2 production, we treated the oligomerized $A\beta_{42}$ (Aβ)
200 in cultured astrocytes as previously described (*25, 26*). We found that Aβ treatment
201 significantly increased H_2O_2 in a concentration-dependent manner (Fig. 3, A and C), which was
202 effectively reduced by 10 μM concentration of the enhancers, especially KDS12025, which
203 demonstrated exceptional potency with an EC50 of 0.4 μM (Fig. 3, B and D). In contrast,
204 sodium pyruvate at 10 mM failed to reduce H_2O_2 levels (Fig. 3B). Moreover, we employed an
205 oROS-G sensor in astrocytes for 40 hours of continuous live-cell confocal imaging to assess
206 the time course of H_2O_2 after incubation with 5 μM Aβ or 180 μM putrescine, a precursor of
207 MAO-B-dependent production of H_2O_2 (*10, 27*) (fig. S8, C and D). The time course of Aβ- or
208 putrescine-induced H_2O_2 levels gradually peaked between 10 to 20 hours and was significantly
209 reduced by KDS12025 during this period to the control level (Fig. 3, E and F). Furthermore,
210 KDS12025 showed a significantly faster and more potent H_2O_2-decomposing effect compared
211 to sodium pyruvate (Fig. 3, E and F). These results indicate that KDS12025 is highly effective
212 in reducing Aβ-induced H_2O_2 levels to the control level *in vitro* within 24 hours.
213

214 **KDS12025 effectively alleviates AD pathology *in vivo***

215 We further investigated whether the KDS12008, 17, and 25 could alleviate AD symptoms
216 like astrogliosis and memory impairment in the APP/PS1 mouse model, a well-established
217 platform for studying AD (*28, 29*). Over 16 days, daily intraperitoneal (i.p.) injections of 3
218 mg/kg/day of these enhancers were evaluated using immunohistochemistry to quantify reactive
219 astrocytes and the passive avoidance test (PAT) for hippocampus-dependent memory (*30*) (Fig.
220 3G). Consistent with our previous works (*10, 31*), we observed a significant increase in reactive
221 astrocytes in the molecular layer of the hippocampal dentate gyrus (DG) of APP/PS1 mice,
222 which was significantly reduced by KDS12008, 17, and 25, indicating that these enhancers
223 effectively mitigate H_2O_2-induced reactive astrocytes (Fig. 3, H and I). We next conducted PAT
224 to examine whether KDS12008, 17, and 25 could recover memory impairment in APP/PS1

225 mice. We observed that APP/PS1 mice showed memory impairment, as shown by their shorter
226 latency to enter a dark room where they had previously received a foot shock (Fig. 3J). In
227 contrast, we found a significant memory improvement in APP/PS1 mice with KDS12008, 17,
228 and 25, among which KDS12025 was the most effective in alleviating memory impairment
229 (Fig. 3J). Furthermore, to examine the functional consequence of reactive astrocytes, we
230 measured γ-aminobutyric acid type A receptor ($GABA_AR$)-mediated tonic inhibition currents
231 in DG granule neurons, as described previously (*10, 32*). We found an increase of tonic GABA
232 current in APP/PS1 mice, as revealed by the $GABA_AR$ antagonist bicuculline (50 μM), which
233 was significantly reduced by KDS12025 treatment, bringing the tonic GABA current to control
234 levels (Fig. 3, K and L). In contrast, $GABA_AR$-mediated spontaneous inhibitory postsynaptic
235 currents showed no significant changes by KDS12025 (Fig. 3, M and N). A similar effect was
236 found in the treatment of 10 mg/kg/day KDS12025 (fig. S9). These results indicate that
237 KDS12025 is highly effective in reversing key pathological features of AD in mouse models,
238 including reactive astrocytes, aberrant tonic GABA current, and memory impairment.
239

240 **KDS12025 alleviates neurodegeneration and cognitive impairment in APP/PS1 mice with**
241 **focal GiD**

242 We next examined whether KDS12025 alleviates the neurodegeneration in the newly
243 developed AD mouse model. As previously described (*10, 11*), we employed focal diphtheria
244 toxin receptor (DTR)-expressing astrocytes in APP/PS1 mice to induce neurodegeneration,
245 which is typically absent in the APP/PS1 mouse model. We injected the AAV-GFAP104-DTR-
246 GFP virus into the CA1 of APP/PS1 mice (focal GiD; APP+DTR) or AAV-GFAP104-GFP virus
247 into the wild-type littermate mice (WT+GFP). After 5 weeks, we injected diphtheria toxin for
248 16 days to induce severe reactive astrocytes and neurodegeneration in CA1 pyramidal cells,
249 simultaneously treating the model mice with either KDS12025 or vehicle control (Fig. 3O). We
250 observed that severe reactive astrocytes were significantly increased in APP+DTR compared
251 to the WT+GFP (Fig. 3, P and Q). In contrast, KDS12025-treated APP+DTR mice
252 (APP+DTR+KDS) showed a significant reduction in reactive astrocytes (Fig. 3Q), suggesting
253 H_2O_2-dependent reactivity in their astrocytes. Furthermore, we found that the number of NeuN
254 was significantly decreased in APP+DTR mice compared to the WT+GFP (Fig. 3, P and R),
255 which indicates neurodegeneration in APP+DTR mice. In marked contrast, APP+DTR+KDS
256 mice showed a similar number of NeuN-positive cells as WT+GFP mice (Fig. 3R), indicating
257 that KDS12025 effectively protected neurodegeneration. KDS12025 also fully recovered

memory deficit and cognitive impairment in this model, without altering locomotor activity (Fig. 3, S and T, and fig. S10A). Taken together, these results propose KDS12025 as a highly potent and neuroprotective therapeutic for neurodegenerative diseases including AD.

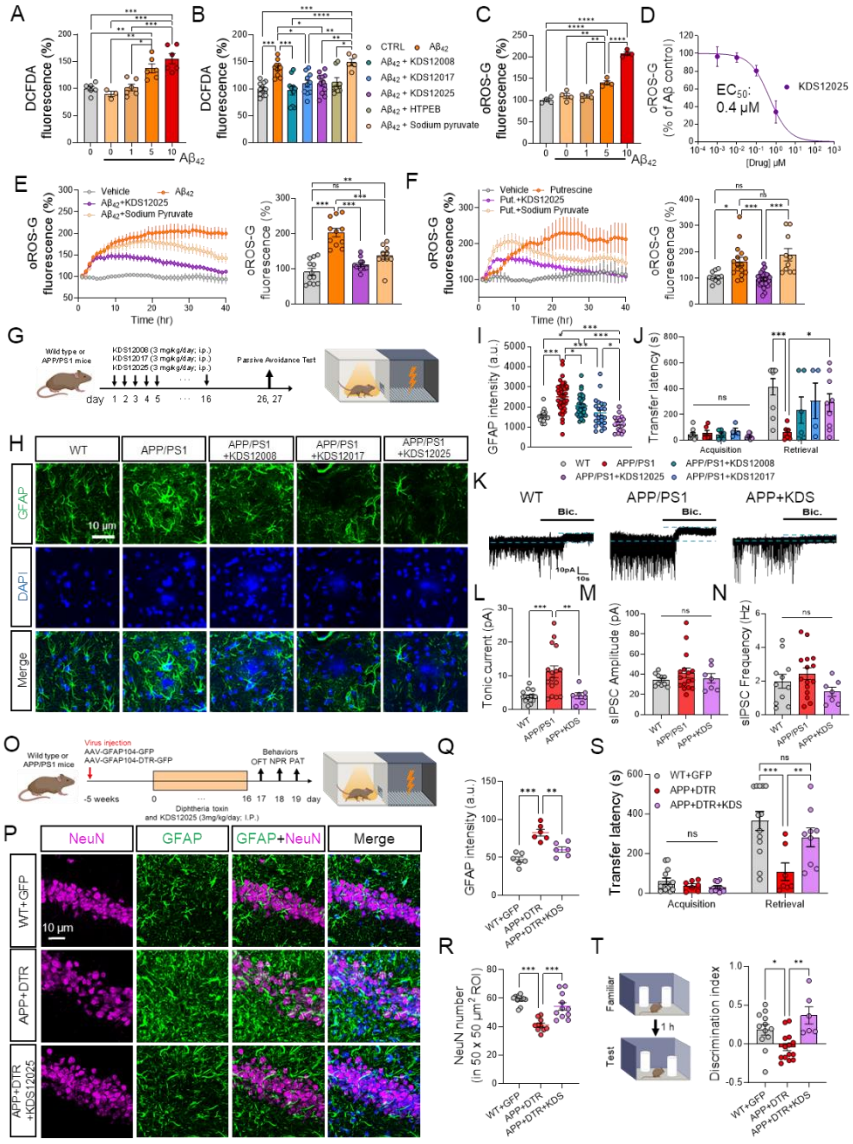

Fig. 3. KDS12025 alleviates aberrant H_2O_2 and AD symptoms, including neurodegeneration, astrogliosis, and memory impairment. **(A)** DCFDA-based H_2O_2 assay in Aβ-incubated cultured astrocytes at various concentrations. **(B)** Measurement of Aβ-induced H_2O_2 levels in cultured astrocytes after treating KDS12008 (10 μM), KDS12017 (10 μM), KDS12025 (10 μM), HTPEB (10 μM), or sodium pyruvate (10 mM). **(C)** cpGFP sensor-based H_2O_2 assay in Aβ-incubated cultured astrocytes **(D)** Dose-response curve of KDS12025 within $A\beta_{42}$ incubated astrocytes. **(E)** 40-hour continuous H_2O_2 imaging using oROS-G probe following oligomerized Aβ (5 μM) treatment, with the administration of KDS12025 (10 μM) and sodium pyruvate (1 mM). **(F)** Results of H_2O_2 measurement following putrescine (180 μM) treatment, with the administration of KDS12025 and sodium pyruvate. **(G)** Schematic timeline of experiment with the i.p. injection of KDS12008, KDS12017, or KDS12025 at 3 mg/kg/day for 16 days in APP/PS1 mice. **(H)** Representative immunostained images for GFAP and nearby Aβ. **(I)** Mean intensity of GFAP in GFAP-positive astrocytes area. **(J)** Transfer latency to enter the dark chamber during the acquisition and retrieval session in the PAT. **(K)** Representative trace of $GABA_AR$ mediated-tonic GABA current recorded from granule cells in the DG of APP/PS1 mice and administration of KDS12025 at 3mg/kg/day. **(L)** $GABA_AR$ mediated-tonic GABA current measured from DG granule cells. **(M and N)** Amplitude and frequency of spontaneous inhibitory postsynaptic currents (sIPSC) measured from granule cells in the DG of APP/PS1 mice. **(O)** Schematic diagram and experimental timeline for inducing reactive astrocytes in APP/PS1 mice using the focal expression of DTR and treatment with i.p. injection of KDS12025 (3 mg/kg) for 16 days. **(P)** Representative image of NeuN, and GFAP after KDS12025 treatment in the hippocampus CA1 of focal GiD mice. **(Q)** Mean intensity of GFAP intensity in focal GiD. **(R)** Quantification of neurodegeneration with NeuN number per 50 x 50 μm^2. **(S)** Latency to the dark chamber in focal GiD with KDS12025 treated mice. **(T)** Discrimination index in NPR test. Data are presented as the mean ± s.e.m Data are presented as the mean ± s.e.m. *P < 0.05, **P < 0.01, ***P < 0.001; ns, not significant. Additional statistics are provided in table S7.

261

Oral administration of KDS12025 also rescues AD pathologies

We further explored whether the oral administration route of KDS12025 is also effective in APP/PS1 mice. To examine the possibility, we administered KDS12025 at 3 mg/kg/day for 2 weeks through drinking water *ad libitum* (Fig. 4A). Using antibodies against GFAP, and GABA, we observed that KDS12025 treatment effectively reversed increased GFAP intensity and abnormal astrocytic GABA levels in APP/PS1 mouse (Fig. 4, B to D). Furthermore, we employed Sholl analysis to evaluate astrocyte reactivity based on morphological changes (Fig. 4E). This analysis demonstrated that several indices of reactive astrocytes, including a sum of intersections, ramification index, and ending radius, which were significantly upregulated in APP/PS1 mice, were effectively normalized by KDS12025 to wild-type levels (Fig. 4, E-I). These results show that oral administration of KDS12025 alleviates astrogliosis in the AD mouse model.

To assess the effect of oral administration of KDS12025 on AD symptoms, we employed electrophysiology to record the spike probability of DG granule cells, as previously conducted (*31*). While APP/PS1 mice exhibited a significantly reduced spike probability in response to perforant path stimulation, KDS12025 treatment significantly restored the spike probability to normal levels (Fig. 4, J and K). To investigate whether the oral administration of KDS12025 reverses memory impairment, we performed PAT and novel place recognition (NPR) tests (*33*). Oral administration of KDS12025 significantly reversed the memory impairment of APP/PS1 mice in PAT and NPR (Fig. 4, L and M), without affecting general locomotor activity (fig. S10B). Even at 0.1 mg/kg/day, oral administration of KDS12025 significantly reversed the memory impairment of the GiD mouse model of AD (*10*) (fig. S10C). These results indicate that even oral administration of KDS12025 effectively and potently rescues AD-like symptoms in the AD mouse models.

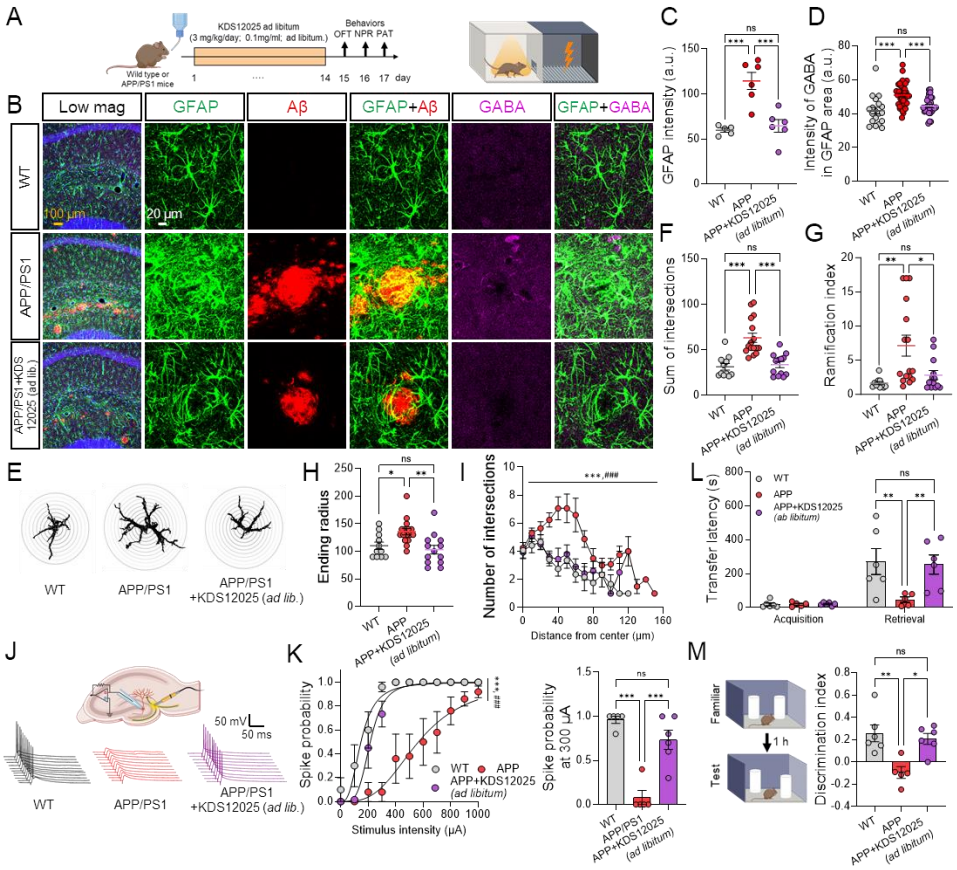

Fig. 4. Oral administration of KDS12025 rescues AD pathologies. (A) Schematic timeline of APP/PS1 mice with *ad libitum* administration of KDS12025 (3 mg/kg/day for 2 weeks), followed by performing OFT, NPR, and PAT. **(B)** Representative immunostaining images for GFAP, Aβ, and GABA after *ad libitum* administration of KDS12025. **(C)** Mean intensity of GFAP. **(D)** Mean intensity of GABA in GFAP-positive area. **(E)** Representative image for Sholl analysis of astrocytes in the stratum molecular layer from the GFAP images. **(F)** Summary graph showing the summation of intersections in astrocytes. **(G)** Summary graph showing the ramification index. **(H)** Summary graph showing the ending radius. **(I)** The number of intersections relative to their distance from the center. **(J)** Experimental schematic of measuring spike probability with electrical stimulation of perforant pathway stimulation after 2-week oral administration of KDS12025 and a representative trace of measurement of evoked EPSPs **(K)** Summary graph of Spike probability within stimulus intensity of 100-1000 μA (left) and comparison of spike probability at a stimulus intensity of 300 μA (right). **(L)** Transfer latency to enter the dark chamber during the acquisition and retrieval session in PAT. **(M)** Schematic protocol of the NPR test and summary bar graph showing the result of the NPR test. *P < 0.05, **P < 0.01, ***,$^{\#\#\#}$P < 0.001; ns, not significant. Additional statistics are provided in table S7.

Astrocytic hemoglobin β is necessary for the action of KDS12025 in the hippocampus

286 Building on these dramatic effects of KDS12025, our subsequent studies aimed to clarify
287 the molecular mechanism underlying KDS12025. We investigated if Hbβ in hippocampal
288 astrocytes is required for the action of KDS12025 in AD models. Initially, we transfected
289 primary cultured astrocytes with short hairpin RNA (shRNA) targeting Hbβ, aiming to inhibit
290 its expression and evaluate the consequent effects on KDS12025's activity using DCFDA
291 assays (Fig. 5A). We validated the efficacy of Hbβ knockdown using shRNA construct (fig.
292 S11, A and B). We observed an increase in aberrant H_2O_2 levels induced by Aβ in astrocytes
293 with the control Sc-shRNA, which was significantly reduced by KDS12025 application (Fig.
294 5B). In contrast, gene-silencing of Hbβ with shRNA while applying KDS12025 did not reduce
295 H_2O_2 levels, indicating that Hbβ is necessary for the mode of action of KDS12025 (Fig. 5B).
296 Interestingly, Hbβ-shRNA led to a significant increase in Aβ-induced H_2O_2 compared to Sc-
297 shRNA, suggesting that Hbβ knockdown exacerbates the aberrant H_2O_2 levels in cultured
298 astrocytes (Fig. 5B). These results indicate that Hbβ is critical for the H_2O_2-decomposing action
299 of KDS12025 in cultured astrocytes, and the lack of it makes the cells more vulnerable to
300 oxidative stress.

301 Subsequently, we tested whether Hbβ in hippocampal astrocytes is necessary for the
302 KDS12025's H_2O_2-decomposing effect *in vivo*. Before this assessment, we examined the Hbβ
303 expression in the hippocampus and found it present in astrocytes, which showed a significant
304 reduction in APP/PS1 mice (Fig. 5, C and D and fig. S10D). Interestingly, administration of
305 KDS12025 in APP/PS1 mice significantly recovered astrocytic Hbβ, suggesting that H_2O_2
306 negatively regulates the level of astrocytic Hbβ in AD (fig. S12). Then, we injected an AAV
307 carrying pSicoR-Hbβ-shRNA-mCherry into the stratum radiatum of the hippocampus in
308 APP/PS1 mice to examine the necessity of Hbβ in KDS12025's effect *in vivo*. (Fig. 5E). We
309 observed a significantly reduced astrocytic Hbβ in the APP/PS1 mice injected with Hbβ-
310 shRNA compared to those injected with control Sc-shRNA (Fig. 5, F and G and fig. S11C),
311 indicating a successful knockdown of Hbβ. While KDS12025 treatment reverted astrocyte
312 reactivity to wild-type levels in the Sc-shRNA group, these effects were abolished in the Hbβ-
313 shRNA group (Fig. 5, H to L). Moreover, the memory rescue effect of KDS12025 observed in
314 APP/PS1 mice was absent in the Hbβ-shRNA group (Fig. 5M). Altogether, these results
315 demonstrate that hippocampal astrocytic Hbβ is necessary for the action of KDS12025 in

316 alleviating astrogliosis and hippocampus-dependent memory impairment in the AD mouse
317 model.

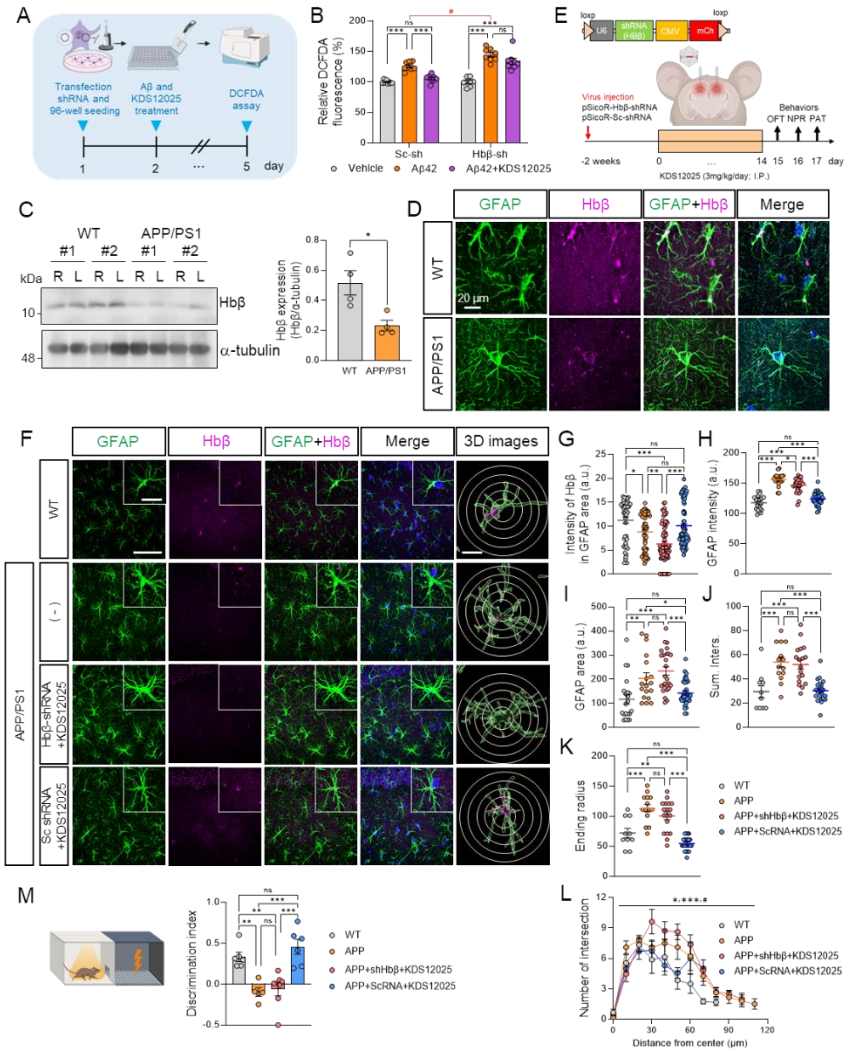

Fig. 5. Astrocytic Hbβ is necessary for the action of KDS12025 in the hippocampus. (A) Experimental timeline of transfection of Hbβ-shRNA, Aβ incubation, KDS12025 treatment. **(B)** Relative H_2O_2 levels in Sc-shRNA or Hbβ-shRNA transfected, oligomerized Aβ (5 μM)-treated cultured astrocytes with KDS12025 (10 μM). The '#' symbol (red color) indicates a comparison of Aβ-induced H_2O_2 between Sc-shRNA and Hbβ-shRNA. **(C)** Protein Quantification of Hbβ protein in the hippocampus of WT littermate and APP/PS1 mice **(D)** Representative Lattice-SIM images showing GFAP and Hbβ in the hippocampal regions of both WT littermate and APP/PS1 mice. **(E)** Schematic overview and timeline detailing the injection of an AAV carrying pSicoR-Hbβ-shRNA-mCherry or pSicoR-Sc-shRNA-mCherry into the stratum radiatum of the hippocampus in APP/PS1 mice. **(F)** Representative immunostaining confocal images of GFAP, and Hbβ and Sholl analysis images in the hippocampus, which were further analyzed using Imaris software. **(G)** Mean intensity of Hbβ in GFAP-positive area in the hippocampus. **(H)** Mean intenstiy of GFAP. **(I)** GFAP-positive area. **(J)** Summary graph showing the summation of intersections in astrocytes. **(K)** Summary graph showing the ending radius. **(L)** The number of intersections relative to their distance from the center. **(M)** Discrimination index from NPR test. Data are presented as the mean ± s.e.m. *,#P < 0.05, **P < 0.01, ***P < 0.001; ns, not significant. Additional statistics are provided in table S7.

Astrocytic Hbβ is decreased in the hippocampus of AD patients

To assess the clinical significance of the astrocytic Hbβ in AD patients, we performed immunohistochemistry on postmortem hippocampal tissues from both normal subjects and AD patients (Fig. 6, A and B). We observed astrocytic Hbβ in these tissues, highlighting its potential as a target for KDS12025 in clinics. Notably, there was a significant reduction in astrocytic Hbβ in the AD patients compared to normal subjects (Fig. 6, C and D). These findings parallel the reduced Hbβ expression found in the AD mouse model (Fig. 5), suggesting a similar pathological mechanism in human and animal models.

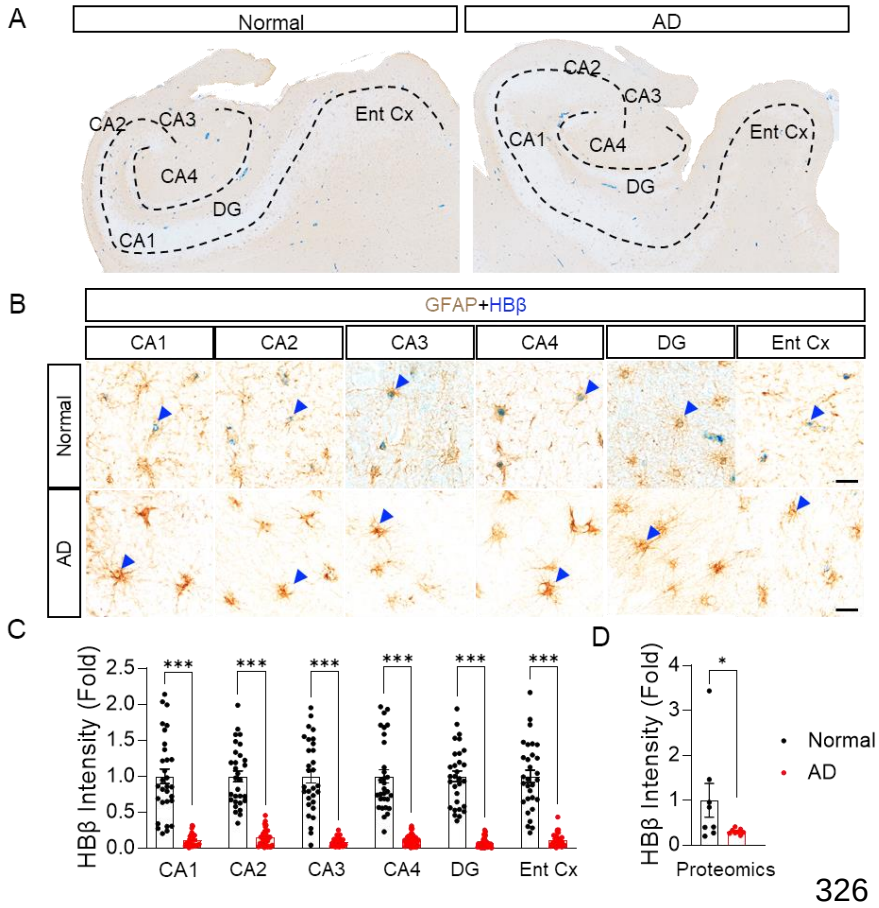

Fig. 6. Astrocytic Hbβ is decreased in the hippocampus of AD patients. (A) Representative images of postmortem hippocampal tissue from normal subjects and AD postmortem brains. **(B)** Representative images of double-staining of GFAP and Hbβ in postmortem hippocampal tissues from normal subjects and AD postmortem brains (20 μM scalebar). **(C)** Quantification of astrocytic Hbβ intensity in each hippocampal sub-region. **(D)** Hbβ proteomic data of the hippocampal postmortem brain. Data are presented as the mean ± s.e.m. *P < 0.05, ***P < 0.001. Additional statistics are provided in table S7.

326

Discussion

In this study, we have discovered that Hb exhibits a peroxidase activity. We have identified the presence of Hb within the hippocampal astrocytes of both mouse and human brains and found a significant decline in astrocytic Hbβ levels in AD, offering a new perspective on its role in neurodegenerative diseases like AD. Furthermore, we synthesized KDS12025, a small molecule characterized by its nanomolar potency, high water solubility, and BBB-permeability, which enhanced the peroxidase activity of Hb by 100-fold, resulting in the effective decomposition of aberrant H_2O_2 even in AD-like cultured astrocytes with reduced Hbβ levels. KDS12025 effectively prevented astrogliosis, restored memory function, and recovered the reduced level of astrocytic Hbβ in AD mouse models. Gene-silencing of Hbβ substantiated that astrocytic Hbβ in the hippocampus is necessary for the H_2O_2-decomposing effect of KDS12025 both *in vitro* and *in vivo*, without affecting the primary respiratory function of Hb. The presence of Hb in human hippocampal astrocytes highlights its potential as a therapeutic target, substantiating KDS12025's clinical relevance for treating AD. These findings propose KDS12025 as a new H_2O_2-decomposing enhancer for Hb and a novel approach for treatment, effectively targeting oxidative stress in neurodegenerative diseases including AD (fig. S13).

Our study provides compelling evidence for Hb's antioxidative function through its H_2O_2-decomposing peroxidase activity within hippocampal astrocytes. We demonstrate that Hb's ability to decompose H_2O_2 is not due to a catalase-like activity, as shown in our oxygen liberation assay (Fig. 2). Instead, Hb exhibits H_2O_2-decomposing peroxidase activity which is validated by both peroxidase-dependent and -independent H_2O_2 assays (Fig. 1 and 2). Our results align well with the previous report proposing Hb's peroxidase role in the plasma (*9, 34*). Previous quantum mechanics studies describe the importance of Arg38 in coordinating proton transfer between the substrate, H_2O_2, and acceptor, His42, in the HRP peroxidase mechanism (*16, 35*) (fig. S14A). Hb does not contain this Arg or any other polar residues in proximity (*36*) (fig. S14B), therefore exhibiting much lower peroxidase activity. In this study, we found that treatment of Hb by KDS12025 increases Hb's peroxidase activity by 100-fold even at extremely low level of Hb (Fig. 2E). We propose that this heightened activity of Hb may be due to the KDS12025's aniline group acting as this missing polar residue to assist and stabilize in coordinating H_2O_2 and H_2O to the iron atom (fig. S14C). It is possible that KDS12025 enhances the thermodynamic and kinetic dynamics of Hb's ability to reduce H_2O_2. Further

research is needed to test this exciting possibility of how KDS12025 interacts with Hb, H_2O_2, and H_2O to decompose one molecule of H_2O_2 into two molecules of H_2O (fig. S14D).

Although extensive research has identified H_2O_2 as a significant contributor to AD pathology (*10, 12, 13, 37*), traditional antioxidants have failed to alleviate AD symptoms due to poor brain compatibility, high dosage requirements, and high reactivity, which all limit their practical use in treating AD (*12, 13*). Hence, KDS12025 would be the first-in-class drug candidate that enhances Hb's H_2O_2-decomposing peroxidase activity without directly scavenging H_2O_2 (Fig. 1), offering a new approach to treat AD. Furthermore, KDS12025 at 10 μM boosts Hb's capacity to decompose H_2O_2 up to 20% even at 100-fold lower concentrations of Hb (0.04 U/ml), at which Hb shows virtually no peroxidase activity in the absence of KDS12025 (Fig. 2E). This unique feature of KDS12025 circumvents the limitations of traditional H_2O_2-scavengers such as sodium pyruvate (800 mg/kg) (*38*) and *N*-acetylcysteine (200 mg/kg) (*39*), which require much higher, often impractical doses. Indeed, we have utilized an extremely low dose of 0.1 mg/kg/day even by oral administration *ad libitum* and found a potent effect of alleviating memory impairment in the GiD mouse model of AD (fig. S10C). Thus, KDS12025 promises an effective treatment option that paves new therapeutic avenues for treating neurodegenerative diseases by boosting Hb's intrinsic antioxidative properties at extremely low doses with minimal side effects.

Our findings also propose that oxidative stress influences astrocytic Hbβ in the hippocampus, leading to decreased Hbβ levels in AD. We have shown that while Hbβ is present in hippocampal astrocytes, its levels are reduced in the hippocampus of mouse models (Fig. 5) and AD patients (Fig. 6). This is consistent with reduced Hbβ mRNA and protein levels in the cortex and hippocampus of AD patients (*40, 41*), paralleled by findings in aged mice models showing a marked decrease in the cortical astrocytic Hbβ mRNA (*42*). Paradoxically, while increases in Hbβ have been reported in the cerebrospinal fluid (CSF) of mild cognitive impairment patients (*43*), our findings align with this in that acute exposure to H_2O_2 in cultured astrocytes leads to an increase in Hbβ mRNA (fig. S11D), suggesting an involvement of initial antioxidant defense by Hbβ. However, it appears that Hbβ eventually leaks into the CSF in neurodegenerative states like AD, leading to a depletion of Hbβ in the brain (*43*). Based on those observations, we hypothesize that if aberrantly excessive H_2O_2 is not resolved in time, it can lead to irreversible severe reactive astrogliosis and chronic oxidative stress that further depletes astrocytic Hbβ, perpetuating a vicious cycle of reactive astrogliosis and excessive

390 H_2O_2-production that further exacerbates and accelerates AD progression. In other words, once
391 the reactive astrocytes become severely reactive and engage in the vicious cycle, the condition
392 may become irreversible, where targeting and removing Aβ plaques might be ineffective,
393 particularly in late-stage AD. These new concepts can provide plausible explanations for the
394 recent setbacks of the immunotherapy-based drug candidates that attempt to remove Aβ
395 plaques. In contrast, treating with KDS12025 in AD animal models liberates the hippocampal
396 astrocytes from the vicious cycle to enter into a virtuous cycle of recovered astrocytic Hbβ
397 level and reduced H_2O_2 that further reduces oxidative stress and accelerates recovery from AD.
398 Taken together, KDS12025 can counteract the decline of antioxidative functions commonly
399 observed in neurodegenerative diseases, offering a viable therapeutic strategy for AD where
400 natural defenses fall short.

401 Extracellular free Hb has been traditionally viewed as toxic due to its tendency to elicit
402 inflammatory responses and damage through ferroptosis (*2, 44*). However, emerging reports
403 suggest that exogenous Hb can mitigate inflammatory responses in cultured astrocytes (*5*). Our
404 study highlights the beneficial role of Hb, i.e., the antioxidative role of endogenous Hbβ in the
405 hippocampal astrocytes (Fig. 5 and 6) under certain conditions, especially when modulated by
406 specific enhancers like KDS12025. This is further supported by the gene-silencing results,
407 revealing that the absence of Hbβ increases vulnerability to H_2O_2 (Fig. 5B). The unexpected
408 antioxidative role of Hbβ proposes brain Hbβ as an effective therapeutic target in
409 neurodegenerative diseases like AD to manage oxidative stress potently and selectively.
410 KDS12025's therapeutic potential can be further expanded to relieve H_2O_2-mediated
411 neurodegeneration and oxidative stress in various neurodegenerative diseases such as
412 Parkinson's disease, amyotrophic lateral sclerosis, ischemic stroke, spinal cord injury and even
413 aging. Furthermore, because Hb is abundantly present in the blood, KDS12025 can
414 conveniently target the blood Hb. In support of this idea, the administration of erythropoietin,
415 a hematopoietic cytokine that can upregulate Hb in red blood cells, has been shown to exert
416 protective effects in the heart, the vasculature, and the nervous system in addition to attenuating
417 AD-like symptoms (*45*). Future investigations should be carried out to examine whether
418 KDS12025 can be effective in diseases related to peripheral or systemic H_2O_2 by targeting the
419 blood Hb. In summary, we have delineated the unprecedented antioxidative function of Hb in
420 the brain, which can be boosted by KDS12025. The newly developed tools and concepts in this

study should be useful in overcoming various brain and peripheral diseases whose etiology involves oxidative stress.

References and Notes

1. D. Bulters *et al.*, Haemoglobin scavenging in intracranial bleeding: biology and clinical implications. *Nat Rev Neurol* **14**, 416-432 (2018).
2. M. A. Altinoz *et al.*, Involvement of hemoglobins in the pathophysiology of Alzheimer's disease. *Exp Gerontol* **126**, 110680 (2019).
3. M. Biagioli *et al.*, Unexpected expression of alpha- and beta-globin in mesencephalic dopaminergic neurons and glial cells. *Proc Natl Acad Sci U S A* **106**, 15454-15459 (2009).
4. O. I. Butt, P. W. Buehler, F. D'Agnillo, Blood-brain barrier disruption and oxidative stress in guinea pig after systemic exposure to modified cell-free hemoglobin. *Am J Pathol* **178**, 1316-1328 (2011).
5. S. B. Sankar, R. K. Donegan, K. J. Shah, A. R. Reddi, L. B. Wood, Heme and hemoglobin suppress amyloid beta-mediated inflammatory activation of mouse astrocytes. *J Biol Chem* **293**, 11358-11373 (2018).
6. F. Amri, I. Ghouili, M. C. Tonon, M. Amri, O. Masmoudi-Kouki, Hemoglobin-Improved Protection in Cultured Cerebral Cortical Astroglial Cells: Inhibition of Oxidative Stress and Caspase Activation. *Front Endocrinol (Lausanne)* **8**, 67 (2017).
7. M. Kvist, E. S. Ryabova, E. Nordlander, L. Bulow, An investigation of the peroxidase activity of Vitreoscilla hemoglobin. *J Biol Inorg Chem* **12**, 324-334 (2007).
8. C. E. Cooper, R. Silaghi-Dumitrescu, M. Rukengwa, A. I. Alayash, P. W. Buehler, Peroxidase activity of hemoglobin towards ascorbate and urate: a synergistic protective strategy against toxicity of Hemoglobin-Based Oxygen Carriers (HBOC). *Biochim Biophys Acta* **1784**, 1415-1420 (2008).
9. H. Keum, J. Kim, Y. H. Joo, G. Kang, N. Chung, Hemoglobin peroxidase reaction of hemoglobin efficiently catalyzes oxidation of benzo[a]pyrene. *Chemosphere* **268**, 128795 (2021).
10. H. Chun *et al.*, Severe reactive astrocytes precipitate pathological hallmarks of Alzheimer's disease via H(2)O(2)(-) production. *Nat Neurosci* **23**, 1555-1566 (2020).
11. H. Chun, C. J. Lee, Reactive astrocytes in Alzheimer's disease: A double-edged sword. *Neurosci Res* **126**, 44-52 (2018).
12. D. A. Butterfield, B. Halliwell, Oxidative stress, dysfunctional glucose metabolism and Alzheimer disease. *Nat Rev Neurosci* **20**, 148-160 (2019).
13. H. J. Forman, H. Zhang, Targeting oxidative stress in disease: promise and limitations of antioxidant therapy. *Nat Rev Drug Discov* **20**, 689-709 (2021).
14. J. H. Shin *et al.*, Concurrent blockade of free radical and microsomal prostaglandin E synthase-1-mediated PGE2 production improves safety and efficacy in a mouse model of amyotrophic lateral sclerosis. *J Neurochem* **122**, 952-961 (2012).
15. M. Gajhede, D. J. Schuller, A. Henriksen, A. T. Smith, T. L. Poulos, Crystal structure of horseradish peroxidase C at 2.15 A resolution. *Nat Struct Biol* **4**, 1032-1038 (1997).
16. P. Vidossich *et al.*, On the role of water in peroxidase catalysis: a theoretical investigation of HRP compound I formation. *J Phys Chem B* **114**, 5161-5169 (2010).
17. H. Sies, Oxidative stress: oxidants and antioxidants. *Exp Physiol* **82**, 291-295 (1997).
18. A. Casado, M. Encarnacion Lopez-Fernandez, M. Concepcion Casado, R. de La Torre, Lipid peroxidation and antioxidant enzyme activities in vascular and Alzheimer dementias. *Neurochem Res* **33**, 450-458 (2008).
19. O. Ighodaro, O. Akinloye, First line defence antioxidants-superoxide dismutase (SOD), catalase (CAT) and glutathione peroxidase (GPX): Their fundamental role in the entire antioxidant defence grid. *Alexandria journal of medicine* **54**, 287-293 (2018).

20. B. Entsch, B. A. Palfey, D. P. Ballou, V. Massey, Catalytic function of tyrosine residues in para-hydroxybenzoate hydroxylase as determined by the study of site-directed mutants. *J Biol Chem* **266**, 17341-17349 (1991).
21. M. M. Goyal, A. Basak, Human catalase: looking for complete identity. *Protein Cell* **1**, 888-897 (2010).
22. X. Wang *et al.*, Pyruvate protects mitochondria from oxidative stress in human neuroblastoma SK-N-SH cells. *Brain Res* **1132**, 1-9 (2007).
23. B. Faller, Artificial membrane assays to assess permeability. *Curr Drug Metab* **9**, 886-892 (2008).
24. J. D. Lee *et al.*, Structure-guided engineering of a fast genetically encoded sensor for real-time H₂O₂ monitoring. *bioRxiv*, 2024.2001.2031.578117 (2024).
25. Y. H. Ju *et al.*, Astrocytic urea cycle detoxifies Abeta-derived ammonia while impairing memory in Alzheimer's disease. *Cell Metab* **34**, 1104-1120 e1108 (2022).
26. E. J. Yang, H. Kim, H. S. Kim, M. J. Chang, Phloroglucinol attenuates oligomeric amyloid beta peptide(1)(-)(42)-induced astrocytic activation by reducing oxidative stress. *J Pharmacol Sci* **145**, 308-312 (2021).
27. W. Won *et al.*, Inhibiting peripheral and central MAO-B ameliorates joint inflammation and cognitive impairment in rheumatoid arthritis. *Exp Mol Med* **54**, 1188-1200 (2022).
28. H. Chun, I. Marriott, C. J. Lee, H. Cho, Elucidating the Interactive Roles of Glia in Alzheimer's Disease Using Established and Newly Developed Experimental Models. *Front Neurol* **9**, 797 (2018).
29. K. Lok *et al.*, Characterization of the APP/PS1 mouse model of Alzheimer's disease in senescence accelerated background. *Neurosci Lett* **557 Pt B**, 84-89 (2013).
30. E. F. Willis, P. F. Bartlett, J. Vukovic, Protocol for Short- and Longer-term Spatial Learning and Memory in Mice. *Front Behav Neurosci* **11**, 197 (2017).
31. S. Jo *et al.*, GABA from reactive astrocytes impairs memory in mouse models of Alzheimer's disease. *Nat Med* **20**, 886-896 (2014).
32. S. Lee *et al.*, Channel-mediated tonic GABA release from glia. *Science* **330**, 790-796 (2010).
33. J. Haettig, Y. Sun, M. A. Wood, X. Xu, Cell-type specific inactivation of hippocampal CA1 disrupts location-dependent object recognition in the mouse. *Learn Mem* **20**, 139-146 (2013).
34. D. V. Grigorieva *et al.*, Measurement of plasma hemoglobin peroxidase activity. *Bull Exp Biol Med* **155**, 118-121 (2013).
35. E. Derat, S. Shaik, C. Rovira, P. Vidossich, M. Alfonso-Prieto, The effect of a water molecule on the mechanism of formation of compound 0 in horseradish peroxidase. *J Am Chem Soc* **129**, 6346-6347 (2007).
36. Vlasova, II, Peroxidase Activity of Human Hemoproteins: Keeping the Fire under Control. *Molecules* **23**, (2018).
37. M. A. Ansari, S. W. Scheff, Oxidative stress in the progression of Alzheimer disease in the frontal cortex. *J Neuropathol Exp Neurol* **69**, 155-167 (2010).
38. H. Koivisto *et al.*, Chronic Pyruvate Supplementation Increases Exploratory Activity and Brain Energy Reserves in Young and Middle-Aged Mice. *Front Aging Neurosci* **8**, 41 (2016).
39. J. More *et al.*, N-Acetylcysteine Prevents the Spatial Memory Deficits and the Redox-Dependent RyR2 Decrease Displayed by an Alzheimer's Disease Rat Model. *Front Aging Neurosci* **10**, 399 (2018).

40. S. Vanni *et al.*, Hemoglobin mRNA Changes in the Frontal Cortex of Patients with Neurodegenerative Diseases. *Front Neurosci* **12**, 8 (2018).
41. S. J. Schonberger, P. F. Edgar, R. Kydd, R. L. Faull, G. J. Cooper, Proteomic analysis of the brain in Alzheimer's disease: molecular phenotype of a complex disease process. *Proteomics* **1**, 1519-1528 (2001).
42. M. Orre *et al.*, Acute isolation and transcriptome characterization of cortical astrocytes and microglia from young and aged mice. *Neurobiol Aging* **35**, 1-14 (2014).
43. D. S. Spellman *et al.*, Development and evaluation of a multiplexed mass spectrometry based assay for measuring candidate peptide biomarkers in Alzheimer's Disease Neuroimaging Initiative (ADNI) CSF. *Proteomics Clin Appl* **9**, 715-731 (2015).
44. M. Zille *et al.*, Neuronal Death After Hemorrhagic Stroke In Vitro and In Vivo Shares Features of Ferroptosis and Necroptosis. *Stroke* **48**, 1033-1043 (2017).
45. Y. P. Li *et al.*, Erythropoietin attenuates Alzheimer-like memory impairments and pathological changes induced by amyloid beta42 in mice. *Brain Res* **1618**, 159-167 (2015).
46. Dassault Systèmes BIOVIA, Discovery Studio Modeling Environment, Release 2021, San Diego: Dassault Systèmes, 2023.
47. A. Henriksen, A. T. Smith, M. Gajhede, The Structures of the Horseradish Peroxidase C-Ferulic Acid Complex and the Ternary Complex with Cyanide Suggest How Peroxidases Oxidize Small Phenolic Substrates*. *Journal of Biological Chemistry* **274**, 35005-35011 (1999).
48. S.-Y. Park, T. Yokoyama, N. Shibayama, Y. Shiro, J. R. H. Tame, 1.25 Å Resolution Crystal Structures of Human Haemoglobin in the Oxy, Deoxy and Carbonmonoxy Forms. *Journal of Molecular Biology* **360**, 690-701 (2006).
49. G. I. Berglund *et al.*, The catalytic pathway of horseradish peroxidase at high resolution. *Nature* **417**, 463-468 (2002).
50. Kamaljeet, S. Bansal, U. SenGupta, A Study of the Interaction of Bovine Hemoglobin with Synthetic Dyes Using Spectroscopic Techniques and Molecular Docking. *Frontiers in Chemistry* **4**, (2017).
51. K. V. Pathak, T.-L. Chiu, E. A. Amin, R. J. Turesky, Methemoglobin Formation and Characterization of Hemoglobin Adducts of Carcinogenic Aromatic Amines and Heterocyclic Aromatic Amines. *Chemical Research in Toxicology* **29**, 255-269 (2016).
52. C. Puscas *et al.*, The high affinity of small-molecule antioxidants for hemoglobin. *Free Radical Biology and Medicine* **124**, 260-274 (2018).
53. B. J. Reeder *et al.*, Tyrosine Residues as Redox Cofactors in Human Hemoglobin: IMPLICATIONS FOR ENGINEERING NONTOXIC BLOOD SUBSTITUTES*. *Journal of Biological Chemistry* **283**, 30780-30787 (2008).
54. M. Sharma, N. Farhat, A. U. Khan, F. H. Khan, R. Mahmood, Studies on the interaction of 2,4-dibromophenol with human hemoglobin using multi-spectroscopic, molecular docking and molecular dynamics techniques. *Journal of Biomolecular Structure and Dynamics*, 1-11 (2023).
55. C. J. Lee *et al.*, Astrocytic control of synaptic NMDA receptors. *J Physiol* **581**, 1057-1081 (2007).
56. W. B. Stine, Jr., K. N. Dahlgren, G. A. Krafft, M. J. LaDu, In vitro characterization of conditions for amyloid-beta peptide oligomerization and fibrillogenesis. *J Biol Chem* **278**, 11612-11622 (2003).
57. J. H. Park *et al.*, Newly developed reversible MAO-B inhibitor circumvents the shortcomings of irreversible inhibitors in Alzheimer's disease. *Sci Adv* **5**, eaav0316 (2019).

58. H. Chun *et al.*, Severe reactive astrocytes precipitate pathological hallmarks of Alzheimer's disease via H2O2(-) production. *Nat Neurosci* **23**, 1555-1566 (2020).
59. A. Ventura *et al.*, Cre-lox-regulated conditional RNA interference from transgenes. *Proc Natl Acad Sci U S A* **101**, 10380-10385 (2004).

Acknowledgments: We express our sincere thanks to Yejin Cho, Juyeon Chae, Suyeon Yellena Kim, and Eunjin Shin for providing technical assistance in producing AAV viruses, optimizing enzyme assays, and capturing Lattice SIM images. We also extend our gratitude to the Research Solution Center (RSC) at the Institute for Basic Science (IBS) for their management of the animal facilities and for providing access to Imaris software. Special thanks to Dr. Andre Berndt from the University of Washington for generously supplying the oROS-G plasmid. Additionally, we acknowledge BioRender.com for facilitating the creation of some of the illustrative images presented in our work.

Funding: This work was supported by the following agencies: the Institute for Basic Science (IBS), Center for Cognition and Sociality (IBS-R001-D2 to C.J.L.); the Korea Health Technology R&D Project through the Korea Health Industry Development Institute (KHIDI) and Korea Dementia Research Center (KDRC), funded by the Ministry of Health & welfare and Ministry of Science and ICT, Republic of Korea (HU23C0018 to K.D.P.), and the Korea Institute of Science and Technology (KIST) Institutional Program (2E32851 to K.D.P.); the National Research Foundation (NRF) grant funded by the Korea government (MSIT) (RS-2023-00261784 to A.N.P). Supercomputing resources were provided by the Korea Institute of Science and Technology Information (KISTI-HPC) (KSC-2023-CRE-0420 to A.N.P.).

Author contributions:

Conceptualization: WW, EHL, HC, CJL, KDP

Methodology: WW, EHL, LG, CJL, KDP, ANP

Investigation: WW, EHL, LG, HC, DK, MB, JC, TK, UP, JL, SO, CJW, YK, SJP

Funding acquisition: CJL, KDP, ANP

Supervision: CJL, KDP, ANP, HR

Writing: WW, EHL, LG, CJL, KDP, ANP

Competing interests: The authors declare a competing interest due to a patent associated with KDS12025.

Data and materials availability: All data are available in the main text or the supplementary materials.

Supplementary Materials

Materials and Methods

figs. S1 to S14

tables S1 to S7

References

Material and Methods

In vitro H_2O_2 assay

Hb (Sigma-Aldrich, H7379), H_2O_2 (Sigma-Aldrich, H1009-5ml), and Amplex Red reagent (Invitrogen™ A12222) were obtained for the study. We prepared 4 μM H_2O_2 solution from a serial dilution in a 50 mM sodium phosphate buffer (pH 7.2). Subsequently, 49 μl of the 4 μM H_2O_2 solution was mixed with 1 μl of the test compound in DMSO. The resulting mixture, combined with an assay solution comprising Amplex Red reagent (diluted from a 20 mM stock solution to 0.1 mM) and HRP (diluted from a 200U/ml stock solution to 0.2 U/ml), was added to the wells at 50 μl per well. After a 60-minute incubation at 37°C, the production of resorufin from Amplex Red was quantified using a microplate fluorescence reader (SpectraMax i5 reader, Molecular Devices) at ex/em=535/580 nm. For Hb experiments, the protocol remained consistent, substituting HRP with Hb (diluted from an 8 mg/mL stock to 10 μg/ml). Following co-treatment, the plate was incubated at 37 °C for 30 min and the mean intensity of fluorescence was measured using iD5 microplate readers.

In the ROS-Glo assay, the H_2O_2 substrate solution and ROS-Glo detection solution were prepared according to the manufacturer's instructions. The concentration of H_2O_2 and drugs was the same as in the Amplex Red assay, but the presence of the HRP, Hb, CAT, or GPx depended on the experiments. Then, the relative luminescent values were measured using iD5 microplate readers. To evaluate the extent of peroxidase function facilitation by HTPEB (1 μM) and KDS12025 (1 μM) in HRP (0.2 U/ml) and Hb (10 μg/ml), we measured the difference over 30 and 60 minutes using the ROS-Glo assay. The fold change was calculated by dividing the delta values during the 30-minute reaction for the vehicle over drug conditions.

To assess enzyme activity, the amount of H_2O_2 consumed over a specific time was quantified alongside a standard curve. To determine Hb's peroxidase function, we administered Hb in a dose-dependent manner, ranging from 0.01 to 112 U/ml, and pre-incubated it with H_2O_2 along with DMSO (vehicle), HTPEB (1 μM), or KDS12025 (1 μM) at 37°C for 30 minutes. Subsequently, the remaining H_2O_2 was measured using the ROS-Glo assay. We normalized the values against conditions without Hb and plotted the dose-response. Using the Prism program for curve fitting, we calculated the EC_{50} and EC_{20} values of the H_2O_2-decomposition. All the EC_{50} and EC_{20} values were determined by fitting data with GraphPad Prism 10.2.1.

General Synthetic Method

Reaction progression was checked using analytical thin-layer chromatography (TLC) plates (#1.05715, Merck) and analyzed with 254 nm and 365 nm ultraviolet light. The reaction mixtures were purified by flash column chromatography using silica gel (#1.09385, Merck). Melting points were determined in open capillary tubes using a Standford Research Systems melting point apparatus and were uncorrected. Nuclear magnetic resonance (NMR) spectral data were obtained at 400MHz (^{1}H) and at 100MHz (^{13}C) using a BRUKER apparatus. Chemical shits (δ) were expressed in parts per million (ppm) from tetramethylsilane (TMS), the internal standard and coupling constants (J) were expressed in hertz and assigned as follows: s, singlet; d, doublet; t, triplet; q, quartet; AB_q, AB quartet; br, broad; m, multiplet. All chemical reagents and solvents were of reagent grade, used without further purification and were purchased from commercial sources. Analytical HPLC was performed using a Waters E2695 system equipped with a SHISEIDO capcell pak C_{18} MGII column (4.6mm x 150 mm; 5 μm). HPLC data were recorded using the following parameters: 0.1% acetic acid in H2O/ MeCN, 90/10 -> 0/100 in 10 minutes, +10 minute isocratic hold, flow rate of 1.0 mL/min, λ=254 and

280 nm. Compounds were checked by using TLC, ^{1}H and ^{13}C NMR and LR-MS. The TLC, NMR, and analytic data confirmed that the purity of the products was $\geq$ 95%.

Preparation of *N*-methyl-4-nitroaniline (1)

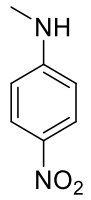

A solution of fluoro-4-nitrobenzene (1.0 g, 7.1 mmol) and methylamine (3.41 g, 109.9 mmol) in 10 mL ethanol was heated at reflux for 24 hours. The reaction was cooled and concentrated in vacuo. The resulting residue was diluted with ethyl acetate and washed with brine, dried (Na_2SO_4), and the solvent removed in vacuo to give 913.3 mg (85%) of the title compound as a yellow solid. R_f = 0.70 (*n*-Hex 1: EtOAc 1); ^{1}H NMR (400 MHz, DMSO-d_6) δ 8.01 (d, 2H, J = 9.28), 7.31 (d, 1H, J = 4.28), 6.61 (d, 2H, J = 9.36), 2.80 (d, 2H, J = 5.00), 2.33 (s, 1H).

Preparation of *tert*-butyl methyl(4-nitrophenyl)carbamate (2)

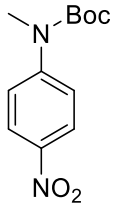

To a solution of *N*-methyl-4-nitroaniline (800 mg, 5.26 mmol) in 10 mL THF were added di-*tert*-butyl dicarbonate (1.72 g, 7.89 mmol) and 4-dimethylaminopyridine (32.1 mg, 0.26 mmol). The reaction mixture was heated at reflux for 12 hours. The reaction was cooled and concentrated in vacuo. The resulting residue was diluted with ethyl acetate and washed with brine, dried (Na_2SO_4), and the solvent was removed in vacuo to give 1.29 g (97%) of the title compound as a yellow oil. R_f = 0.80 (*n*-Hex 3: EtOAc 1); ^{1}H NMR (400 MHz, DMSO-d_6) δ 8.20 (d, 2H, J = 9.20), 7.60 (d, 2H, J = 9.16), 3.29 (s, 3H), 1.45 (s, 9H)

Preparation of *tert*-butyl (4-aminophenyl)(methyl)carbamate (3)

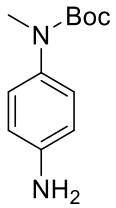

To a solution of *tert*-butyl methyl(4-nitrophenyl)carbamate (6.67g, 26.45 mmol) in 25mL methanol, was added palladium on carbon (667 mg). The reaction mixture was stirred under hydrogen for 2 hours at room temperature. The reaction was filtered through a pad of celite. The filtrate was concentrated in vacuo, to give 5.1768 g (88%) of the title compound as a yellow solid. R_f = 0.05 (*n*-Hex 1: EtOAc 1); ^{1}H NMR (400 MHz, DMSO-d_6) δ 6.86 (d, 2H, J = 8.52), 6.50 (d, 2H, J = 8.60), 5.01 (s, 2H), 3.06 (s, 3H), 1.35 (s, 9H)

Preparation of 1-(2-bromoethyl)-2-methoxybenzene (5a)

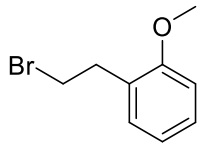

To a solution of 2-(2-methoxyphenyl)ethan-1-ol (5g, 32.85 mmol) in anhydrous dichloromethane (75 mL) was added carbon tetrabromide (15.25 g, 45.99 mmol) and stirred at 0° under nitrogen atmosphere. Triphenylphospine (10.35 g, 39.42 mmol) was added potionwise and stirred under same condition for 1 hour. The reaction mixture was concentrated in vacuo and the residue was purified by column chromatography on silica gel, eluting with *n*-hexane only and then a mixture of *n*-hexane and ethyl acetate (20:1) to afford 5.8069 g (82%) of title compound as a colorless oil. R_f = 0.20 (*n*-Hex); ^{1}H NMR (400 MHz, DMSO-d_6) δ 7.24 (t, 1H, J = 7.98), 6.99 (d, 1H, J = 8.16), 6.89 (t, 1H, J = 7.36), 3.79 (s, 3H), 3.64 (t, 2H, J = 7.48), 3.09 (t, 2H, J = 7.44)

Preparation of 1-(2-bromoethyl)-3-methoxybenzene (5b)

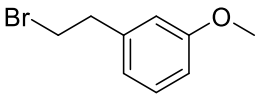

To a solution of 2-(3-methoxyphenyl)ethan-1-ol (1g, 6.57 mmol) in anhydrous dichloromethane (20 mL) was added carbon tetrabromide (3.05 g, 9.20 mmol) and stirred at 0° under nitrogen atmosphere. Triphenylphospine (2.06 g, 7.88 mmol) was added potionwise and stirred under same condition for 1 hour. The reaction mixture was concentrated in vacuo and the residue was purified by column chromatography on silica gel, eluting with *n*-hexane only and then a mixture of *n*-hexane and ethyl acetate (20:1) to afford 1.37 g (97%) of title compound as a colorless oil. R_f = 0.20 (*n*-Hex); ^{1}H NMR (400 MHz, DMSO-d_6) δ 7.23 (t, 1H, J = 7.60), 6.88 (m, 3H), 3.75 (s, 3H), 3.74 (t, 2H, J = 7.2), 3.11 (t, 2H, J = 7.2)

General procedure for alkylated compounds (7a-7k) (Method A)

To a solution of aniline (3, 4a-4d) (1.0-3.0 equiv) in acetonitrile, were added potassium carbonate/cesium carbonate (1.0-1.2 equiv), potassium iodide (0.1 equiv), and phenethyl bromide (6a-6g) (1.0 equiv) in a sealed tube. The reaction mixture was heated at 110°C for 36 hours. The reaction mixture was cooled and diluted with ethyl acetate and washed with brine, dried with anhydrous Na_2SO_4, and concentrated in vacuo. Purification by column chromatography afforded the desired compound compound.

General procedure for final KDS compounds (8a-8h) (Method B)

To a solution of amine containing compounds (7e-7k) (1.0 equiv) was dissolved in anhydrous dichloromethane was added 4.0M hydrochloric acid in dioxane (4.0-6.0 equiv). The reaction mixture was stirred at room temperature for 48 hours. The precipitate was filtered and the filtercake was obtained to afford the desired compound

***tert*-butyl methyl(4-((4-(trifluoromethyl)phenethyl)amino)phenyl)carbamate (7a)**

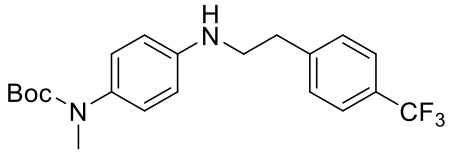

Using method A, *tert*-butyl (4-aminophenyl)(methyl)carbamate (440 mg, 1.98 mmol), 1-(2-bromoethyl)-4-(trifluoromethyl)benzene (500 mg, 1.98 mmol), potassium carbonate (821 mg, 5.94 mmol), and potassium iodide (33 mg, 0.20 mmol) in acetonitrile (10 mL) to give 7a as an off white solid (319 mg, 41%); R_f = 0.45 (*n*-Hex 3: EtOAC 1); ^{1}H NMR (400 MHz, DMSO-d_6) δ 7.68 (d, 2H, J = 8.00 Hz) 7.53 (d, 2H, J = 8.00 Hz), 6.96 (d, 2H, J = 8.80 Hz), 6.57 (d, 2H, J = 8.80 Hz), 5.70 (t, 1H, J = 5.60 Hz), 3.28 (t, 2H, J = 7.20 Hz), 3.08 (s, 3H), 2.94 (d, 2H, J = 7.20 Hz)

N-(4-(trifluoromethyl)phenethyl)aniline (7b)

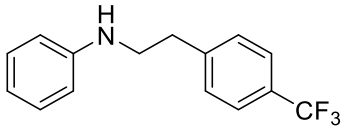

Using method A, aniline (552mg, 5.93 mmol), 1-(2-bromoethyl)-4-(trifluoromethyl)benzene (500mg, 1.98 mmol), potassium carbonate (273 mg, 1.98 mmol), and potassium iodide (33 mg, 0.20 mmol) in acetonitrile (10 mL) gave 7b as a white solid (50.4 mg, 8%); R_f = 0.50 (*n*-Hex 9: EtOAC 1); HPLC purity: 7.7 min, 99.2%; mp 20-30 °C; ^{1}H NMR (400 MHz, DMSO-d_6) δ 7.65 (d, 2H, J = 8.12 Hz), 7.50 (d, 2H, J = 8.04 Hz), 7.07 (t, 2H, J = 8.16 Hz), 6.59 (d, 2H, J = 8.12 Hz), 6.53 (t, 1H, J = 7.24 Hz), 5.65 (t, 1H, J = 5.56 Hz), 3.30-3.25 (m, 2H), 2.92 (t, 2H, J = 7.28 Hz); ^{13}C NMR (100 MHz, DMSO-d_6) δ 149.1, 145.5, 130.0, 129.4, 127.7, 127.4, 127.1, 126.8, 126.3, 125.5 (q, $J_{C\text{-}F}$ = 3.57 Hz), 116.2, 112.5, 44.5 (**C**H$_2$), 35.1 (**C**H$_2$)

4-((4-(trifluoromethyl)phenethyl)amino)phenol (7c)

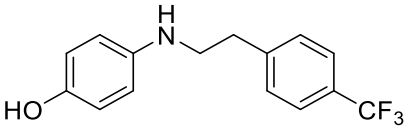

Using method A, 4-aminophenol (258.6 mg, 2.37 mmol), 1-(2-bromoethyl)-4-(trifluoromethyl)benzene (200 mg, 0.79 mmol), potassium carbonate (200 mg, 0.79 mmol), and potassium iodide (13 mg, 0.08 mmol) in acetonitrile (4 mL) gave 7c as a white solid (111 mg, 53%); R_f = 0.30 (*n*-Hex 3: EtOAC 1); HPLC purity: 9.3 min, >99.9%; mp 110-120 °C; ^{1}H NMR (400 MHz, DMSO-d_6) δ 8.39 (s, 1H), 7.64 (d, 2H, J = 8.00 Hz), 7.49 (d, 2H, J = 8.00 Hz), 6.55 (d, 2H, J = 8.56 Hz), 6.45 (d, 2H, J = 8.64 Hz), 4.99 (s, 1H), 3.21-3.17 (m, 2H), 2.89 (t, 2H, J = 7.20 Hz) ^{13}C NMR (100 MHz, DMSO-d_6) δ 148.8, 145.7, 134.6, 130.0, 125.5 (q, $J_{C\text{-}F}$ = 4.06), 116.2, 113.9, 103.1 45.7 (**C**H$_2$), 35.3 (**C**H$_2$)

3-((4-(trifluoromethyl)phenethyl)amino)benzoic acid (7d)

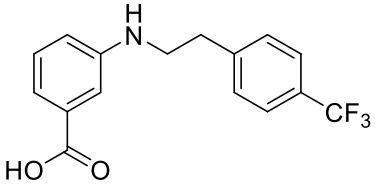

Using method A, 3-aminobenzoic acid (813 mg, 5.93 mmol), 1-(2-bromoethyl)-4-(trifluoromethyl)benzene (500 mg, 1.98 mmol), potassium carbonate (273 mg, 1.98 mmol), and potassium iodide (33 mg, 0.20 mmol) in acetonitrile (10 mL) gave 7d as a white solid (49 mg, 8%); R_f = 0.30 (*n*-Hex 3: EtOAC 1); HPLC purity: 12.6 min, 98.4%; mp 82-86 °C; ^{1}H NMR (400 MHz, DMSO-d_6) δ 12.65, (s, 1H), 7.66 (d, 2H, J = 8.08 Hz), 7.51 (d, 2H, J = 7.92 Hz), 7.21-7.18 (m, 2H), 7.14 (d, 1H, J = 7.40 Hz), 6.83 (d, 1H, J = 7.08 Hz), 5.98 (s, 1H), 3.32 (t, 2H, J = 7.04 Hz), 2.94 (t, 2H, J = 6.88 Hz) ^{13}C NMR (100 MHz, DMSO-d_6) δ 166.6 (**C**(O)), 149.5, 143.8, 130.7, 130.2, 129.5, 127.6 (q, $J_{C\text{-}F}$ = 31.56 Hz), 125.7 (q, $J_{C\text{-}F}$ = 3.71 Hz), 124.9 (q, $J_{C\text{-}F}$ = 270.27 Hz), 118.9, 116.7, 114.5, 64.9(**C**H_2), 34.6(**C**H_2)

N^1,N^1-dimethyl-N^4-(4-(trifluoromethyl)phenethyl)benzene-1,4-diamine (7e)

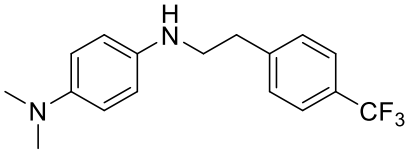

Using method A, N^1,N^1-dimethylbenzene-1,4-diamine (646 mg, 4.74 mmol), 1-(2-bromoethyl)-4-(trifluoromethyl)benzene (1.0g, 3.96 mmol), potassium carbonate (1.64 g, 11.88 mmol), and potassium iodide (66 mg, 0.40 mmol) in acetonitrile (20 mL) gave 7e as a dark brown oil (300 mg, 25%); R_f = 0.37 (*n*-Hex 3: EtOAC 1) ^{1}H NMR (400 MHz, DMSO-d_6) δ 7.66 (d, 2H, J = 8.00 Hz), 7.50 (d, 2H, J = 8.00 Hz), 6.65 (d, 2H, J = 8.96 Hz), 6.54 (d, 2H, J = 8.96 Hz), 5.02 (t, 1H, J = 6.00 Hz), 3.22 (q, 2H, J = 6.44 Hz), 2.91 (t, 2H, J = 7.12 Hz), 2.72 (s, 6H)

***tert*-butyl (4-((2-methoxyphenethyl)amino)phenyl)(methyl)carbamate (7f)**

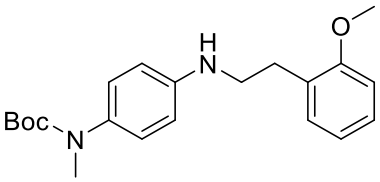

Using method A, I-butyl (4-aminophenyl)(methyl)carbamate (2.10 g, 9.45 mmol), 1-(2-bromoethyl)-2-methoxybenzene (2.03 g, 9.45 mmol), cesium carbonate (3.69 g, 11.34 mmol), and potassium iodide (157.7 mg, 0.95 mmol) in acetonitrile (20 mL) gave 7f as a yellow oil (1.21 g, 36%); R_f = 0.42 (*n*-Hex 3: EtOAC 1); ^{1}H NMR (400 MHz, DMSO-d_6) δ 7.23-7.18 (m, 2H), 6.97 (d, 1H, J = 7.92 Hz), 6.93 (d, 2H, J = 8.64 Hz), 6.88 (t, 1H, J = 7.36 Hz), 6.54 (d, 2H, J = 8.76 Hz), 5.69 (t, 1H, J = 5.68 Hz), 3.81 (s, 3H), 3.18-3.13 (m, 2H), 3.07 (s, 3H), 2.80 (t, 2H, J = 6.84 Hz), 1.35 (s, 9H)

***tert*-butyl (4-((3-methoxyphenethyl)amino)phenyl)(methyl)carbamate (7g)**

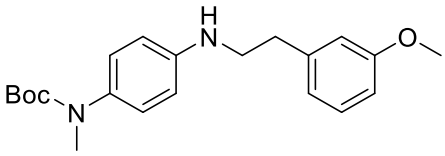

Using method A, *tert*-butyl (4-aminophenyl)(methyl)carbamate (455 mg, 2.05 mmol), 1-(2-bromoethyl)-3-methoxybenzene (400 mg, 1.86 mmol), potassium carbonate (771 mg, 5.58 mmol), and potassium iodide (32 mg, 0.19 mmol) in acetonitrile (5 mL) gave 7g as a yellow oil (244 mg, 37%); R_f = 0.41 (*n*-Hex 3: EtOAC 1); ^{1}H NMR (400 MHz, DMSO-d_6) δ 7.22 (t,

1H, J = 8.04 Hz), 6.95 (d, 2H, J = 8.60 Hz), 6.86-6.85 (m, 2H), 6.80-6.77 (m, 1H), 6.55 (d, 2H, J = 8.72 Hz), 5.65 (t, 1H, J = 5.64 Hz), 3.72 (s, 3H), 3.23 (q, 2H, J = 6.80 Hz), 3.08 (s, 3H), 2.81 (t, 2H, J = 7.60 Hz), 1.36 (s, 9H)

***tert*-butyl (4-((4-methoxyphenethyl)amino)phenyl)(methyl)carbamate (7h)**

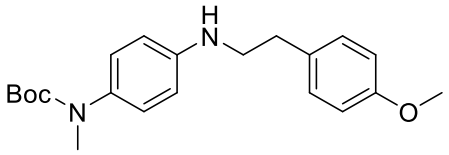

Using method A, *tert*-butyl (4-aminophenyl)(methyl)carbamate (340 mg, 1.53 mmol), 1-(2-bromoethyl)-4-methoxybenzene (300 mg, 1.39 mmol), potassium carbonate (578 mg, 4.18 mmol), and potassium iodide (23 mg, 0.14 mmol) in acetonitrile (5 mL) gave 7h as a yellow oil (244 mg, 37%); R_f = 0.41 (*n*-Hex 3: EtOAC 1); ^{1}H NMR (400 MHz, DMSO-d_6) δ 7.20 (d, 2H, J = 8.52 Hz), 6.94 (d, 2H, J = 8.60 Hz), 6.87 (d, 2H, J = 8.52 Hz), 6.54 (d, 2H, J = 8.72 Hz), 5.63 (t, 1H, J = 5.60 Hz), 3.73 (s, 3H), 3.21-3.16 (m, 2H), 3.08 (s, 3H), 2.77 (t, 2H, J = 7.24), 1.36 (s, 9H)

***tert*-butyl methyl(4-(phenethylamino)phenyl)carbamate (7i)**

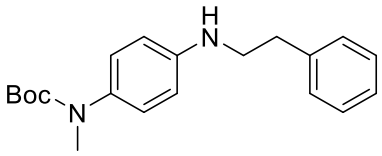

Using method A, *tert*-butyl (4-aminophenyl)(methyl)carbamate (500 mg, 2.25 mmol), (2-bromoethyl)benzene (416 mg, 2.25 mmol), cesium carbonate (879.4 mg, 2.70 mmol), and potassium iodide (37 mg, 0.23 mmol) in acetonitrile (10 mL) gave 7i as a yellow oil (160.4 mg, 20%); R_f = 0.32 (*n*-Hex 9: EtOAC 1); ^{1}H NMR (400 MHz, DMSO-d_6) δ 7.32-7.27 (m, 4H), 7.22-7.18 (m, 1H), 6.93 (d, 2H, J = 8.68 Hz), 6.54 (d, 2H, J = 8.80), 5.65 (t, 1H, J = 5.72 Hz), 3.25-3.19 (m, 2H), 3.07 (s, 3H), 2.83 (t, 2H, J = 7.76), 1.35 (s, 9H)

***tert*-butyl methyl(4-((3-(trifluoromethyl)phenethyl)amino)phenyl)carbamate (7j)**

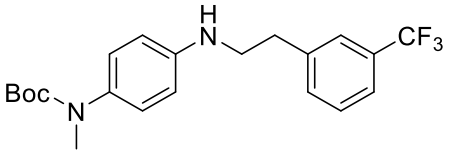

Using method A, *tert*-butyl (4-aminophenyl)(methyl)carbamate (440 mg, 1.98 mmol), 1-(2-bromoethyl)-3-(trifluoromethyl)benzene (500 mg, 1.98 mmol), potassium carbonate (821 mg, 5.94 mmol), and potassium iodide (33 mg, 0.20 mmol) in acetonitrile (7 mL) to give 7j as an off white solid (395 mg, 51%); R_f = 0.44 (*n*-Hex 3: EtOAc 1); ^{1}H NMR (400 MHz, DMSO-d_6) δ 7.64 (s, 1H), 7.61-7.52 (m, 3H), 6.95 (d, 2H, J = 8.72 Hz), 6.56 (d, 2H, J = 8.80 Hz), 5.69 (t, 1H, 5.68 Hz), 3.30-3.25 (m, 2H), 3.08 (s, 3H), 2.94 (t, 2H, J = 7.16 Hz)

***tert*-butyl methyl(4-((2-(trifluoromethyl)phenethyl)amino)phenyl)carbamate (7k)**

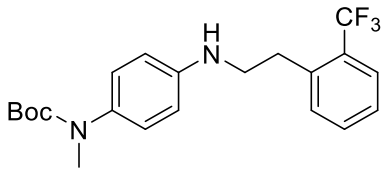

Using method A, *tert*-butyl (4-aminophenyl)(methyl)carbamate (295 mg, 1.33 mmol), 1-(2-bromoethyl)-2-(trifluoromethyl)benzene (337 mg, 1.33 mmol), potassium carbonate (552 mg, 3.99 mmol), and potassium iodide (22 mg, 0.13 mmol) in acetonitrile (7 mL) to give 7j as an off white solid (319 mg, 41%); Rf = 0.45 (*n*-Hex 3: EtOAc 1); ^{1}H NMR (400 MHz, DMSO-d_6) δ 7.73 (d, 1H, J = 7.72 Hz), 7.65 (t, 1H, J = 7.36 Hz), 7.58 (d, 1H, J = 7.60 Hz), 7.46 (t, 1H, J = 7.48 Hz), 6.97 (d, 2H, J = 8.64 Hz), 6.58 (d, 2H, J = 8.76 Hz), 5.85 (t, 1H, J = 5.84 Hz), 3.29-3.24 (m, 2H), 3.09 (s, 3H), 3.01 (t, 2H, J = 7.96 Hz), 1.37 (s, 9H)

N^1-methyl-N^4-(4-(trifluoromethyl)phenethyl)benzene-1,4-diamine hydrochloride salt (8a, KDS12017)

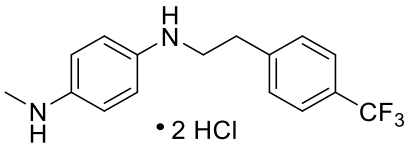

Using method B, *tert*-butyl methyl(4-((4-(trifluoromethyl)phenethyl)amino)phenyl)carbamate (316 mg, 0.80 mmol), 4.0M hydrochloric acid in dioxane (1.20 mL, 4.80 mmol) in dichloromethane (5 mL) to give 8a as an off white solid (270 mg, 92%); HPLC purity: 8.1 min, >99.9%; mp 246-250 °C; ^{1}H NMR (400 MHz, DMSO-d_6) δ 10.58 (br, 1H), 7.66 (d, 2H, J = 7.96 Hz), 7.50 (d, 2H, J = 7.92 Hz), 7.13 (s, 2H), 6.82 (s, 2H), 3.34 (t, 2H, J = 7.04 Hz), 2.96 (t, 2H, J = 7.40 Hz), 2.79 (s, 3H); ^{13}C NMR (100 MHz, DMSO-d_6) δ 144.51, 130.07, 129.81, 127.50 (q, $J_{C\text{-}F}$ = 31.63 Hz), 126.24, 125.62 (q, $J_{C\text{-}F}$ = 3.81 Hz), 123.54, 46.40 (**C**H_2), 35.74 (**C**H_2), 33.92 (**C**H_3)

N^1,N^1-dimethyl-N^4-(4-(trifluoromethyl)phenethyl)benzene-1,4-diamine hydrochloride salt (8b, KDS12008)

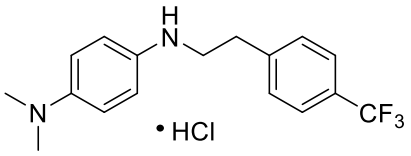

Using method B, N^1,N^1-dimethyl-N^4-(4-(trifluoromethyl)phenethyl)benzene-1,4-diamine (300 mg, 0.97 mmol), 4.0M hydrochloric acid in dioxane (0.73 mL) in dichloromethane (7 mL) to give 8b as an off white solid; HPLC purity: 8.0 min, 99.7%; mp 216-241 °C ^{1}H NMR (400 MHz, DMSO-d_6) δ 7.89 (b, 2H) 7.66 (d, 2H, J = 8.00), 7.51 (d, 2H, J = 7.96 Hz), 7.40 (s, 2H), 6.89 (s, 2H), 3.36 (t, 2H, J = 7.28Hz), 3.01 (s, 6H), 2.98 (t, 3H, J = 7.04 Hz); ^{13}C NMR (100 MHz, DMSO-d_6) δ 144.47, 130.07, 128.94, 127.50 (q, $J_{C\text{-}F}$ = 31.48 Hz), 126.24, 125.62 (q, $J_{C\text{-}F}$ = 3.45 Hz), 123.54, 46.21 (**C**H_2), 45.19 (**C**H_3), 33.90 (**C**H_2)

N^1-(2-methoxyphenethyl)-N^4-methylbenzene-1,4-diamine hydrochloride salt (8c, KDS12025)

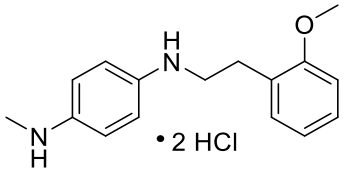

Using method B, *tert*-butyl (4-((2-methoxyphenethyl)amino)phenyl)(methyl)carbamate (586 mg, 1.64 mmol), 4.0M hydrochloric acid in dioxane (1.65 mL, 6.58 mmol) in dichloromethane (10 mL) to give 8c as a white solid (436 mg, 81%); HPLC purity: 6.8 min, 99.7%; mp 210-212 °C; ^{1}H NMR (400 MHz, DMSO-d_6) δ 7.25-7.17 (m, 3H), 7.09 (s, 2H), 6.98 (d, 1H, J = 8.04), 6.89 (t, 3H, J = 7.36 Hz), 3.80 (s, 3H), 3.24 (t, 2H, J = 7.12 Hz), 2.84 (t, 2H, J = 8.16 Hz), 2.79 (s, 3H); ^{13}C NMR (100 MHz, DMSO-d_6) δ 157.60, 130.42, 128.49, 126.16, 124.94, 124.79, 122.13, 120.86, 119.99, 111.19, 55.80(**C**H_3), 47.45(**C**H_2), 35.50(**C**H_2), 27.96(**C**H_3)

N^1-(3-methoxyphenethyl)-N^4-methylbenzene-1,4-diamine hydrochloride salt (8d)

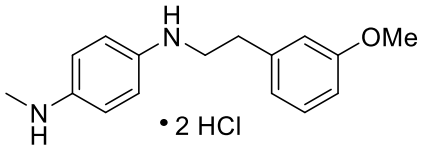

Using method B, *tert*-butyl (4-((3-methoxyphenethyl)amino)phenyl)(methyl)carbamate (240 mg, 0.67 mmol), 4.0M hydrochloric acid in dioxane (1.01 mL, 4.02 mmol) in dichloromethane (10 mL) to give 8d as a white solid (193 mg, 87%); HPLC purity: 6.7 min, >99.9%; mp 245-249 °C; ^{1}H NMR (400 MHz, DMSO-d_6) δ 9.18 (b, 4H), 7.29 (d, 2H, J = 7.29 Hz), 7.22 (t, 1H, J = 7.92 Hz), 7.16 (d, 2H, J = 7.84 Hz), 6.84-6.78 (m, 3H), 3.74 (s, 3H), 3.37 (t, 2H, J = 8.24 Hz), 2.92 (t, 2H, J = 7.44 Hz), 2.80 (s, 3H); ^{13}C NMR (100 MHz, DMSO-d_6) δ 159.82, 140.34, 129.92, 124.58, 124.46, 121.48, 121.33, 118.82, 114.75, 112.41, 55.44 (**C**H_3), 48.30 (**C**H_2), 35.34 (**C**H_2), 33.46 (**C**H_3)

N^1-(4-methoxyphenethyl)-N^4-methylbenzene-1,4-diamine (8e)

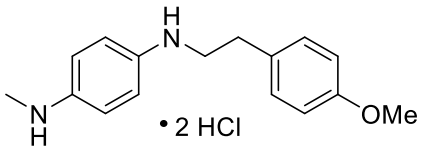

Using method B, *tert*-butyl (4-((4-methoxyphenethyl)amino)phenyl)(methyl)carbamate (586 mg, 1.64 mmol), 4.0M hydrochloric acid in dioxane (1.65 mL, 6.58 mmol) in dichloromethane (10 mL) to give 8e as a white solid (436 mg, 81%); HPLC purity: 6.6 min, 99.4%; mp 220-245 °C; ^{1}H NMR (400 MHz, DMSO-d_6) δ 10.10 (b, 4H), 7.34 (d, 2H, J = 8.56 Hz), 7.25 (d, 2H, J = 8.12 Hz), 7.18 (d, 2H, J = 8.48 Hz), 6.87 (d, 2H, J = 8.48 Hz), 3.72 (s, 3H), 3.34 (t, 2H, J = 8.28 Hz), 2.90 (t, 2H, J = 7.48 Hz), 2.81 (s, 3H); ^{13}C NMR (100 MHz, DMSO-d_6) δ 158.38, 13036, 130.12, 124.77, 124.64, 121.72, 119.86, 114.36, 55.50 (**C**H_3), 49.24(**C**H2), 35.33(**C**H_2), 32.28 (**C**H_3)

N^1-methyl-N^4-phenethylbenzene-1,4-diamine hydrochloride salt (8f)

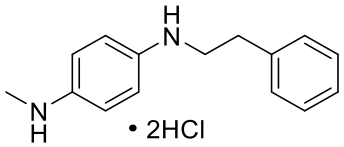

Using method B, *tert*-butyl methyl(4-(phenethylamino)phenyl)carbamate (160 mg, 0.49 mmol), 4.0M hydrochloric acid in dioxane (0.73 mL) in dichloromethane (5mL) to give 8f as an off white solid (111 mg, 76%); HPLC purity: 7.0 min, >99.9%; mp 246-247 °C; H NMR (400 MHz, DMSO-d_6) δ 10.32 (b, 1H), 7.33-7.26 (m, 4H), 7.24-7.20 (m, 1H), 7.08 (s, 2H), 6.88 (s, 2H), 3.31 (t, 2H, J = 7.40 Hz), 2.87 (t, 2H, J = 7.92 Hz), 2.78 (s, 3H)); ^{13}C NMR (100 MHz, DMSO-d_6) δ 139.1, 129.1, 128.9, 126.8, 121.0, 117.6, 47.7 (**C**H_2), 35.2 (**C**H_2), 33.8 (**C**H_3)

N^1-methyl-N^4-(3-(trifluoromethyl)phenethyl)benzene-1,4-diamine hydrochloride salt (8g)

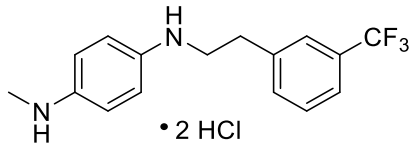

Using method B, *tert*-butyl methyl(4-((3-(trifluoromethyl)phenethyl)amino)phenyl)carbamate (395 mg, 0.34 mmol), 4.0M hydrochloric acid in dioxane (1.5 mL, 6.00 mmol) in dichloromethane (7 mL) to give 8g as an off white solid (351 mg, 96%); mp 210-246 °CHPLC purity: 7.8 min, >99.9%; mp 225-244 °C ^{1}H NMR (400 MHz, MeOD-d_4) δ 7.59-7.7.50 (m, 4H), 7.43 (d, 2H, J= 8.92 Hz), 7.30 (d, 2H, J = 6.84 Hz), 3.62-3.58 (m, 2H), 3.12 (t, 2H, J = 8.00 Hz), 3.30 (s, 3H); ^{13}C NMR (100 MHz, DMSO-d_6) δ 140.66, 133.55, 129.84, 125.84, 123.60, 122.06, 117.98, 47.55 (**C**H_2), 35.80 (**C**H_2), 33.43 (**C**H_3)

N^1-methyl-N^4-(2-(trifluoromethyl)phenethyl)benzene-1,4-diamine hydrochloride salt (8h)

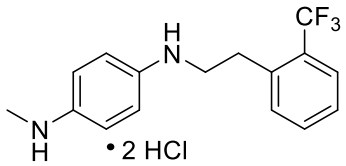

Using method B, *tert*-butyl methyl(4-((2-(trifluoromethyl)phenethyl)amino)phenyl)carbamate (80 mg, 0.20 mmol), 4.0M hydrochloric acid in dioxane (0.30 mL, 1.22 mmol) in dichloromethane (5 mL) to give 8h as an off white solid (53.1 mg, 72%); HPLC purity: 7.7 min, 99.2%; mp 221-246 °C; ^{1}H NMR (400 MHz, DMSO-d_6) δ 9.93 (b, 4H), 7.71 (d, 1H, J = 7.88 Hz), 7.65 (t, 1H, J = 7.48 Hz), 7.58 (d, 1H, J = 7.56 Hz), 7.46 (t, 1H, J = 7.48 Hz), 7.35 (d, 2H, J = 8.44 Hz), 7.08 (d, 2H, J = 7.96 Hz), 3.36 (t, 2H, J = 7.24 Hz), 3.11 (t, 2H, J = 7.20 Hz), 2.82 (s, 3H); ^{13}C NMR (100 MHz, DMSO-d_6) δ 137.36, 133.13, 132.21, 127.69 (q, $J_{C\text{-}F}$ = 32.55 Hz), 127.55, 126.27 (q, $J_{C\text{-}F}$ = 5.63 Hz), 124.91 (q, $J_{C\text{-}F}$ = 255.06 Hz), 122.50, 117.23, 47.13(**C**H_2), 35.94(**C**H_2), 30.65(**C**H_3)

Docking and Binding Energy calculations

Molecular modeling was performed using BIOVIA Discovery Studio software (*46*) under pH 7.4 and standard protocol settings if not specified otherwise. HRP and Hb protein structures were obtained from the protein databank (PDB ID 7ATJ (*47*), 2DN1 (*48*), respectively). In both systems, the heme iron Fe(IV)O state was set up, mimicking the HRP Compound II and ferryl Hb catalytic stages. In the HRP catalytic pocket, crucial crystal water molecule HOH1054 (*49*) was retained. Conversely, in the Hb catalytic pocket, a hydrogen peroxide molecule was placed 2.6 Å under the porphyrin ring pyrrole and within 2.2 Å of both the oxo-iron and distal histidine (H58 and H63 in α and β chains, respectively). Small molecule docking was performed using the CDOCKER protocol. In the HRP protein system, compounds KDS12025 and HTPEB were docked into the catalytic binding site, and the robustness of the docking protocol was verified

through the successful re-docking of ferulic acid within 1.5 Å of the co-crystallized ligand pose. For Hb, multiple binding sites in the Hbα and Hbβ subunits of the Hb tetramer were explored, guided by prior published Hb-small molecule docking studies (*50-54*).
The ligand binding energy (ΔG_{bind}) for the top 5 docking poses was determined using the MM-GBSA method under the Generalized Born with Molecular Volume (GBMV) solvent model and additionally, *in situ* ligand minimization was included in the protocol, where all protein residues within 6 Å of the ligand were treated as flexible.

Binding affinity assay

All ITC experiments were conducted using a MicroCal Auto-iTC200 (Malvern Panalytical) at the Korea Basic Science Institute (Ochang, Korea). Binding affinity was measured using 40 µl of 1 mM KDS12025 and 200 µl of 0.1 mM purified human Hb in sodium phosphate buffer (pH 7). For each titration experiment, 2 µl of KDS12025 was injected into purified human Hb for 4 s at intervals of 150 s at 25 °C. Overall, 19 injections were performed for each experiment and the data were analyzed using MicroCal Origin 7.0 software.

Bubbling liberation

CAT, HRP, and Hb were reacted with H_2O_2 to assess the increase in oxygen production through bubbling liberation. The reaction mixture was placed on a cover slide and observed under a microscope for counting bubbles. Bubbles were quantified in a 1 x 1 mm^2 area using ImageJ (NIH) software. The effect of vehicles (DMSO), HTPEB, and KDS12025 on the enhancement of bubbling liberation was evaluated to determine their impact on the enzymatic reaction. To quantitatively measure the difference in bubbling liberation, CAT, HRP, and Hb were mixed with H_2O_2 in sealed tubes. Additional conditions included the presence of DMSO, HTPEB, or KDS12025. These tubes were connected via tubing to an inverted cylinder submerged in a water bath with minimal air, creating a closed system. The time and volume of the produced bubbles were recorded.
To examine the macroscopic effects of various treatments on oxygen liberation, a visual bubble formation assay was conducted. CAT was prepared at concentrations of 10 mg/ml and 0.08 mg/ml. H_2O_2 was added to each CAT solution at approximate concentrations of 10 M and 0.1 M. For each reaction, vehicle control, KDS12025, and HTPEB were administered to assess their influence on the reaction dynamics. A similar procedure was followed for Hb at identical concentrations to CAT, with a vehicle, KDS12025, and HTPEB treatments. The mixtures were then visually monitored for bubble formation to qualitatively assess the catalytic breakdown of H_2O_2 and the resultant oxygen release.

Off-target selectivity assay

The possibility of KDS12025 on kinase off-target, the KINOMEscan panel of scanEDGE assay was conducted in DiscoverX (CA, USA) using a site-directed competition binding with the test compounds. The assay results are given in table S4 and experimental information is available on the DiscoverX web page (www.discoverx.com). Moreover, the Delta SafetyScreen87 panel assay was conducted in Eurofins Discovery (Cerep, France). The assay results are given in table S5 and experimental information is available on the DiscoverX web page (https://www.eurofinsdiscoveryservices.com).

BBB-permeability test

A parallel artificial membrane permeability assay (PAMPA) was performed to validate the blood-brain barrier permeability of KDS12025. The procedure began by preparing a donor

solution of the compound in a pH 7.4 donor buffer. This solution was added to the wells of a deep well plate, followed by the addition of a high-sensitivity UV plate filled with donor buffer to serve as the blank sample. An initial sample for the UV plate was taken to establish a baseline reading. The PAMPA sandwich was then assembled by adding the donor plate mixture to the donor plate well, followed by placing a BBB-lipid coated membrane on top and an acceptor plate filled with acceptor buffer. This setup was incubated at 25°C for a specific duration to allow diffusion. Post-incubation, a sample from the acceptor plate was taken, and the UV absorbance was measured to determine the permeated amount of the test compound. The permeability was then calculated using the PAMPA explorer program, considering the initial donor concentration and the acceptor's concentration after incubation.

Cultured primary astrocytes

Primary hippocampal astrocytes were obtained from either postnatal day 0-2 (P0-2) C57BL/6 mice as previously described (*55*). The hippocampal tissue was dissected free of meninges, minced, and dissociated into a single-cell suspension by trituration. Cells were grown in Dulbecco's modified Eagle's medium supplemented with D-glucose (4500 mg/L), L-glutamine, sodium pyruvate (110 mg/L), 10% heat-inactivated horse serum, 10% heat-inactivated fetal bovine serum, and 1000 U/ml penicillin-streptomycin. Cells were maintained at 37 °C in a humidified atmosphere containing 5% CO_2.

Oligomerized $A\beta_{42}$ aggregates

Amyloid-beta $(A\beta)_{42}$ monomers (Abcam; DAEFRHDSGYEVHHQKLVFFAEDVGSNK GAIIGLMVGGVVIA) were dissolved to 1 mM in 1% ammonium hydroxide. $A\beta_{42}$ monomers were further diluted to 100 μM in Phosphate Buffered Saline (PBS). The solution was incubated at a 4°C rocker for 24 hours and stored at -80°C for further use as an aggregated form of $A\beta_{42}$ as previously described (*25, 56*).

Intracellular H_2O_2 detection

Intracellular H_2O_2 levels of astrocytes were determined using 2′,7′- dichlorodihydrofluorescein diacetate (DCFDA, Thermofisher). Primary cultured astrocytes were seeded onto 96-well black plates (ibid, USA) and incubated with oligomerized $A\beta_{42}$ in the presence of 10 μM KDS12008, 17, 25, HTPEB, and sodium pyruvate (10 mM). Then these cells were washed with Ca^{2+} and Mg^{2+} contained PBS, followed by the application of 30 μM DCFDA and incubated at 37°C for 30 minutes. The mean intensity of fluorescence was measured using iD5 microplate readers at ex/em=485/530 nm.
H_2O_2-specific, high sensitivity, and fast on-and-off kinetics, genetically encoded oROS-G plasmid, kindly provided by Dr. Andre Berndt. The oROS-G was cloned under the GFAP104 promoter, and delivered into primary cultured hippocampal astrocytes using the NeoN™ transfection system (Invitrogen). Astrocytes were plated in 96-well black plates (ibid) and fluorescence changes were measured using an iD5 microplate reader for endpoint analysis or imaged over 40 hours using an A1 Nikon confocal microscope for live cell imaging.

Mouse

All mice, including both male and female, were grouped-housed in a temperature- and humidity-controlled environment with a 12-hour light/dark cycle. Handling and animal care were performed according to the Institutional Animal Care and Use Committee of the Institute for Basic Science (IBS-2023-006, Daejeon, Korea). For an animal model of AD, both sexes of 10 to 18-month-old APP/PS1 mice were maintained and used as previously described (*57, 58*).

For testing the novel H_2O_2-decomposing enhancers effect in the AD model, mice were treated by i.p. injection with KDS12008 (3 mg/kg/day), KDS12017 (3 mg/kg/day), and KDS12025 (3 and 10 mg/kg/day) once per day for one or two weeks depends on experimental protocol. All drugs were dissolved in 200 µl of saline, and the amount of each drug was calculated based on the weight (kg) of the mouse. Moreover, oral administration of KDS12025 (3 mg/kg/day) in the AD model for two weeks *ad libitum*. Both sexes of 8 to 10-week-old C57BL/6J mice were used for PhenoMaster (TSD systems, Germany). GFAP-CreERT2/iDTR (GiD) lines were maintained by crossing iDTR transgenic mice with GFAP-CreERT2. All mice were randomly distributed into different groups with matched ages.

Passive avoidance test

Sufficiently handled mice were ready before the PAT. Mice were placed in the two-compartment (light and dark) shuttle chamber with a shock generator (Ugo Basile, Italy). On the first day, mice were placed in the light compartment for the acquisition. Mice were allowed to explore the light compartment for 60 seconds, after which the door separating the light and dark compartments was raised to allow the mice to enter the dark compartment. When the mice entered a dark compartment, the separating door was closed immediately and an electrical foot shock (0.5 mA, 2 s duration) was delivered through the floor grid. Then, the mice were moved back to the home cage and the retention trial was followed 24 hours after the acquisition. On the second day, the mice were again placed in the light compartment for the retention trial. After 60 seconds, the door was raised to allow the mice to enter the dark compartment. The latency to step through the dark compartment before and after the electric shock was recorded for up to 540 seconds.

Novel place recognition

Before the novel place recognition (NPR) test, mice underwent sufficient handling and were concurrently habituated to an open field test (OFT) in a square chamber (40 cm x 40 cm x 40 cm). After the habituation, mice were placed in the open field with two identical objects positioned in the first and second quadrants of the cage. Mice were free to explore the objects for 10 min and returned to the home cage for 1 hour. To test spatial recognition memory, one of the two identical objects was placed in a novel place (quadrant) and the mice were re-entered into the open field chamber for 10 min. The discrimination index (DI) was calculated as the percentage of time spent on the novel place over the total time spent on both the novel and the familiar place.

Open field test

For the open field test (OFT), all the mice were placed in an acrylic container (40 cm x 40 cm x 40 cm) for a 10-minute acclimation period. The field was segmented into central (12 cm x 12 cm) and peripheral zones for analysis. Travel distance, center zone duration, and frequency were quantified using Ethovision XT software (Noldus, Netherlands).

Respiration and metabolic analysis

For respiration and metabolic analysis, PhenoMaster (TSE systems, Germany) was employed. All C57BL/6J mice aged 8 to 10 weeks old underwent an initial chamber habituation and gas calibration on day 0. Starting on day 3, the mice were administered KDS12025 dissolved in water at dosages of 10, 1, and 0.1 mg/kg/day. Respiratory and metabolic measurements, including oxygen consumption, carbon dioxide production, respiratory exchange ratio (RER,

calculated as VCO2/VO2), as well as food and drink intake and energy expenditure, were conducted from day 4. The recording ends on day 8 with data collection.

Virus and diphtheria toxin injection

Mice were deeply anesthetized with vaporized 1% isoflurane and placed into stereotaxic frames (RWD Life Science, China). Following an incision on the midline of the scalp, a hole was drilled into the skull above the hippocampus. AAV-GFAP104-GFP or AAV-GFAP104-DTR-GFP were bilaterally microinjected into the hippocampus CA1 (AP, -2.0 mm; ML, ± 1.5 mm; DV, -1.65 mm from the bregma). Diphtheria toxin (2 mg/ml) was administered for 16 days as previously described (*58*). For shRNA knockdown, AAV-pSicoR-Hbβ-shRNA-mCherry or AAV-pSicoR-Sc-shRNA-mCherry were microinjected into the same coordinate. A total of 0.8 µl of the virus was injected using a syringe pump (KD Scientific, USA). The procedures of injection were implemented before 5 weeks of the experiments. All viruses used in this study were produced at the Institute for Basic Science virus facility (IBS virus facility, Korea). To investigate the 0.1 mg/kg/day effects of KDS12025, GiD mice were injected with diphtheria toxin (2 mg/ml) daily for 16 days. Concurrently, KDS12025 was administered *ad libitum* (0.1 mg/kg/day) during the same period.

Immunohistochemistry

Mice were deeply anesthetized with 2% avertin and positioned at the operating table. After opening up the abdomen and exposing the heart, perfused with saline followed by 4% paraformaldehyde (PFA). Decapitate the mice and the brains were excised from the skull. Excised brains were postfixed in 4% PFA overnight at 4°C and dehydrated in 30% sucrose for 48 h. Coronal hippocampal sections were cut at 30 µm-thickness in a cryostat and stored in a storage solution. The sections were fully washed in 0.1 M PBS and incubated for 1 h in a blocking solution (0.3% Triton X-100, 2% donkey and goat serum in 0.1M PBS). Next, a mixture of primary antibodies in the blocking solution was immunostained on a shaker overnight at 4°C. Sections were washed in PBS three times. After washing, sections were incubated with the corresponding fluorescent secondary antibodies for 1 h at RT. DAPI staining was done by adding a DAPI solution (1:2000) during the second washing step. After finishing the washing step, the sections were mounted on the cover slide with a mounting medium. A series of fluorescent images were obtained with a LSM900 (Zeiss, Germany) confocal microscope or Lattice SIM Elyra 7 (Zeiss, Germany). Image analysis was done by the ImageJ (NIH) program. Primary antibodies were diluted to the following amounts: chicken anti-GFAP (1:500, Millipore, ab5541), rabbit anti-amyloid beta (1:500, Abcam, ab2539), mouse anti-NeuN (1:200, Millipore, ab377), rabbit anti-Hbβ (1:200, Abcam, ab214049), mouse anti-Hbβ (1:200, Santacruz, sc-21757). Secondary antibodies from Jackson were diluted (1:500) in the blocking solution.

Sholl analysis and neuron counting

Serial confocal sections immunolabeled with GFAP were compiled into a maximal projection. This projected image was utilized to assess the GFAP signal within the hippocampus. Utilizing the Sholl analysis plugin in ImageJ, concentric circles with 10-µm spacing were automatically generated from the nucleus to the furthest astrocytic process. This analysis quantified the intersections of GFAP-labeled processes within each circle and calculated the ramification index and the ending radius. In the focal GiD mouse model, the NeuN was quantified within a 50 μm^2 region using ImageJ for counting the number of CA1 pyramidal neurons.

Imaris software

Raw image files were used for further analysis using Imaris software (Oxford Instruments). Manual surface reconstruction was performed based on masking GFAP, and Hbβ-positive signals in the stratum radiatum of the hippocampus. The parameters were surface details (0.6 μm); diameter of the largest sphere (2 μm); manual threshold value min (1000) diffusion transparency: 60%. After reconstruction from Imaris software, Hbβ-positive signals in the GFAP surface were quantified.

Electrophysiology

Mice were deeply anesthetized with 3% isoflurane followed by decapitation. The brain was quickly excised from the skull and submerged in a chilled cutting solution that contained 234 mM of sucrose; 24 mM of NaHCO3; 11 mM of d(+)-glucose; 10 mM of MgSO4; 2.5 mM of KCl; 12.5 mM of NaH2PO4; and 0.5 mM of CaCl2. Transverse hippocampal (300 μm thick) were prepared with a vibrating microtome (PRO7N; DSK) and transferred to an artificial cerebrospinal fluid (aCSF) solution that contained 130 mM of NaCl; 24 mM of NaHCO3; 1.25 mM of NaH2PO4; 3.5 mM KCl; 1.5 mM of CaCl2; 1.5 mM of MgCl2; and 10 mM of d(+)-glucose, pH 7.4. Slices were incubated at RT for at least 1 h before recording. All solutions were saturated with 95% O2 and 5% CO2.

For a recording of tonic GABA currents, slices were transferred to a recording chamber that was mounted on an upright Zeiss microscope and continuously perfused with the aCSF solution. The slice was viewed with a 60x water immersion objective (numerical aperture= 90) with infrared differential interference contrast optics. Cellular CMOS camera (Hamamatsu Photonics, Japan). Cellular morphology was visualized by a CMOS camera (Hamamatsu Photonics, Japan) and Imaging Workbench software (INDEC Biosystems). Whole-cell patch recordings were made from pyramidal neurons located in the DG granule cells of the hippocampus. The holding potential was -70 mV. Pipette resistance was typically 6–8 MΩ and the pipette was filled with an internal solution that contained (in mM): 135 CsCl; 4 NaCl; 0.5 CaCl2; 10 HEPES; 5 EGTA; 2 Mg-ATP; 0.5 Na2-GTP; 10 QX-314; pH-adjusted to 7.2 with CsOH (278 to 285 mOsmol). The baseline current before measuring tonic current was recorded with CNQX (20 μM) and D-AP5 (50 μM). The frequency and amplitude of spontaneous inhibitory postsynaptic currents before bicuculline (50 μM) administration were detected and measured by Mini Analysis (Synaptosoft, USA).

Dentate granule cells' synaptic responses were elicited at a low frequency of 0.1 Hz by stimulating perforant path fibers. The stimulation was delivered over 100 ms at intensities ranging from 0 to 1,000 μA using a constant current isolation unit. A tungsten bipolar electrode was positioned in the molecular layer to stimulate the perforant path fibers. Recordings of the evoked excitatory postsynaptic potentials (EPSPs) were typically 6–8 MΩ and the pipette was filled with an internal solution that contained (in mM): 120 potassium gluconates; 10 KCl; 1 MgCl2; 0.5 EGTA; 40 HEPES; pH-adjusted to 7.2 with KOH. The spiking probability was determined by the number of spikes generated per total stimulation. Electrical signals were digitized and sampled at 10-ms intervals with the Digidata 1550B data acquisition system and the Multiclamp 700B Amplifier (Molecular Devices, USA) using the pClamp software.

Hbβ shRNA vector and reverse transcription-PCR

The shRNA sequence for *hbb* was designed with a Broad Institute designer (UK). shRNA for mouse *hbb* (NM_001278161.1) was targeted at nucleotides (5'-gagcatctgtcagttgttggc-3') and inserted into the pSico and pSicoR system (*59*). shNRA sequence is 5'-ggttaattgttcccaagagag-3'. Gene silencing of *hbb* was tested by reverse transcription-PCR (5'-gcacctgactgatgctgaga-3'). For gene silencing of *hbb*, adenovirus-associated virus (AAV) carrying Hbβ-shRNA was transfected into primary cultured astrocytes. 4 days after infection, the total RNA was prepared

using an AllPrep RNA kit (Qiagen, Netherlands) and cDNA was synthesized by SuperScript III Reverse Transcriptase (Invitrogen, USA).

Western blot

Western blotting was conducted following established protocols. Membranes were probed with primary antibodies targeting Hbβ and GAPDH overnight at 4 °C. Post three washes in Tris-buffered saline containing 0.05% Tween 20, blots were incubated with HRP-conjugated secondary antibodies for 2 hours at room temperature. Bands were detected using Immobilon Western ECL solution and captured on an Image Station 4000MM.

Immunohistochemistry with Double Chromogenic Staining

Human brain samples

Neuropathological examination of postmortem brain samples from normal subjects and AD patients was determined using procedures previously established by the Boston University Alzheimer's Disease Center (BUADC). Next of kin provided informed consent for participation and brain donation. Institutional review board approval for ethical permission was obtained through the BUADC center. This study was reviewed by the Institutional Review Board of the Boston University School of Medicine and was approved for exemption because it only included tissues collected from post-mortem subjects not classified as human subjects. The study was performed in accordance with institutional regulatory guidelines and principles of human subject protection in the Declaration of Helsinki. The sample information is listed in table S6.

First staining

Paraffin-embedded human postmortem brain tissues were sectioned in a coronal plane at 10μm. BLOXALL® Blocking solution (Vector Laboratories, Burlingame, CA, USA) was used to block endogenous alkaline phosphatase. Hippocampal tissue sections were blocked with 2.5% normal horse serum (Vector Laboratories) for 1 h and then incubated with GFAP antibody (1:400, AB5541, Millipore, Burlington, MA, USA) for 24 h. After washing three times with PBS, tissue slides were processed with Vector ABC Kit (Vector Laboratories, Burlingame, CA, USA). The GFAP immunoreactive signals were developed with DAB chromogen (Thermo Fisher Scientific, Meridian, Rockford, IL, USA).

Second staining

Tissue slides stained with GFAP were incubated with hemoglobin beta (Hbβ) antibody (1:50, sc-21757, Santa Cruz) for 24 h. After reaction with secondary antibodies, sections were incubated with ImmPRESS-AP anti-mouse IgG (alkaline phosphatase) polymer detection reagent (Vector Laboratories: MP-5402) for 2 h at room temperature. A Vector Blue alkaline phosphatase substrate kit (Vector Laboratories: SK-5300) was used to develop HBβ signals. Double-stained tissue slides were gradually processed back to Histo-clear (HS-200) through an increasing ethanol gradient [70%, 80%, 90%, 95%, and 100% (1 time)] and subsequently mounted. The chromogenic signals of GFAP (brown) and Hbβ (blue) were examined under a light microscopy (BX63) (Olympus, Japan) equipped with high definition (1920 x 1200 pixel) digital camera (DP74) (Olympus, Japan).

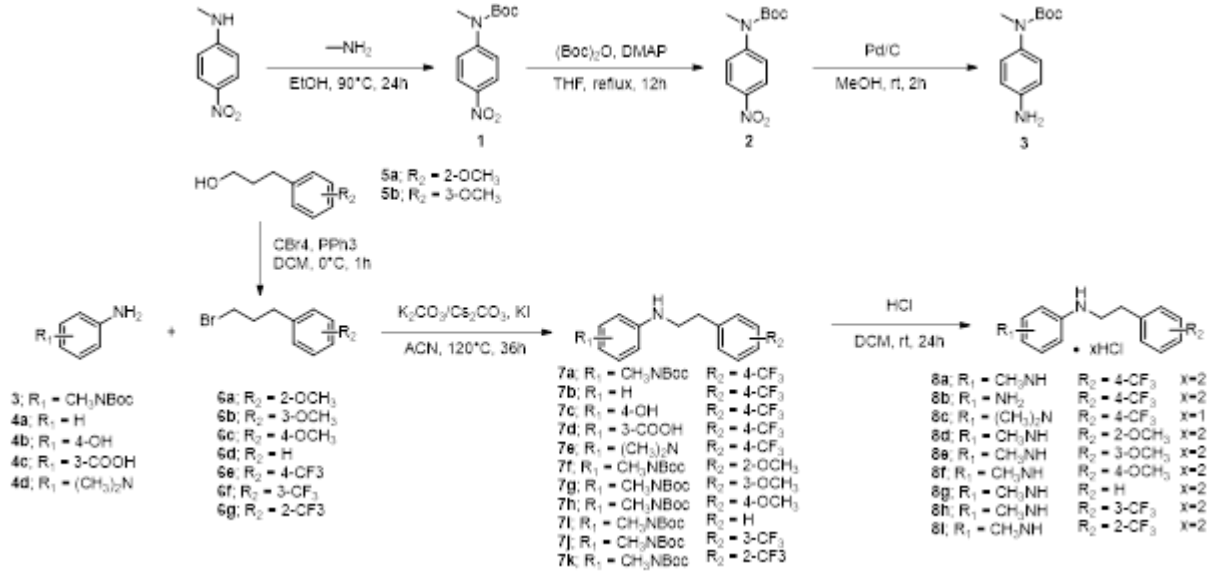

fig. S1. General Procedure for preparation of KDS compounds. Synthetic procedures for preparation of intermediates and KDS compounds.

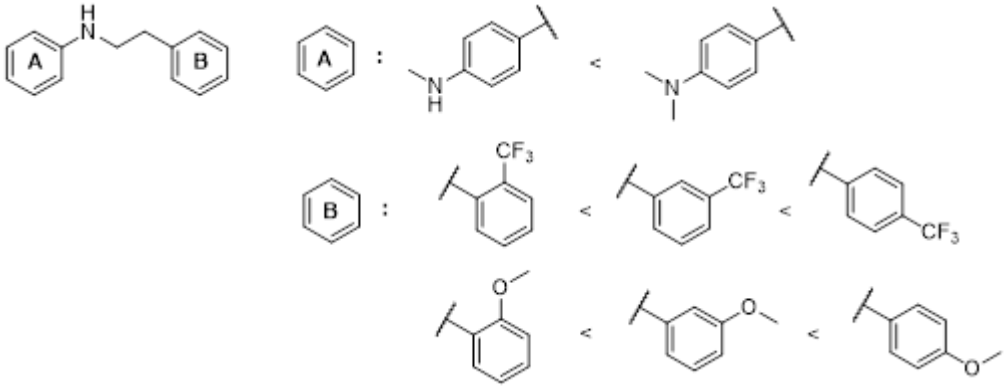

fig S2. Structure-activity relationship of the synthesized compounds. Structure-activity relationship activity is derived from the Amplex Red assay system. A comparison of synthesized KDS compounds indicates that A ring *N*-methylaniline is more potent than *N,N*-dimethylaniline, as well as B ring methoxy compounds are more potent than trifluoromethyl counterparts.

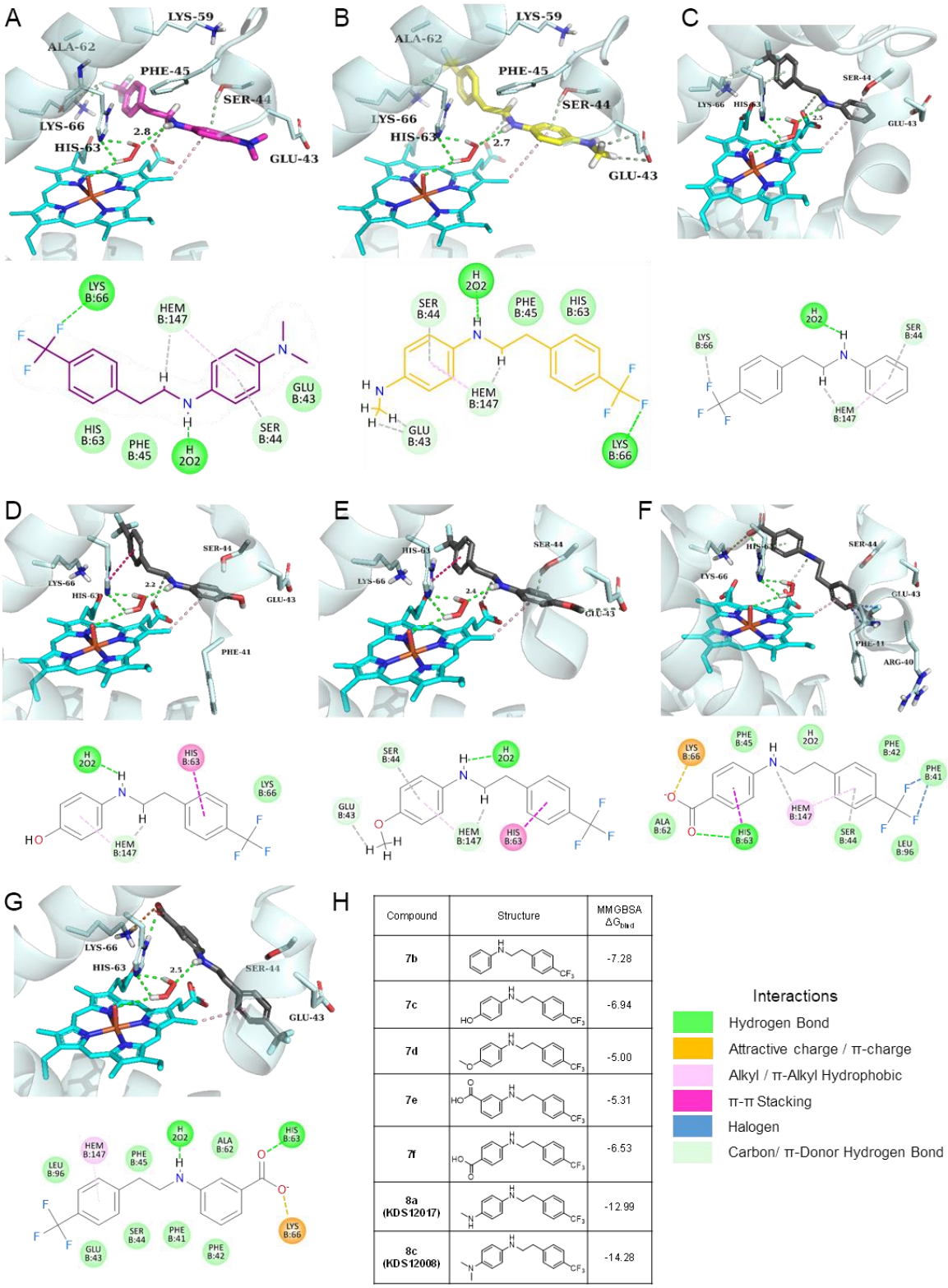

Compound	Structure	MMGBSA ΔG_{bind}
7b		-7.28
7c		-6.94
7d		-5.00
7e		-5.31
7f		-6.53
8a (KDS12017)		-12.99
8c (KDS12008)		-14.28

fig. S3 Binding modes of selected *N*-phenethylaniline compounds in Hbβ chain. (A to G) Predicted 3D binding mode and 2D interaction map of compounds KDS12017 (A), KDS12008 (B), 7b (C), 7c (D), 7d (E), 7f (F) and 7e (G) in the hemoglobin β-subunit. (H) Binding energy (ΔG_{bind}) values for corresponding compounds, calculated by the MMGBSA method.

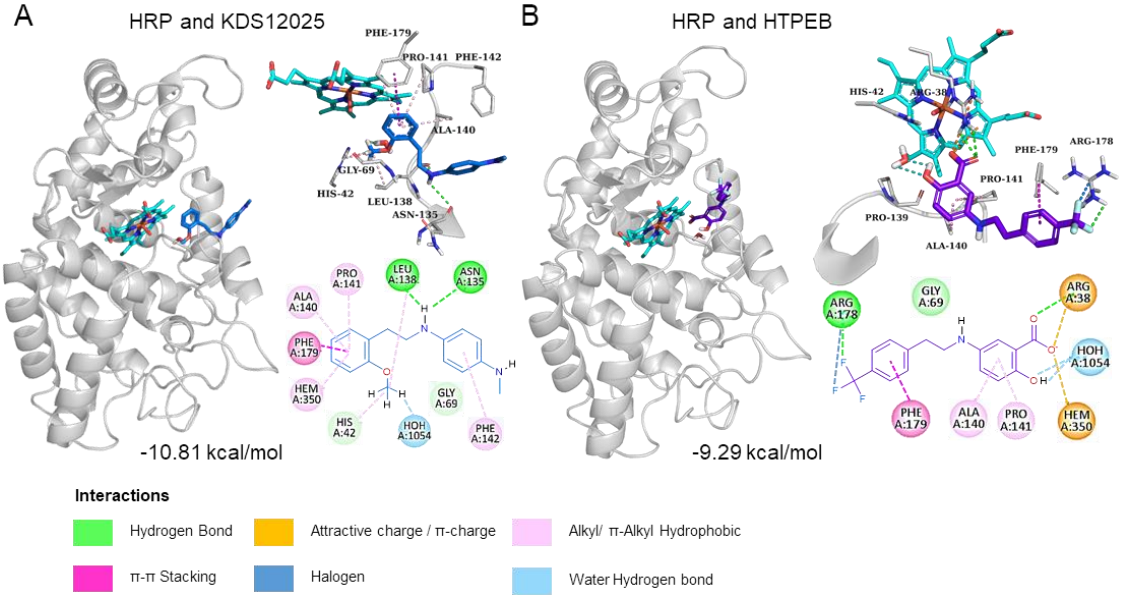

fig. S4 Binding modes of selected active compounds in HRP proposed by molecular docking. (A and B) General view of protein-ligand binding (left), 3D interaction scheme (top right), and 2D interaction map (bottom right) of compounds KDS12025 (A) and HTPEB (B). The calculated binding energy (ΔG_{bind}) values for each compound binding event are specified at the bottom center.

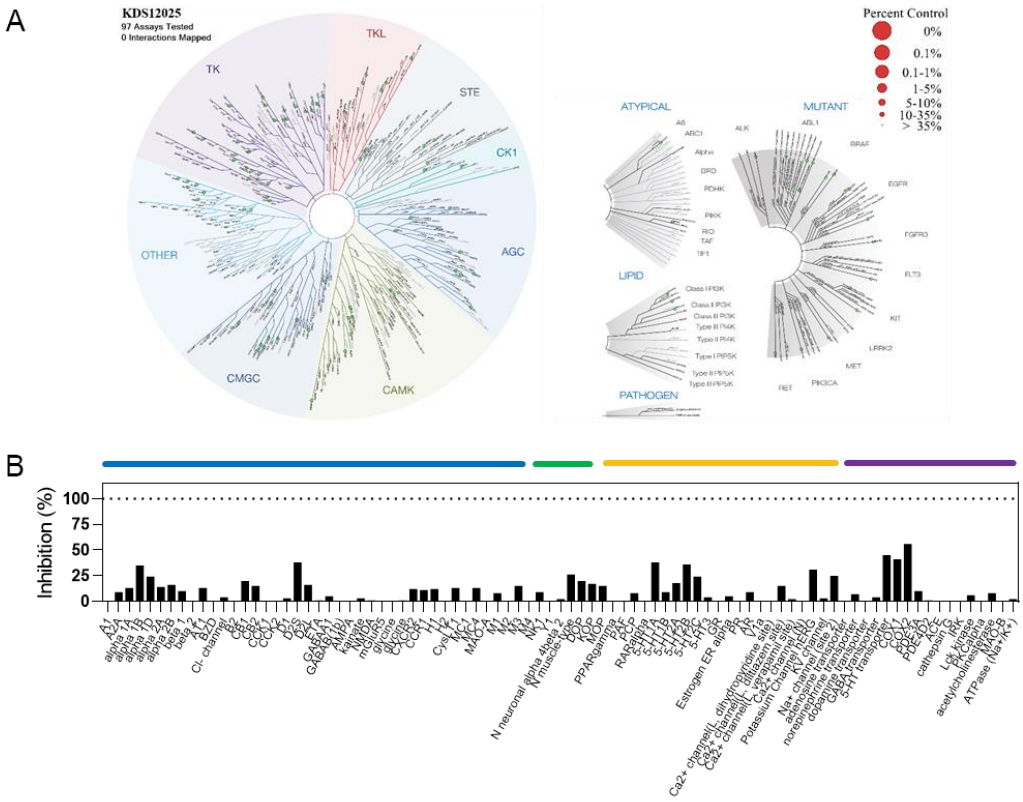

fig. S5. KINOMEscan and Off-target Selectivity Screening Results for KDS12025 at 1000 nM. (A) Schematic diagram of KINOME*scan*™ screening results categorizing human kinases and disease-associated mutant variants. Competitive binding assays for 97 human kinases were performed at 1000nM KDS12025 and the amount of inhibition through control ligand reaction is expressed as the size of the colored circle (green/red). Zero interactions mapped means there are no meaningful responses with ≥ 50% inhibition. TK, Tyrosine Kinase; TKL, Tyrosine Kinase Like; STE, Yeast STE-MAPK family; CK1, Casein Kinase 1; AGC, PKA, PKG, PKC family; CAMK, Calmodulin/Calcium regulated kinases; CMGC, CDK, MAPK, GSK3 and CLK; see table S5 for detailed results. **(B)** The off-target selectivity for 87 primary molecular targets at 1000 nM of KDS12025 including G protein-coupled receptors (GPCRs), kinases, non-kinase enzymes, nuclear receptors, transporters, and various ion channels; see table S4 for detailed results.

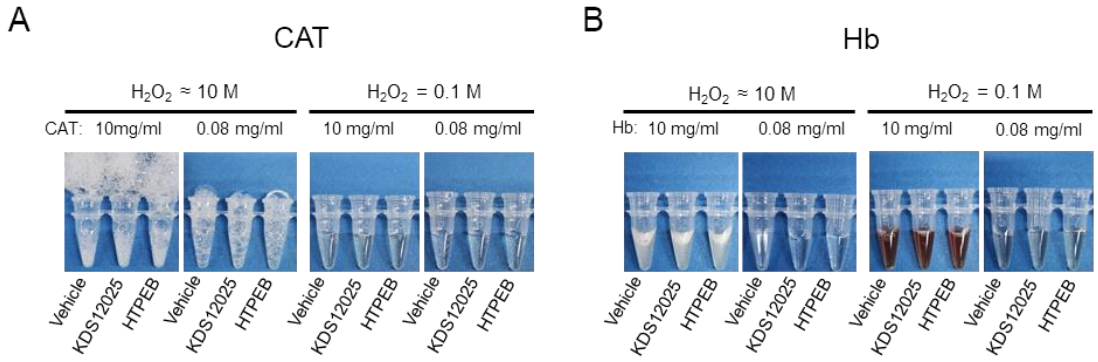

fig S6. Oxygen liberation of CAT and Hb. (A and B) The assay shows oxygen release from CAT (A) and Hb (B) under varied conditions, with observable changes that indicate the degree of oxygen liberation.

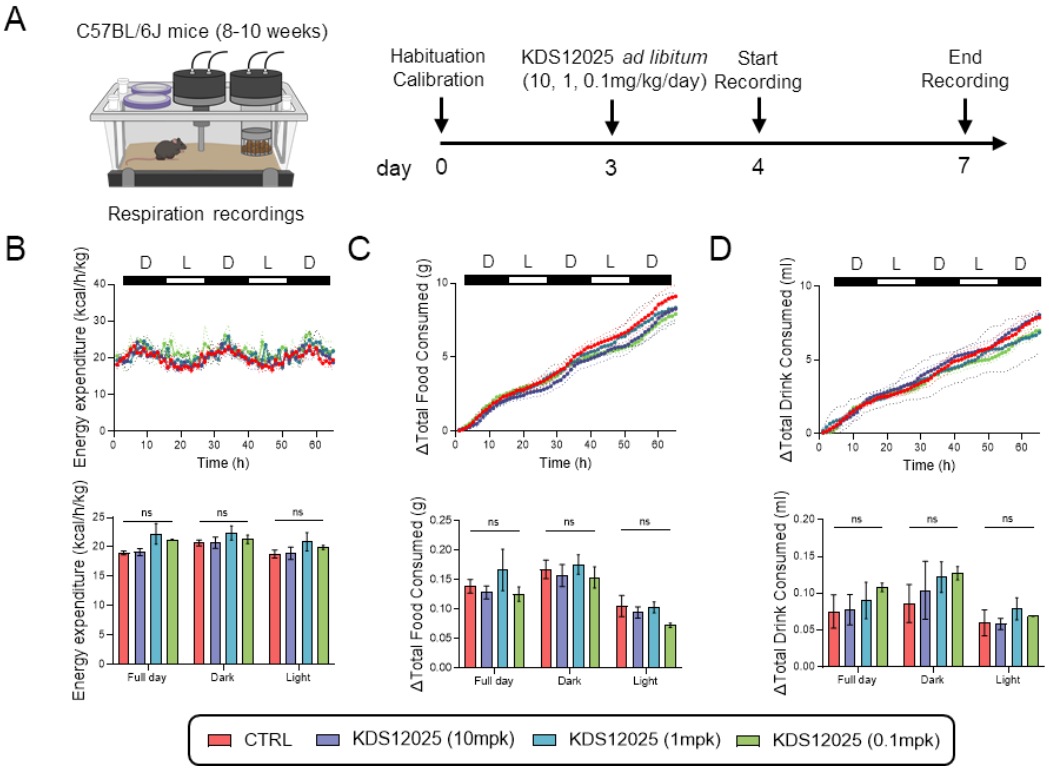

fig S7. Absence of KDS12025 effect on metabolism. (A) Timeline of Phenomaster experiments with the administration of KDS12025 (10, 1, 0.1 mg/kg/day). **(B)** Measurement of energy expenditure (kcal/h/kg) during the administration of KDS12025 at concentrations of 10, 1, and 0.1 mg/kg for both day (dark, 'D') and night (light, 'L') cycles, accompanied by a summary graph. **(C)** Measurement of total food consumption (g) during the 'D' and 'L' cycles. **(D)** Measurement of total drink consumption (ml) during the 'D' and 'L' cycles. Data are presented as the mean ± s.e.m. ns, not significant. Additional statistics are provided in table S7.

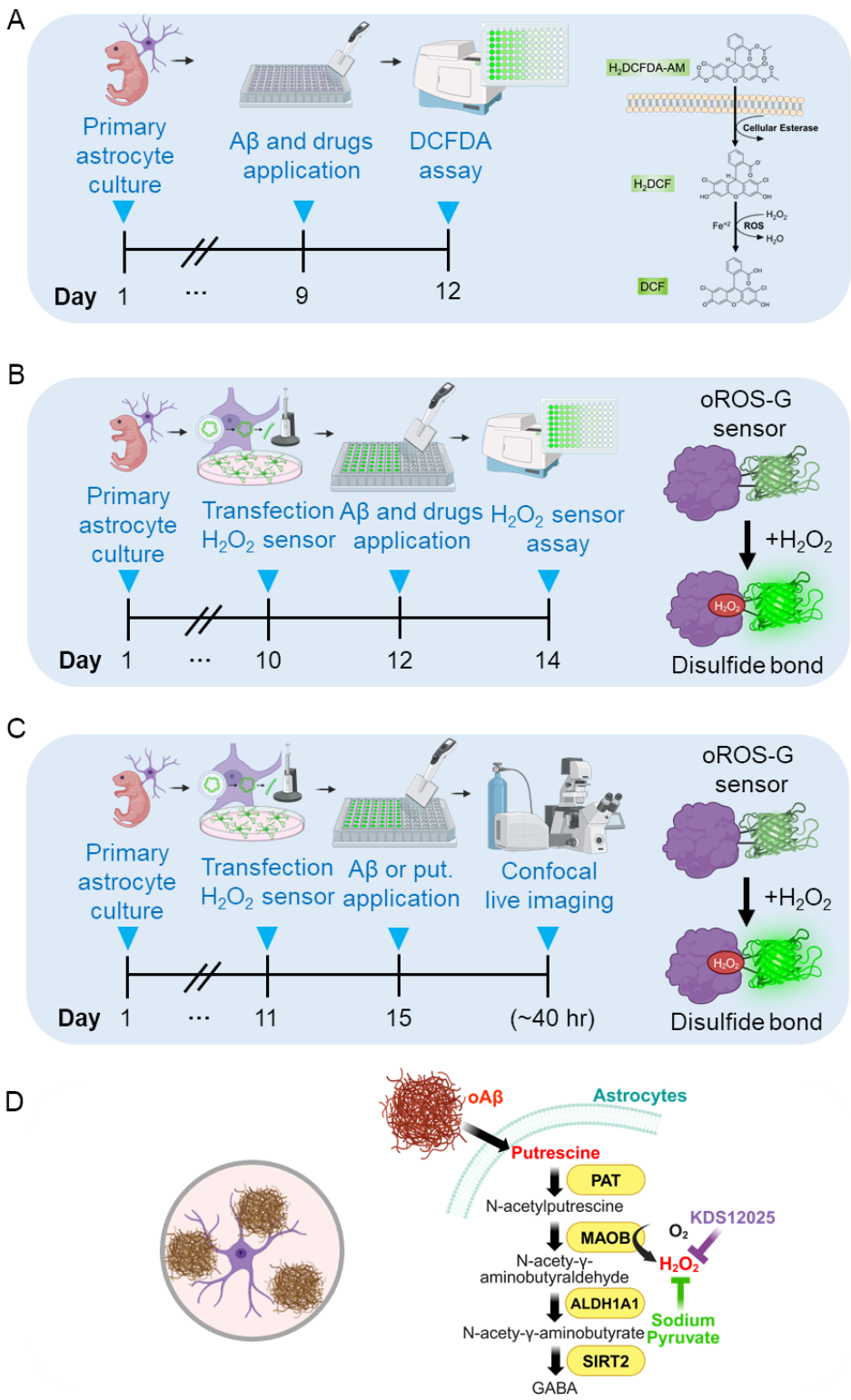

fig. S8. Timeline and schematic images of aberrant H_2O_2 in astrocytes. (A) Timeline and schematic diagram of DCFDA-based H_2O_2 assay. **(B)** Timeline and schematic diagram of newly developed H_2O_2-selective cpGFP sensor, oROS-G. **(C)** Timeline of 40-hour live H_2O_2 imaging using oROS-G probe in Aβ or putrescine incubated cultured astrocytes. **(D)** Schematic diagram of Aβ or putrescine-induced aberrant H_2O_2 in astrocytes.

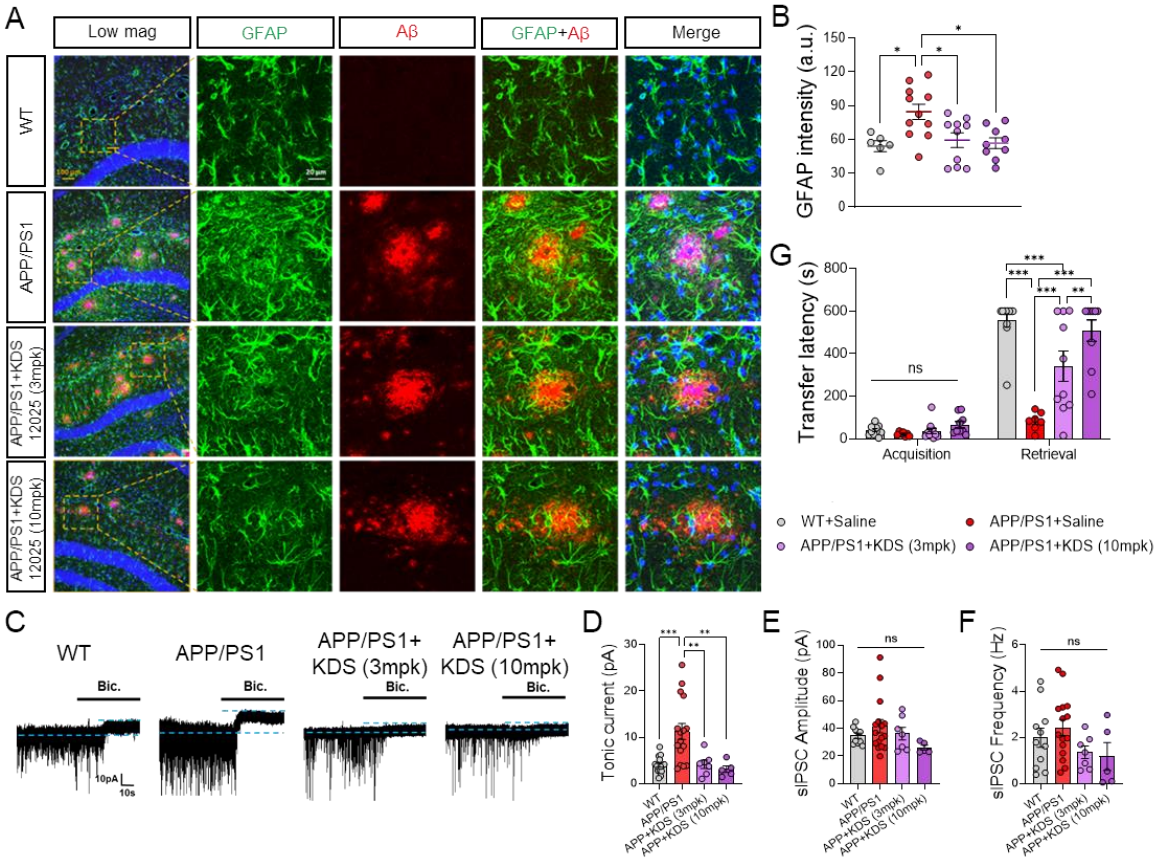

fig S9. 10mg/kg/day of KDS12025 also alleviates the AD symptoms. (A) Representative immunostaining image for GFAP and Aβ after 3 and 10 mg/kg/day i.p. injection of KDS12025 **(B)** Mean intensity of GFAP in GFAP-positive area. **(C)** Representative trace of $GABA_AR$ mediated-tonic GABA current recorded from granule cells in APP/PS1 mice. **(D)** Tonic GABA current measured from granule cells. **(E and F)** Amplitude (E) and frequency (F) of sIPSC measured from granule cells. **(G)** Transfer latency to enter the dark chamber during the PAT. Data are presented as the mean ± s.e.m. *P < 0.05, **P < 0.01, ***P < 0.001; ns, not significant. Additional statistics are provided in table S7.

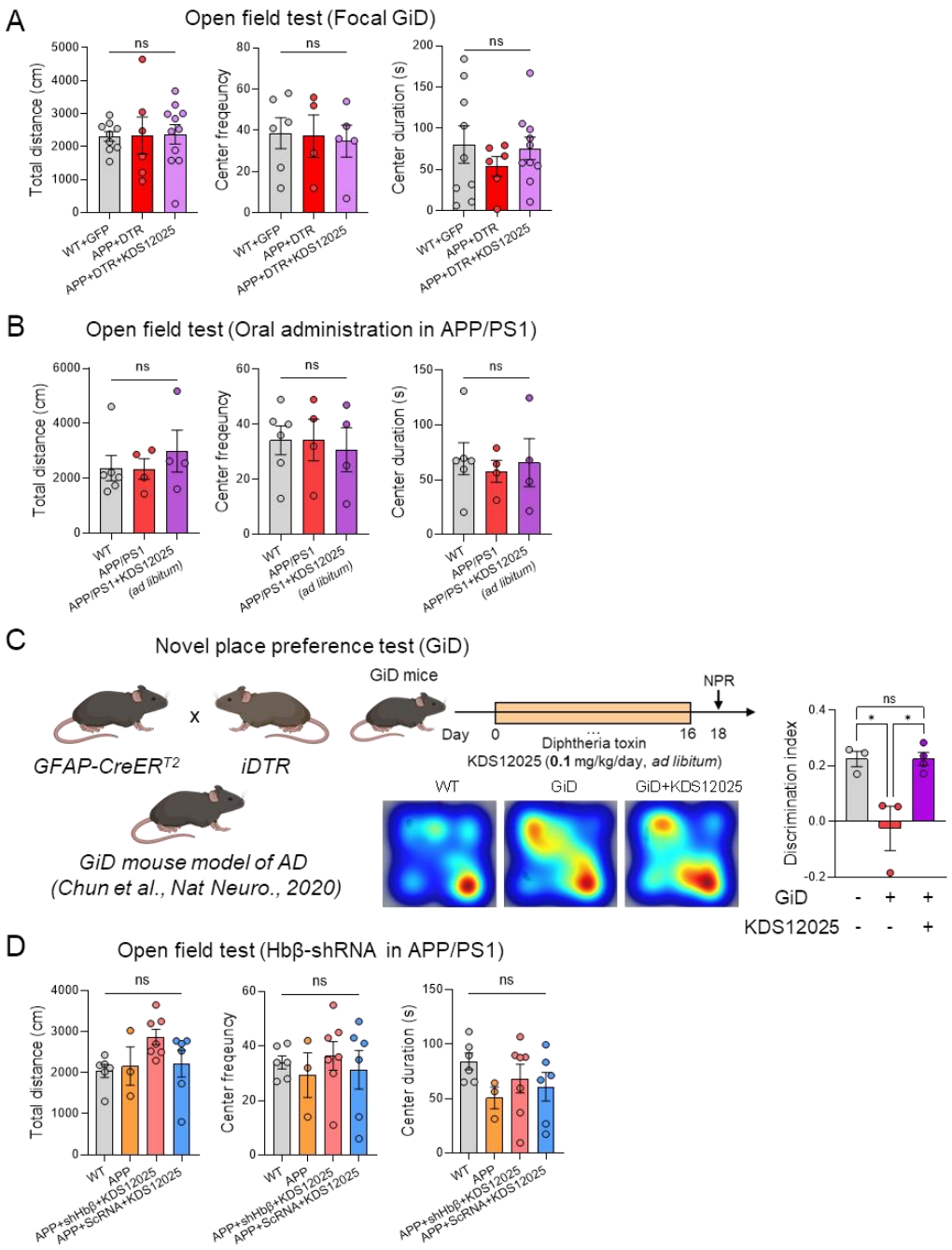

fig S10. General locomotor and memory performance test with KDS12025. (A) Open Field Test (OFT) measuring total distance, center frequency, and center duration for focal GiD groups with KDS12025 treatment. **(B)** OFT for APP/PS1 groups with KDS12025 (*ad libitum*) treatment. **(C)** *GFAP-CreERT2* and *iDTR* crossbred GiD mouse model (Chun et al., Nature Neuroscience, 2020; left) and results of NPR test following administration of KDS12025 (*ad libitum*, 0.1 mg/kg/day) to the GiD mouse model. **(D)** OFT for APP/PS1 of Hbβ silencing with shRNA with KDS12025 treatment. Data are presented as the mean ± s.e.m. *P < 0.05; ns, not significant. Additional statistics are provided in table S7.

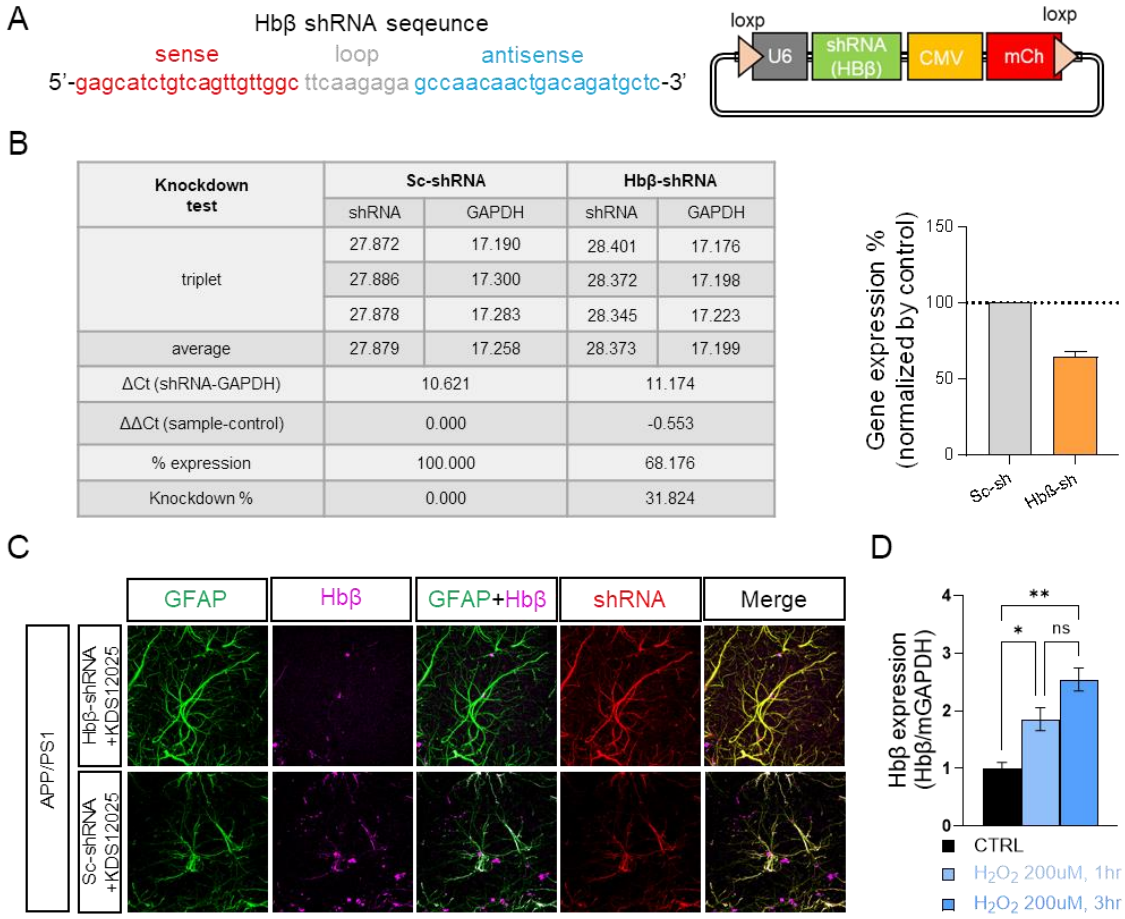

Knockdown test	Sc-shRNA		Hbβ-shRNA	
	shRNA	GAPDH	shRNA	GAPDH
triplet	27.872	17.190	28.401	17.176
	27.886	17.300	28.372	17.198
	27.878	17.283	28.345	17.223
average	27.879	17.258	28.373	17.199
ΔCt (shRNA-GAPDH)	10.621		11.174	
ΔΔCt (sample-control)	0.000		-0.553	
% expression	100.000		68.176	
Knockdown %	0.000		31.824	

fig. S11. Validation of Hbβ-shRNA and acute application of oxidative stress in cultured astrocytes. (A) The sequence and map of Hbβ-shRNA used in this study. **(B)** Validation of Hbβ-shRNA efficiency in cultured astrocytes via qRT-PCR, comparing the knockdown results with Sc-shRNA. **(C)** Lattice SIM imaging demonstrates Hbβ levels in astrocytes after treatment with control Sc-shRNA versus Hbβ-shRNA. **(D)** Quantitative RT-PCR measurement of Hbβ mRNA in cultured astrocytes exposed to 200 μM H_2O_2 for 1 hour and 3 hours. *P < 0.05, **P < 0.01; ns, not significant. Additional statistics are provided in table S7.

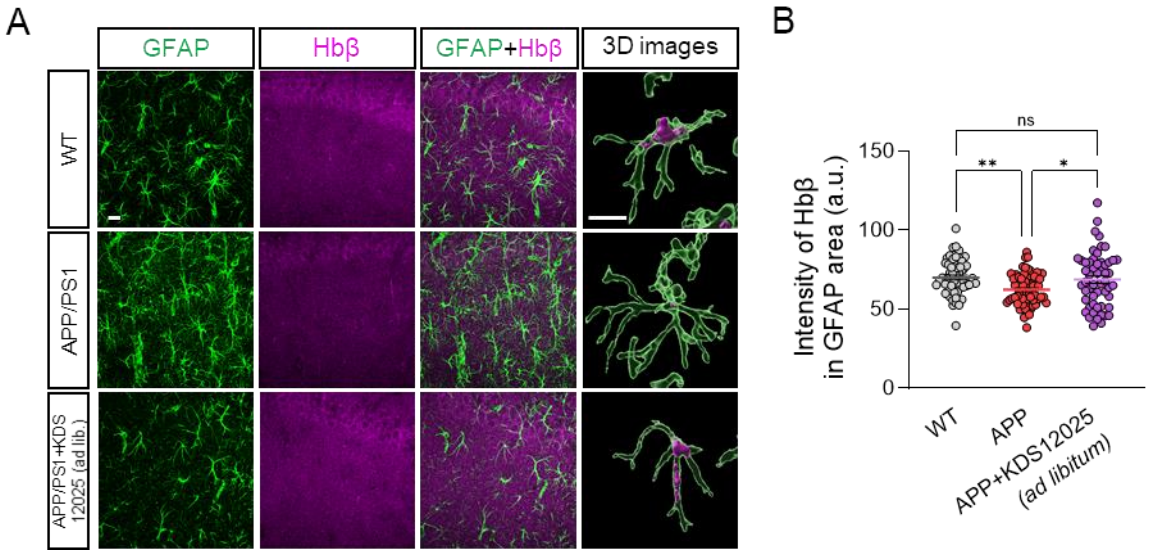

fig. S12. KDS12025-induced virtuous cycle of Hbβ in the hippocampus of APP/PS1 mice. (A) Representative confocal and 3D images of astrocytic Hbβ in WT, APP/PS1, and APP/PS1 mice treated with KDS12025. **(B)** Quantitative analysis of astrocytic Hbβ levels. Data are presented as the mean ± s.e.m. *P < 0.05, **P < 0.01; ns, not significant. Additional statistics are provided in table S7.

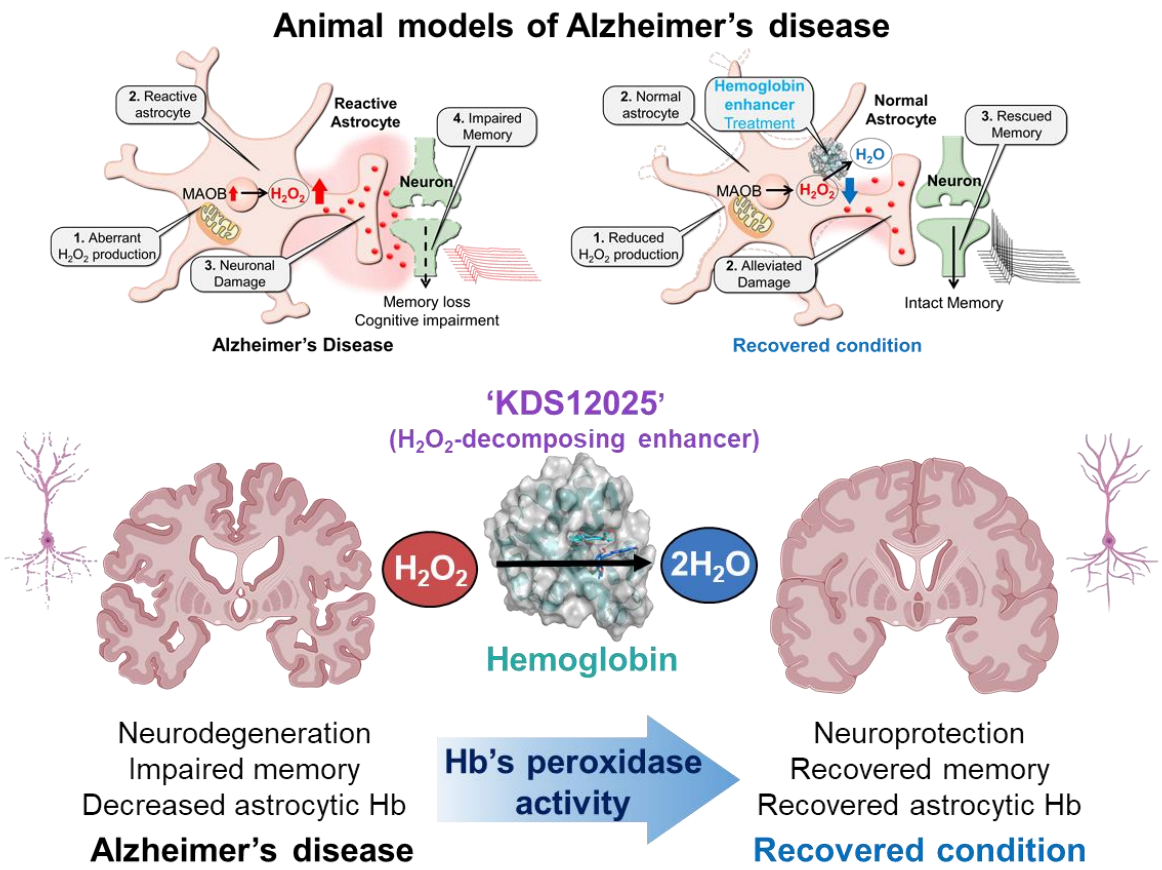

fig. S13. Graphical abstract and summaries.

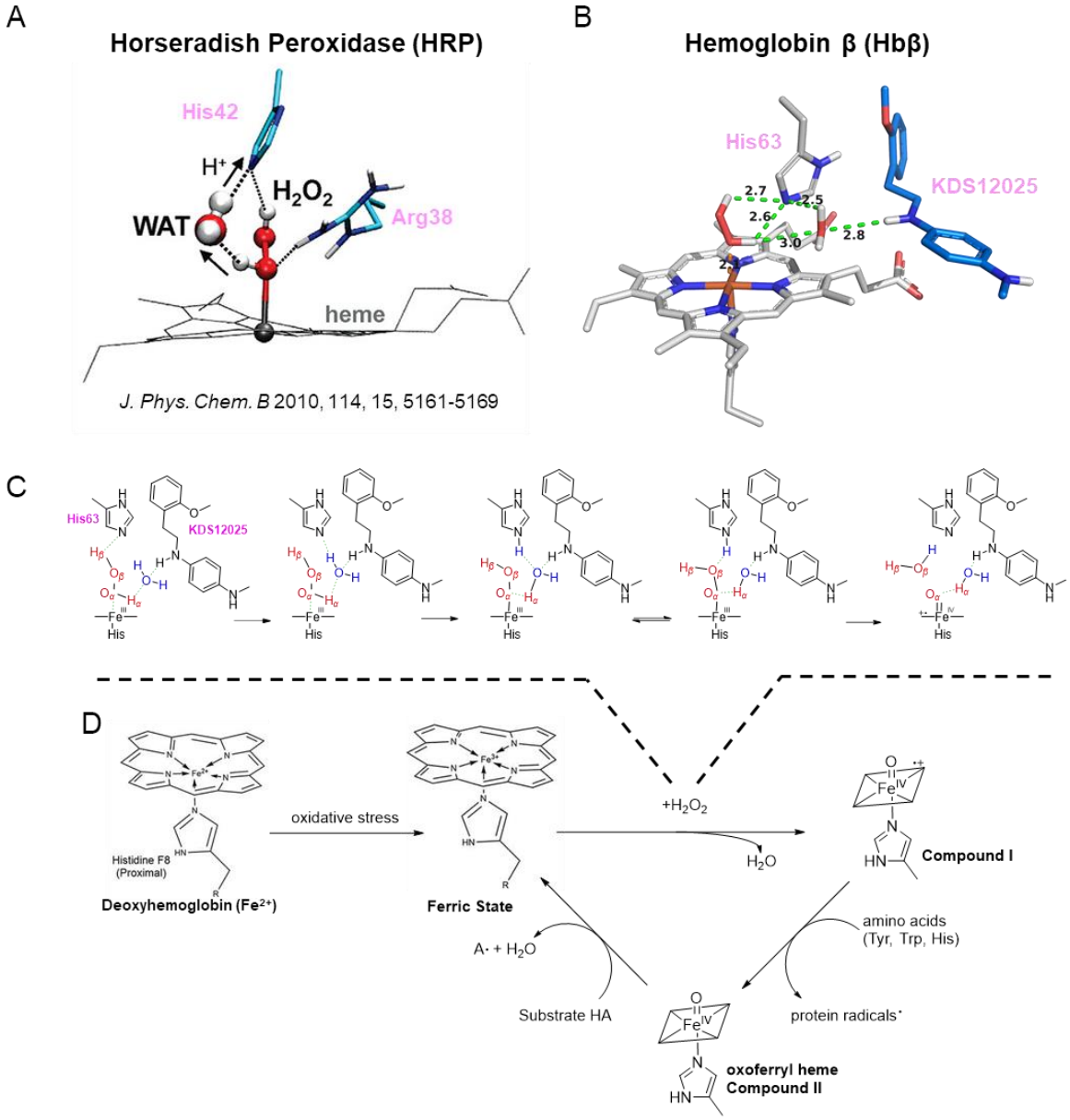

fig. S14. Mechanism of KDS12025 enhancement of hemoglobin peroxidase activity. (A) Representative snapshot of HRP and H_2O - H_2O_2 – His42 – Arg38 reactive conformation for H_2O_2 decomposition and subsequent activation to Por°±Fe^{IV}=O (taken from *J. Phys. Chem. B* 2010, 114, 14, 5161-5169). **(B)** Predicted reactive conformation of H_2O – H_2O_2 – His63 – KDS12025 for H_2O_2 composition and subsequent activation to Por°±Fe^{IV}=O (Compound I). **(C)** Proposed reactive conformation mechanism for the decomposition of H_2O_2 (red color) for proton transfer and release of H_2O (blue color) with KDS12025 assisting in coordinating H_2O and subsequently H_2O_2 with the iron atom. **(D)** General hemoglobin peroxidase cycle. KDS12025 facilitates the decomposition of H_2O_2 and the formation of Por°±Fe^{IV}=O (Compound I).

table S1. SAR analysis of HTPEB

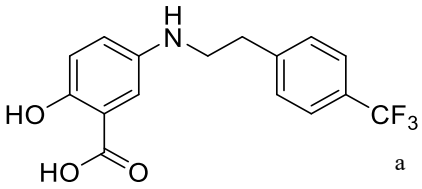

a

Cmpd.	Structure	HB-EC_{50}	HRP-EC_{50}
Salicylic Acid	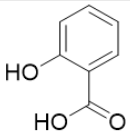	>10	>10
p-Cresotic acid	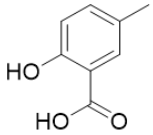	>10	>10
Mesalazine	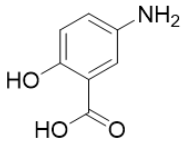	0.2129	3.604
2-(4-(Trifluoromethyl)phenyl)ethylamine	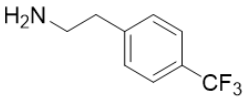	>10	>10

[a] Structure of HTPEB

table S2. Effects synthesized compounds on hydrogen peroxide scavenging activity.

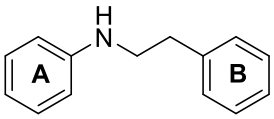

Cmpd.	A	B	HB-EC_{50}	HRP-EC_{50}
HTPEB	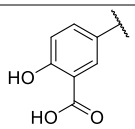	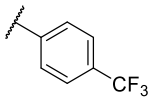	0.1551	1.520
7b	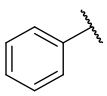	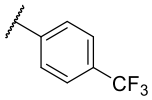	393.2	>10
7c	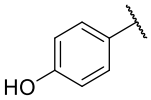	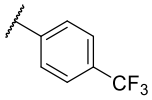	5.090	>10
7d	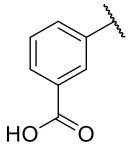	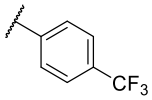	>10	>10
8a (KDS12017)	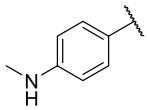	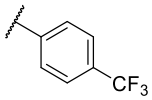	0.08622	0.8276
8b (KDS12008)	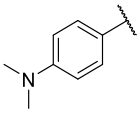	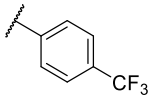	0.06704	0.7953
8c (KDS12025)	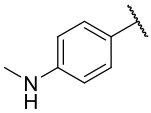	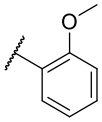	0.04489	0.5289
8d	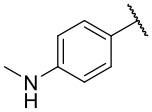	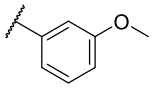	0.08551	0.5163
8e	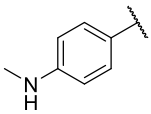	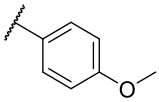	0.06946	0.7896
8f	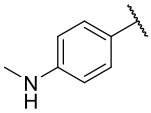	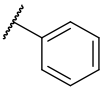	0.07806	0.8973
8g	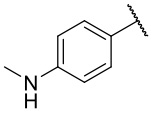	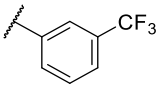	0.08838	0.3782
8h	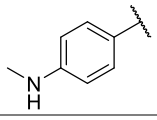	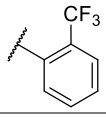	0.06911	0.4999

table S3. *In vivo* pharmacokinetic parameters of KDS12025

Cmpd.	PK[a]						
	i.v.				*p.o.*		*F* (%)
	AUC_{all} (ng*h/mL)	*Cl* (mL/h/kg)	V_{ss} (L/kg)	$t_{1/2}$ (h)	C_{max} (ng/mL)	AUC_{all} (ng*h/mL)	
KDS12025	686.60+118	74442.14+1493	5033.68+1407	0.96+0.09	2305.40+344	3601.96+662	87.43

[a]Mice (n=4) were dosed with 5 mg/kg for i.v. and 30 mg/kg for p.o.. Parameters were calculated from composite plasma concentration-time data. Data are expressed as the mean ± SD %.

Abbreviations: *Cmpd*, compound; *AUC*, area under the plasma concentration-time curve; *Cl*, time-averaged total body clearance; V_{ss}, apparent volume distribution at steady state; $t_{1/2}$, elimination half-life; C_{max}, maximum concentration of the drug; *F*, bioavailability

PAMPA[a] BBB permeability					
Compound	Concentration	Incubation Time	P_e (10^{-6}cm/sec)	BCS code[b]	Method
Progesterone	50 μM	4 hr	42.18	High (CNS+)	U.V
Ranitidine	50 μM	4 hr	0	Low (CNS-)	U.V
KDS12025	50 μM	4 hr	67.43	High (CNS+)	U.V
HTPEB	50 μM	4 hr	3.56	High (CNS-)	U.V

[a]PAMPA; parallel artificial membrane permeability assay.

[b]

Permeability classification		CNS +/- classification	
P_e (10^{-6}cm/sec)	**Classification**	**P_e (10^{-6}cm/sec)**	**Classification**
> 0.4	High	> 10	+
< 0.4	Low	< 10	-

1139 **table S4. KINOMEscan screening results for KDS12025 interactions with 97 kinases**

Compound Name	Selectivity Score Type	Number of Hits	Number of Non-Mutant Kinases	Screening Concentration (nM)	Selectivity Score
KDS12025	S(35)	0	90	1000	0
KDS12025	S(10)	0	90	1000	0
KDS12025	S(1)	0	90	1000	0

Compound Name	DiscoveRx Gene Symbol	Entrez Gene Symbol	Percent Control	Compound Concentration (nM)
KDS12025	ABL1(E255K)-phosphorylated	ABL1	88	1000
KDS12025	ABL1(T315I)-phosphorylated	ABL1	92	1000
KDS12025	ABL1-nonphosphorylated	ABL1	69	1000
KDS12025	ABL1-phosphorylated	ABL1	75	1000
KDS12025	ACVR1B	ACVR1B	95	1000
KDS12025	ADCK3	CABC1	100	1000
KDS12025	AKT1	AKT1	100	1000
KDS12025	AKT2	AKT2	89	1000
KDS12025	ALK	ALK	84	1000
KDS12025	AURKA	AURKA	90	1000
KDS12025	AURKB	AURKB	83	1000
KDS12025	AXL	AXL	71	1000
KDS12025	BMPR2	BMPR2	97	1000
KDS12025	BRAF	BRAF	89	1000
KDS12025	BRAF(V600E)	BRAF	72	1000
KDS12025	BTK	BTK	98	1000
KDS12025	CDK11	CDK19	100	1000
KDS12025	CDK2	CDK2	100	1000
KDS12025	CDK3	CDK3	83	1000
KDS12025	CDK7	CDK7	94	1000
KDS12025	CDK9	CDK9	93	1000
KDS12025	CHEK1	CHEK1	88	1000
KDS12025	CSF1R	CSF1R	100	1000
KDS12025	CSNK1D	CSNK1D	84	1000
KDS12025	CSNK1G2	CSNK1G2	69	1000
KDS12025	DCAMKL1	DCLK1	100	1000
KDS12025	DYRK1B	DYRK1B	69	1000
KDS12025	EGFR	EGFR	92	1000
KDS12025	EGFR(L858R)	EGFR	91	1000
KDS12025	EPHA2	EPHA2	100	1000
KDS12025	ERBB2	ERBB2	99	1000
KDS12025	ERBB4	ERBB4	88	1000
KDS12025	ERK1	MAPK3	88	1000
KDS12025	FAK	PTK2	94	1000
KDS12025	FGFR2	FGFR2	100	1000
KDS12025	FGFR3	FGFR3	99	1000
KDS12025	FLT3	FLT3	75	1000
KDS12025	GSK3B	GSK3B	89	1000
KDS12025	IGF1R	IGF1R	86	1000
KDS12025	IKK-alpha	CHUK	78	1000
KDS12025	IKK-beta	IKBKB	94	1000
KDS12025	INSR	INSR	87	1000
KDS12025	JAK2(JH1domain-catalytic)	JAK2	84	1000
KDS12025	JAK3(JH1domain-catalytic)	JAK3	96	1000
KDS12025	JNK1	MAPK8	90	1000
KDS12025	JNK2	MAPK9	100	1000
KDS12025	JNK3	MAPK10	92	1000
KDS12025	KIT	KIT	97	1000
KDS12025	KIT(D816V)	KIT	100	1000
KDS12025	KIT(V559D,T670I)	KIT	100	1000
KDS12025	LKB1	STK11	75	1000
KDS12025	MAP3K4	MAP3K4	96	1000
KDS12025	MAPKAPK2	MAPKAPK2	72	1000
KDS12025	MARK3	MARK3	100	1000
KDS12025	MEK1	MAP2K1	61	1000
KDS12025	MEK2	MAP2K2	55	1000
KDS12025	MET	MET	85	1000
KDS12025	MKNK1	MKNK1	79	1000
KDS12025	MKNK2	MKNK2	100	1000
KDS12025	MLK1	MAP3K9	100	1000
KDS12025	p38-alpha	MAPK14	100	1000
KDS12025	p38-beta	MAPK11	100	1000
KDS12025	PAK1	PAK1	100	1000
KDS12025	PAK2	PAK2	76	1000
KDS12025	PAK4	PAK4	100	1000
KDS12025	PCTK1	CDK16	73	1000
KDS12025	PDGFRA	PDGFRA	95	1000
KDS12025	PDGFRB	PDGFRB	100	1000
KDS12025	PDPK1	PDPK1	82	1000
KDS12025	PIK3C2B	PIK3C2B	56	1000
KDS12025	PIK3CA	PIK3CA	70	1000
KDS12025	PIK3CG	PIK3CG	81	1000
KDS12025	PIM1	PIM1	100	1000
KDS12025	PIM2	PIM2	96	1000
KDS12025	PIM3	PIM3	100	1000
KDS12025	PKAC-alpha	PRKACA	100	1000
KDS12025	PLK1	PLK1	87	1000
KDS12025	PLK3	PLK3	84	1000
KDS12025	PLK4	PLK4	83	1000
KDS12025	PRKCE	PRKCE	98	1000
KDS12025	RAF1	RAF1	100	1000
KDS12025	RET	RET	79	1000
KDS12025	RIOK2	RIOK2	67	1000
KDS12025	ROCK2	ROCK2	99	1000
KDS12025	RSK2(Kin.Dom.1-N-terminal)	RPS6KA3	63	1000
KDS12025	SNARK	NUAK2	90	1000
KDS12025	SRC	SRC	100	1000
KDS12025	SRPK3	SRPK3	100	1000
KDS12025	TGFBR1	TGFBR1	93	1000
KDS12025	TIE2	TEK	95	1000
KDS12025	TRKA	NTRK1	85	1000
KDS12025	TSSK1B	TSSK1B	61	1000
KDS12025	TYK2(JH1domain-catalytic)	TYK2	86	1000
KDS12025	ULK2	ULK2	87	1000
KDS12025	VEGFR2	KDR	82	1000
KDS12025	YANK3	STK32C	84	1000
KDS12025	ZAP70	ZAP70	78	1000

1140

table S5. KDS12025 interactions with 87 primary molecular targets including G protein–coupled receptors (GPCRs), kinases, non-kinase enzymes, nuclear receptors, transporters, and various ion channels

Compound I.D.	Client Compound I.D.	Test Concentration	% Inhibition of Control Specific Binding 1st	2nd	Mean
A_{2A}*(h)* (agonist radioligand)					
100059830-2	KDS12025	1.0E-06 M	9.7	8.8	9.3
α_{1A}*(h)* (antagonist radioligand)					
100059830-2	KDS12025	1.0E-06 M	12.4	13.5	12.9
α_{1B}*(h)* (antagonist radioligand)					
100059830-2	KDS12025	1.0E-06 M	38.6	30.6	34.6
α_{1D}*(h)* (antagonist radioligand)					
100059830-2	KDS12025	1.0E-06 M	24.7	23.7	24.2
α_{2A}*(h)* (antagonist radioligand)					
100059830-2	KDS12025	1.0E-06 M	13.1	14.6	13.9
α_{2B}*(h)* (antagonist radioligand)					
100059830-2	KDS12025	1.0E-06 M	18.1	13.4	15.8
β_1*(h)* (agonist radioligand)					
100059830-2	KDS12025	1.0E-06 M	13.3	5.7	9.5
β_2*(h)* (antagonist radioligand)					
100059830-2	KDS12025	1.0E-06 M	3.2	-3.9	-0.3
AT_1 *(h)* (antagonist radioligand)					
100059830-2	KDS12025	1.0E-06 M	17.7	7.5	12.6
BZD (central) (agonist radioligand)					
100059830-2	KDS12025	1.0E-06 M	-2.5	3.4	0.5
Cl- channel (GABA-gated) (TBOB site) (antagonist radioligand)					
100059830-2	KDS12025	1.0E-06 M	-3.8	11.0	3.6
B_2 *(h)* (agonist radioligand)					
100059830-2	KDS12025	1.0E-06 M	-4.5	0.6	-2.0
CB_1*(h)* (agonist radioligand)					
100059830-2	KDS12025	1.0E-06 M	18.3	21.6	20.0
CB_2*(h)* (agonist radioligand)					
100059830-2	KDS12025	1.0E-06 M	21.6	9.2	15.4
CCK_1 (CCK_A) *(h)* (agonist radioligand)					
100059830-2	KDS12025	1.0E-06 M	-3.7	-4.5	-4.1
CCK_2 (CCK_B) *(h)* (agonist radioligand)					
100059830-2	KDS12025	1.0E-06 M	-7.1	3.0	-2.1
D_1*(h)* (antagonist radioligand)					
100059830-2	KDS12025	1.0E-06 M	8.9	-3.8	2.5
D_{2S}*(h)* (agonist radioligand)					
100059830-2	KDS12025	1.0E-06 M	36.0	40.2	38.1
D_{2L}*(h)* (antagonist radioligand)					
100059830-2	KDS12025	1.0E-06 M	25.2	6.8	16.0
ET_A*(h)* (agonist radioligand)					
100059830-2	KDS12025	1.0E-06 M	-8.0	9.2	0.6
$GABA_{A1}$ *(h)* (α1,β2,γ2) (agonist radioligand)					
100059830-2	KDS12025	1.0E-06 M	7.6	2.2	4.9
$GABA_{B(1b)}$*(h)* (antagonist radioligand)					
100059830-2	KDS12025	1.0E-06 M	-6.5	-0.7	-3.6
AMPA (agonist radioligand)					
100059830-2	KDS12025	1.0E-06 M	2.0	-2.8	-0.4
kainate (agonist radioligand)					
100059830-2	KDS12025	1.0E-06 M	23.2	-18.1	2.6
NMDA (antagonist radioligand)					
100059830-2	KDS12025	1.0E-06 M	2.2	0.4	1.3
mGluR5 (h) (agonist radioligand)					
100059830-2	KDS12025	1.0E-06 M	-13.6	-15.8	-14.7

Compound I.D.	Client Compound I.D.	Test Concentration	% Inhibition of Control Specific Binding 1st	2nd	Mean
glycine (strychnine-sensitive) (antagonist radioligand)					
100059830-2	KDS12025	1.0E-06 M	-17.4	-17.6	-17.5
glycine (strychnine-insensitive) (antagonist radioligand)					
100059830-2	KDS12025	1.0E-06 M	3.2	-0.5	1.4
CXCR2 (IL-8B) *(h)* (agonist radioligand)					
100059830-2	KDS12025	1.0E-06 M	8.2	16.7	12.4
CCR1 *(h)* (agonist radioligand)					
100059830-2	KDS12025	1.0E-06 M	9.6	11.8	10.7
H_1*(h)* (antagonist radioligand)					
100059830-2	KDS12025	1.0E-06 M	12.9	10.6	11.8
H_2*(h)* (antagonist radioligand)					
100059830-2	KDS12025	1.0E-06 M	-12.8	5.8	-3.5
$CysLT_1$ (LTD_4)*(h)* (agonist radioligand)					
100059830-2	KDS12025	1.0E-06 M	16.9	9.0	12.9
MC_1 (agonist radioligand)					
100059830-2	KDS12025	1.0E-06 M	-16.6	-1.8	-9.2
MC_4*(h)* (agonist radioligand)					
100059830-2	KDS12025	1.0E-06 M	11.3	14.5	12.9
MAO-A (antagonist radioligand)					
100059830-2	KDS12025	1.0E-06 M	4.5	-5.1	-0.3
M_1*(h)* (antagonist radioligand)					
100059830-2	KDS12025	1.0E-06 M	2.2	14.1	8.2
M_2 *(h)* (antagonist radioligand)					
100059830-2	KDS12025	1.0E-06 M	-4.1	-10.2	-7.1
M_3*(h)* (antagonist radioligand)					
100059830-2	KDS12025	1.0E-06 M	11.8	17.3	14.5
M_4*(h)* (antagonist radioligand)					
100059830-2	KDS12025	1.0E-06 M	1.0	-4.5	-1.7
NK_1*(h)* (agonist radioligand)					
100059830-2	KDS12025	1.0E-06 M	7.8	9.9	8.8
Y_1*(h)* (agonist radioligand)					
100059830-2	KDS12025	1.0E-06 M	-5.5	-2.1	-3.8
N neuronal α4β2 *(h)* (agonist radioligand)					
100059830-2	KDS12025	1.0E-06 M	1.5	1.7	1.6
N muscle-type *(h)* (antagonist radioligand)					
100059830-2	KDS12025	1.0E-06 M	31.5	20.0	25.7
δ (DOP) *(h)* (agonist radioligand)					
100059830-2	KDS12025	1.0E-06 M	10.6	30.0	20.3
kappa *(h)* (KOP) (agonist radioligand)					
100059830-2	KDS12025	1.0E-06 M	22.1	12.4	17.3
μ (MOP) *(h)* (agonist radioligand)					
100059830-2	KDS12025	1.0E-06 M	14.5	16.5	15.5
PPARγ *(h)* (agonist radioligand)					
100059830-2	KDS12025	1.0E-06 M	5.3	-4.6	0.3
PAF *(h)* (agonist radioligand)					
100059830-2	KDS12025	1.0E-06 M	-6.0	-6.1	-6.0
PCP (antagonist radioligand)					
100059830-2	KDS12025	1.0E-06 M	5.4	10.6	8.0
RARα *(h)* (agonist radioligand)					
100059830-2	KDS12025	1.0E-06 M	-5.4	-5.0	-5.2
5-HT_{1A}*(h)* (agonist radioligand)					
100059830-2	KDS12025	1.0E-06 M	34.9	40.4	37.6

Compound I.D.	Client Compound I.D.	Test Concentration	% Inhibition of Control Specific Binding 1st	2nd	Mean
5-HT_{1B} *(h)* (antagonist radioligand)					
100059830-2	KDS12025	1.0E-06 M	13.2	5.3	9.2
5-HT_{2A}*(h)* (agonist radioligand)					
100059830-2	KDS12025	1.0E-06 M	22.5	13.9	18.2
5-HT_{2B}*(h)* (agonist radioligand)					
100059830-2	KDS12025	1.0E-06 M	34.1	38.2	36.1
5-HT_{2C}*(h)* (antagonist radioligand)					
100059830-2	KDS12025	1.0E-06 M	21.0	26.2	23.6
5-HT_3*(h)* (antagonist radioligand)					
100059830-2	KDS12025	1.0E-06 M	8.6	-0.5	4.0
GR *(h)* (agonist radioligand)					
100059830-2	KDS12025	1.0E-06 M	-4.3	-3.4	-3.9
Estrogen ER alpha (h) (agonist radioligand)					
100059830-2	KDS12025	1.0E-06 M	-9.2	18.5	4.7
PR *(h)* (agonist radioligand)					
100059830-2	KDS12025	1.0E-06 M	-5.3	-2.8	-4.1
AR(h) (agonist radioligand)					
100059830-2	KDS12025	1.0E-06 M	5.8	12.5	9.1
V_{1a}*(h)* (agonist radioligand)					
100059830-2	KDS12025	1.0E-06 M	-12.5	-7.3	-9.9
Ca^{2+} channel (L, dihydropyridine site) (antagonist radioligand)					
100059830-2	KDS12025	1.0E-06 M	-37.5	-21.0	-29.3
Ca^{2+} channel (L, diltiazem site) (benzothiazepines) (antagonist radioligand)					
100059830-2	KDS12025	1.0E-06 M	11.9	18.3	15.1
Ca^{2+} channel (L, verapamil site) (phenylalkylamine) (antagonist radioligand)					
100059830-2	KDS12025	1.0E-06 M	-0.6	4.5	2.0
Ca^{2+} channel (N) (antagonist radioligand)					
100059830-2	KDS12025	1.0E-06 M	-3.6	-17.7	-10.7
Potassium Channel hERG (human)- [3H] Dofetilide					
100059830-2	KDS12025	1.0E-06 M	29.7	33.2	31.5
K_V channel (antagonist radioligand)					
100059830-2	KDS12025	1.0E-06 M	14.7	-7.8	3.5
Na^+ channel (site 2) (antagonist radioligand)					
100059830-2	KDS12025	1.0E-06 M	16.4	34.5	25.5
adenosine transporter (antagonist radioligand)					
100059830-2	KDS12025	1.0E-06 M	1.4	-1.4	0.0
norepinephrine transporter*(h)* (antagonist radioligand)					
100059830-2	KDS12025	1.0E-06 M	10.5	3.0	6.7
dopamine transporter*(h)* (antagonist radioligand)					
100059830-2	KDS12025	1.0E-06 M	-1.9	-11.4	-6.6
GABA transporter (antagonist radioligand)					
100059830-2	KDS12025	1.0E-06 M	-1.0	8.9	4.0
5-HT transporter *(h)* (antagonist radioligand)					
100059830-2	KDS12025	1.0E-06 M	37.1	53.6	45.4

table S6. Demographic information about human postmortem brain samples from normal subjects and AD patients.

Number	Case	Age	Sex	Braak Stage
1	Normal	88	M	I
2	Normal	82	M	I
3	Normal	70	M	I
1	AD	89	M	V
2	AD	83	M	VI
3	AD	70	M	VI

data S1

^{1}H and ^{13}C-NMR spectra

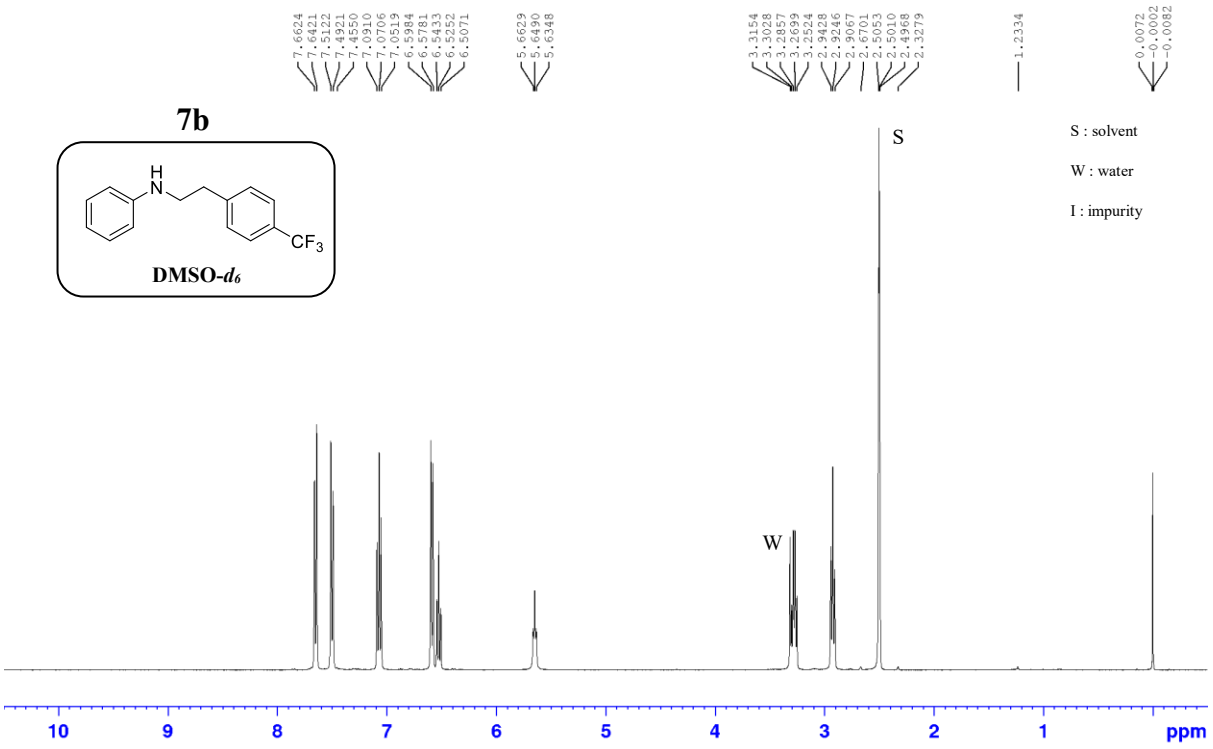

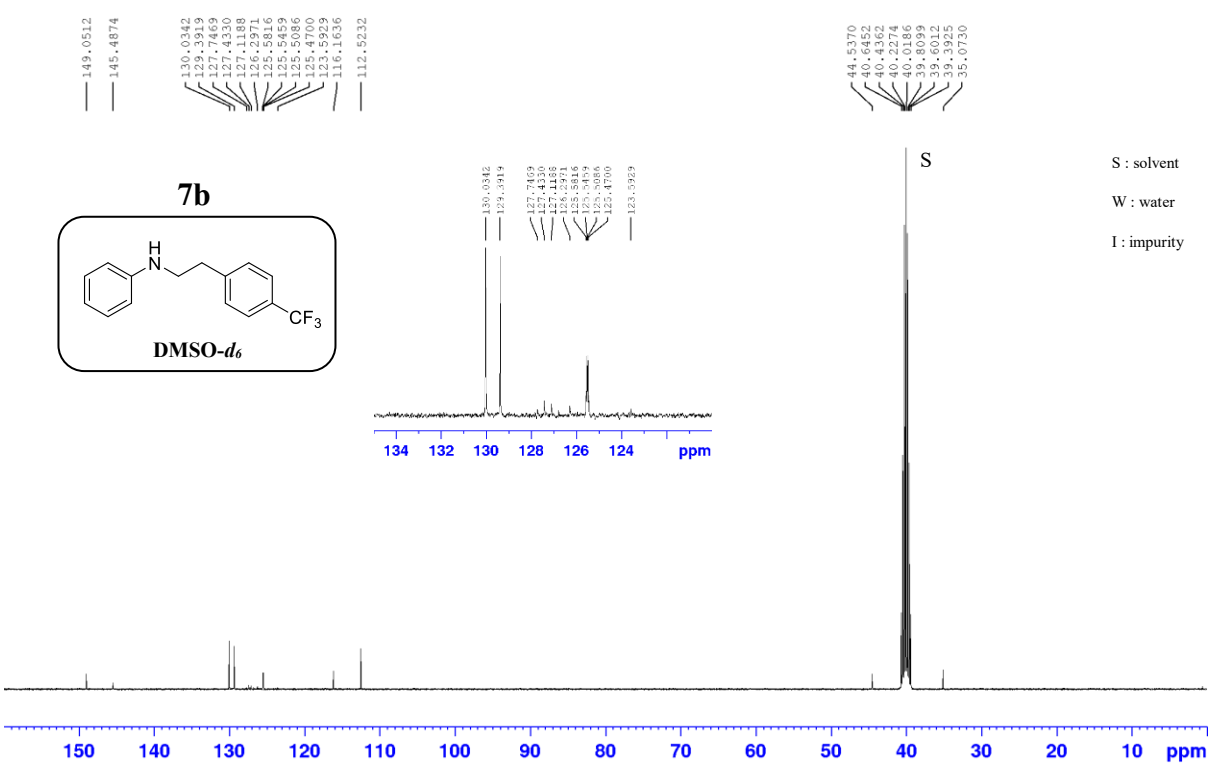

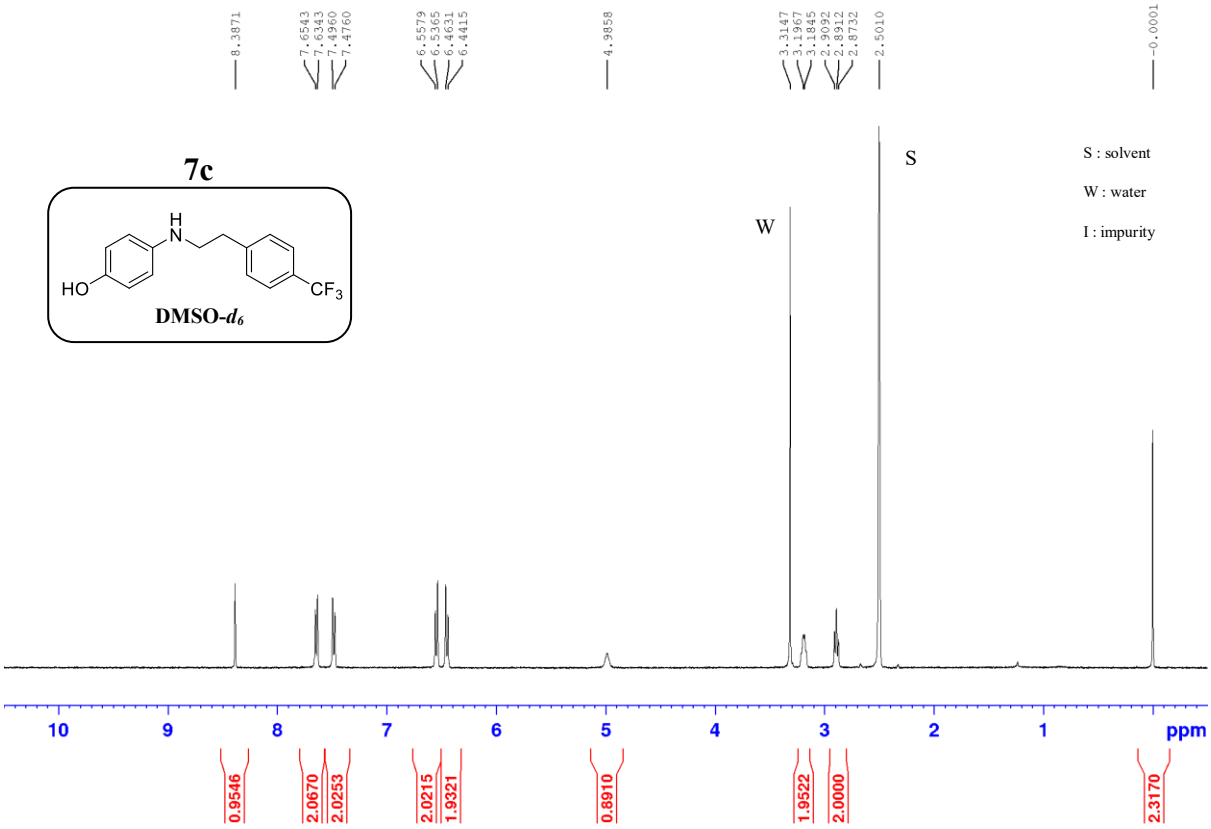
7c
HO
H
N
CF3
DMSO-d6
S : solvent
W : water
I : impurity
W
S
8.3871
7.6543
7.6343
7.4960
7.4760
6.5579
6.5365
6.4631
6.4415
4.9858
3.3147
3.1967
3.1845
2.9092
2.8912
2.8732
2.5010
-0.0001
0.9546
2.0670
2.0253
2.0215
1.9321
0.8910
1.9522
2.0000
2.3170
10 9 8 7 6 5 4 3 2 1 ppm

1156

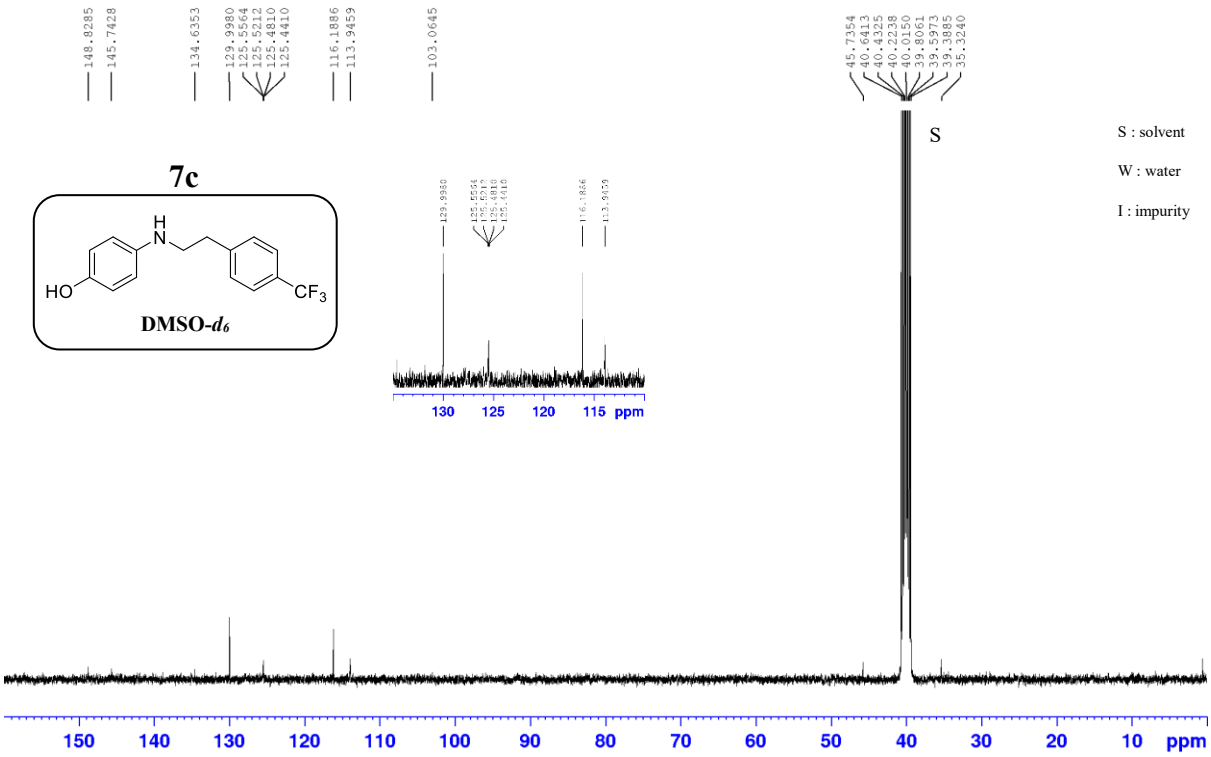
7c
HO
H
N
CF3
DMSO-d6
S : solvent
W : water
I : impurity
S
148.8285
145.7428
134.6353
129.9980
125.5564
125.5212
125.4810
125.4410
116.1886
113.9459
103.0645
45.7354
40.6413
40.4325
40.2238
40.0150
39.8061
39.5973
39.3885
35.3240
130 125 120 115 ppm
150 140 130 120 110 100 90 80 70 60 50 40 30 20 10 ppm

1157

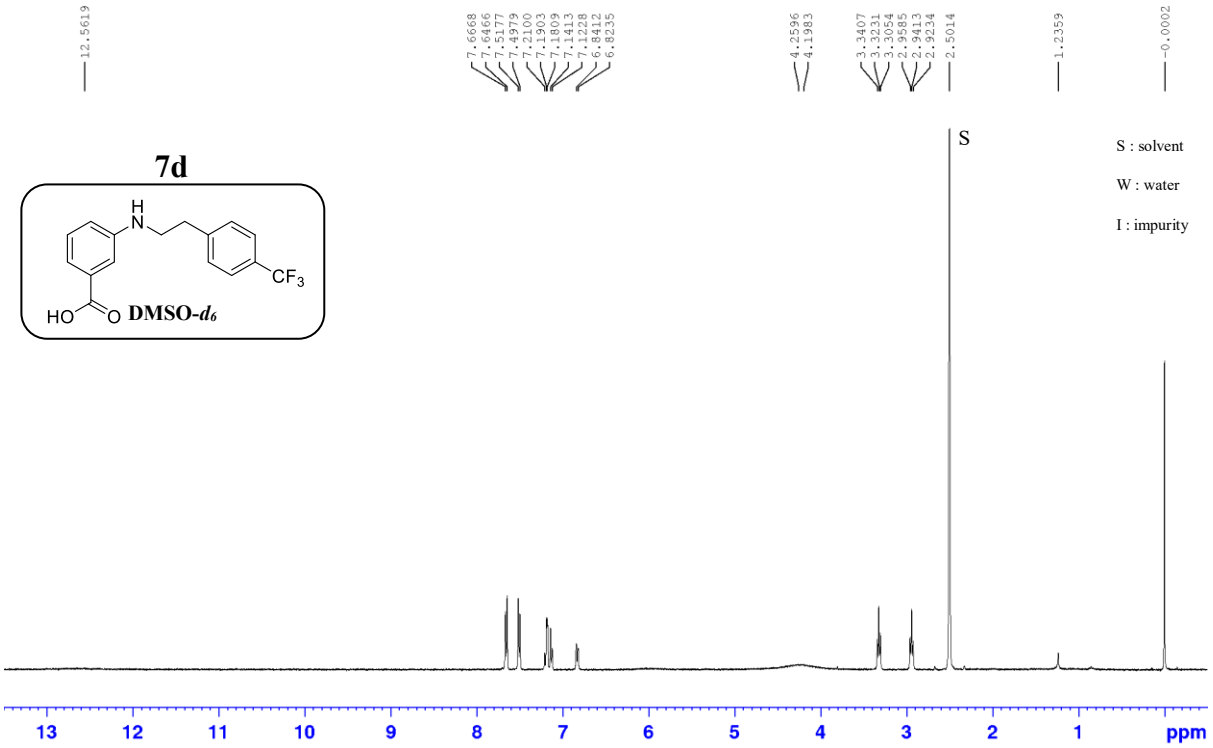

1158

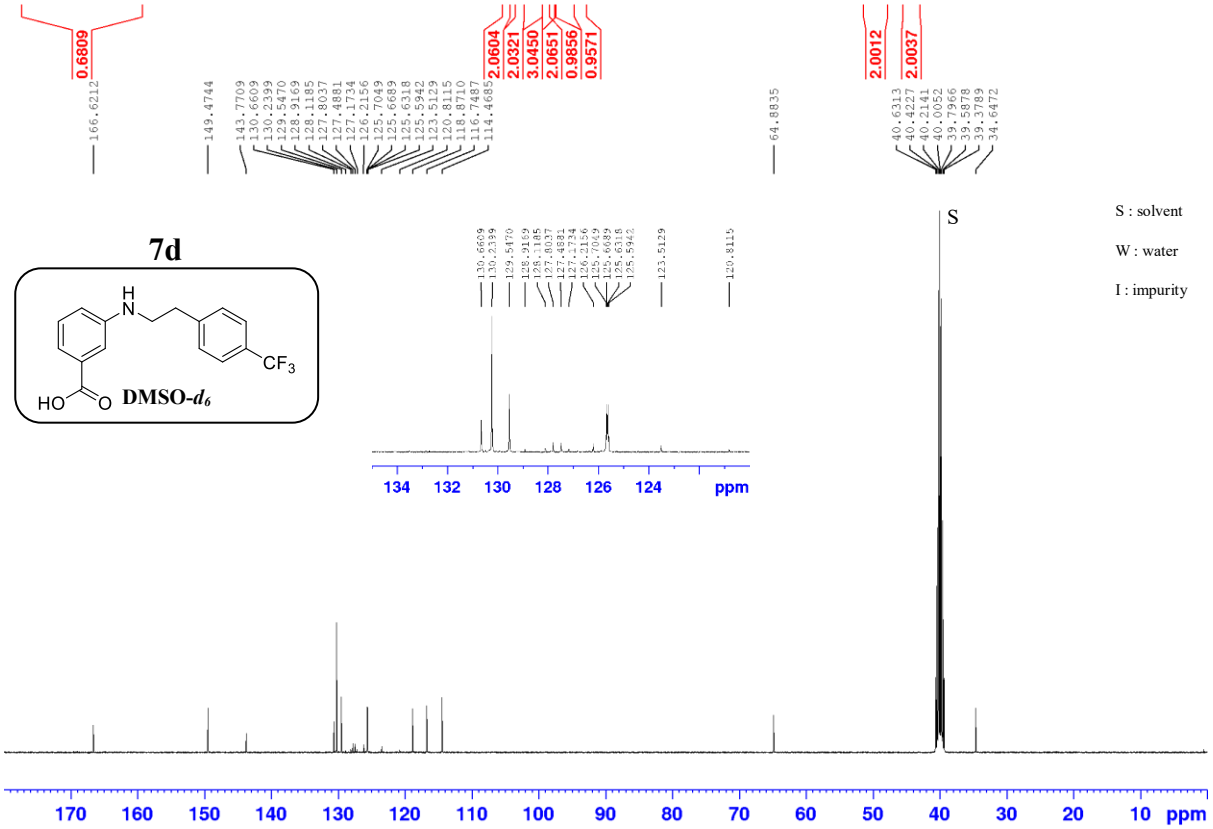

1159

1160

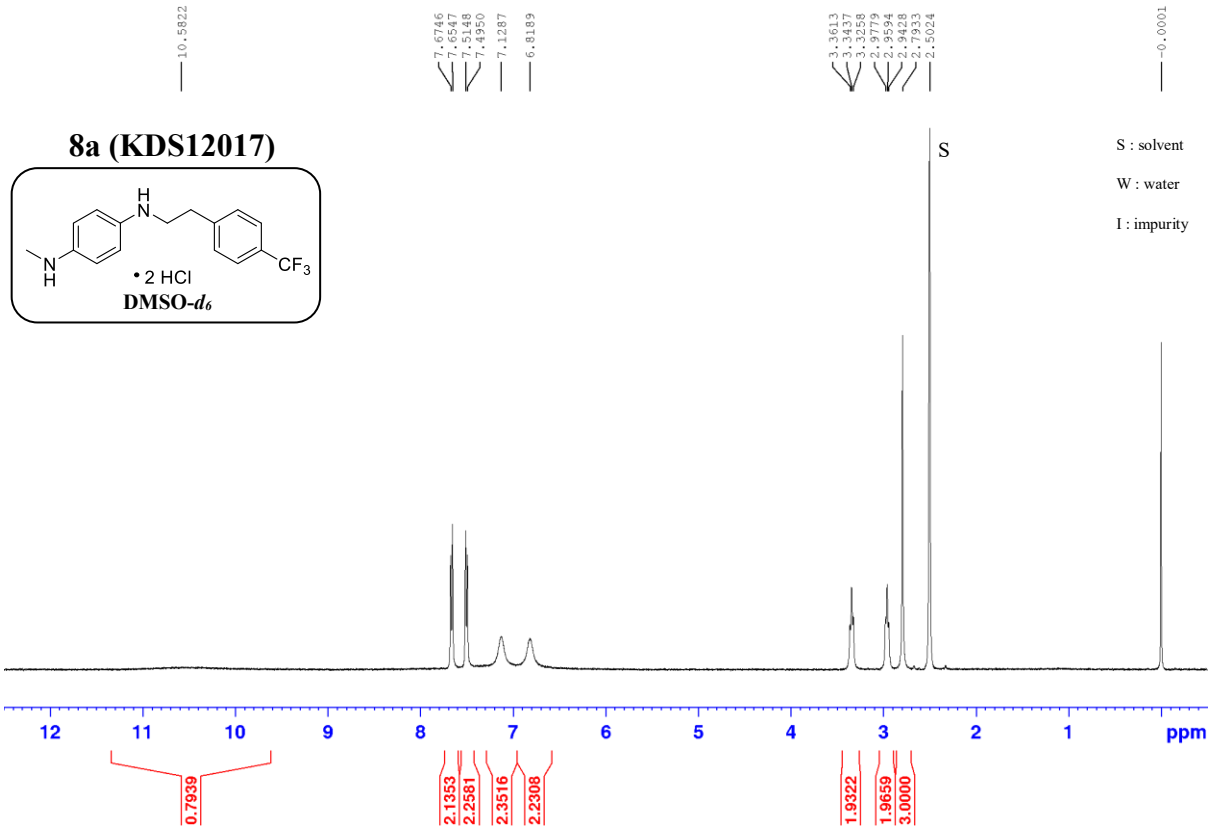
8a (KDS12017)
• 2 HCl
DMSO-d6
S : solvent
W : water
I : impurity
ppm

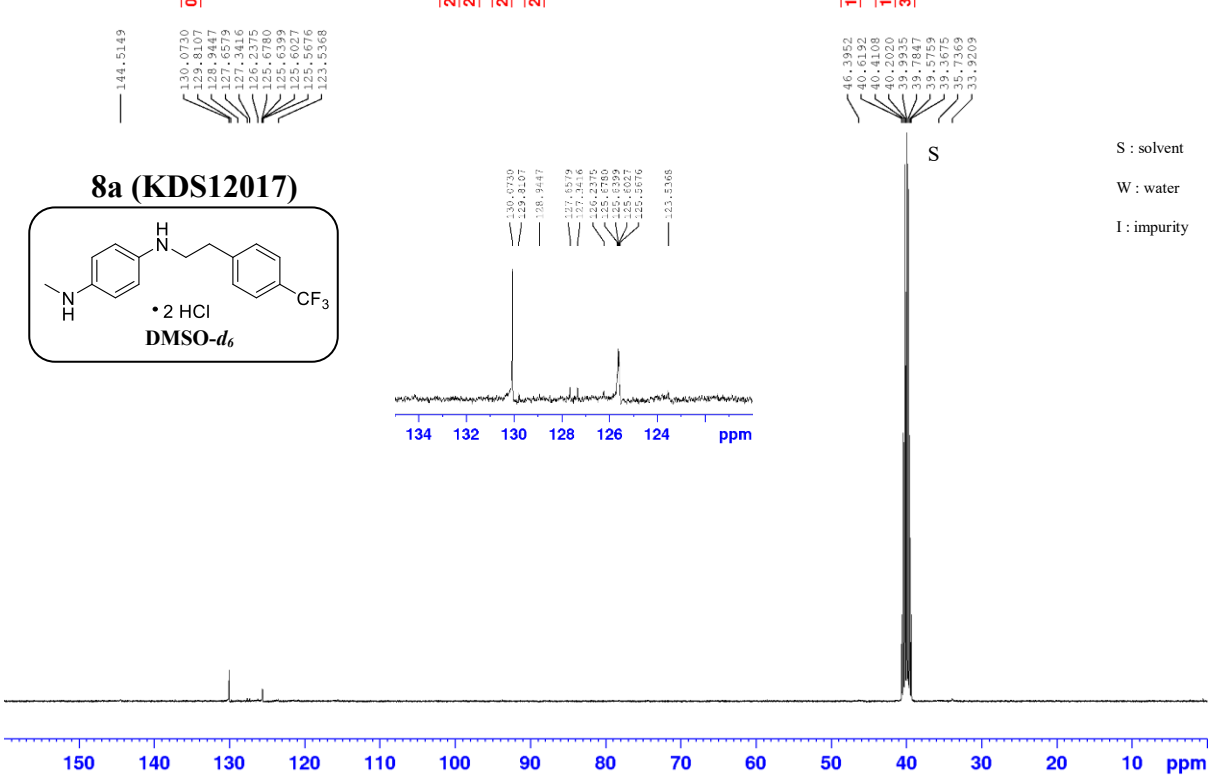
8a (KDS12017)
• 2 HCl
DMSO-d6
S : solvent
W : water
I : impurity
ppm

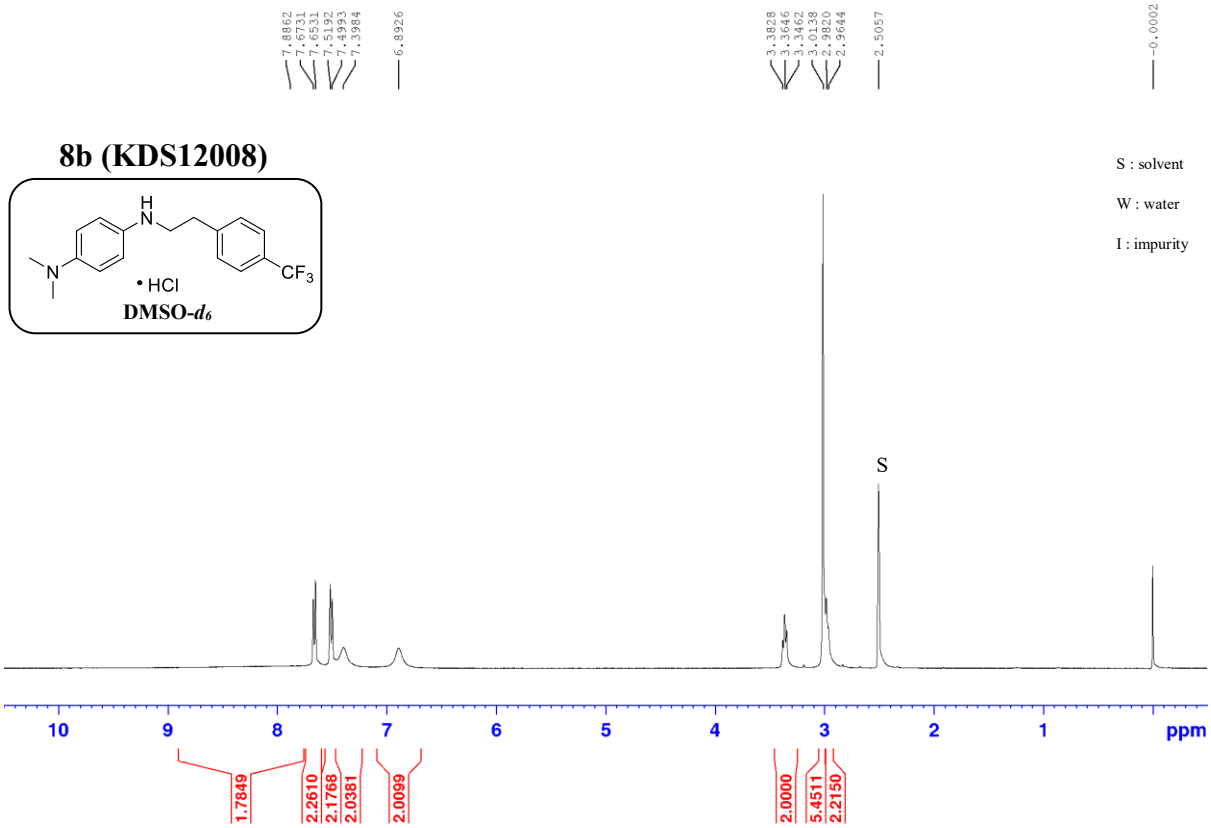

1164

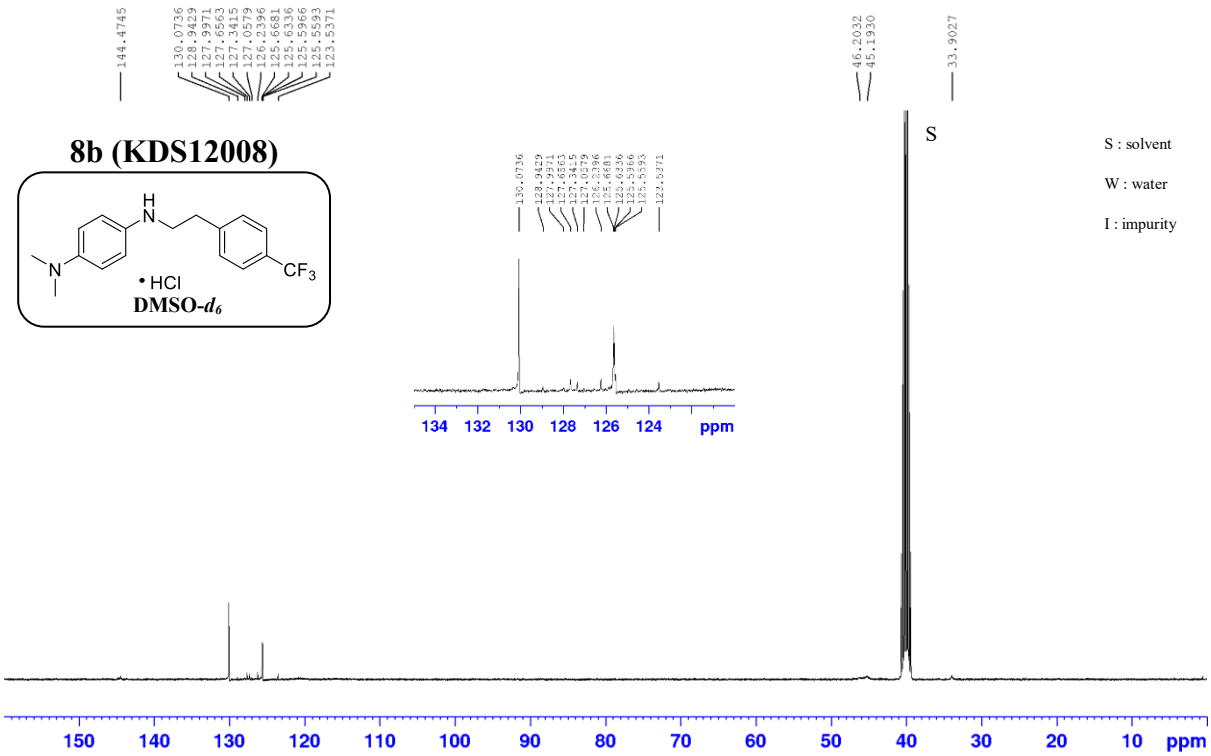

1165

1166

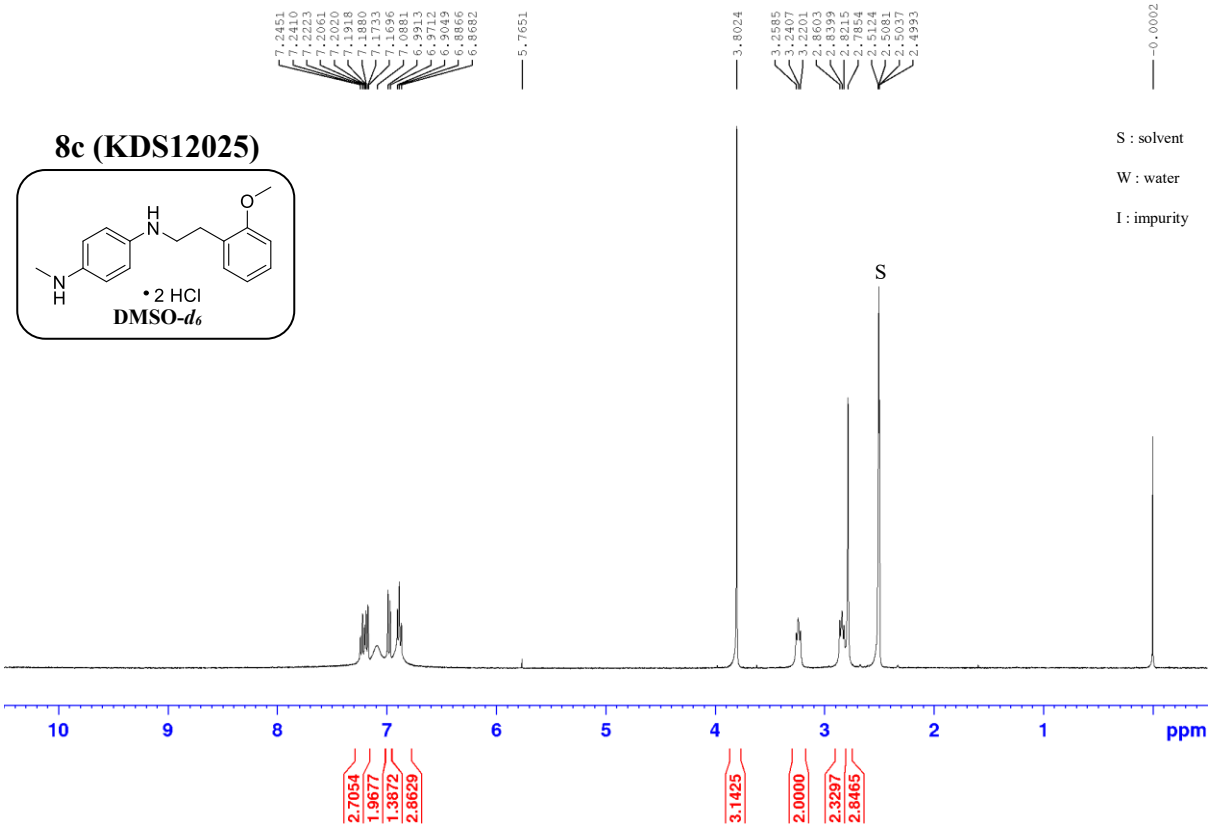
8c (KDS12025)
• 2 HCl
DMSO-d6
S : solvent
W : water
I : impurity
S
7.2451
7.2410
7.2223
7.2061
7.2020
7.1918
7.1880
7.1733
7.1696
7.0881
6.9913
6.9712
6.9049
6.8866
6.8682
5.7651
3.8024
3.2585
3.2407
3.2201
2.8603
2.8399
2.8215
2.7854
2.5124
2.5081
2.5037
2.4993
-0.0002
10 9 8 7 6 5 4 3 2 1 ppm
2.7054
1.9677
1.3872
2.8629
3.1425
2.0000
2.3297
2.8465

1167

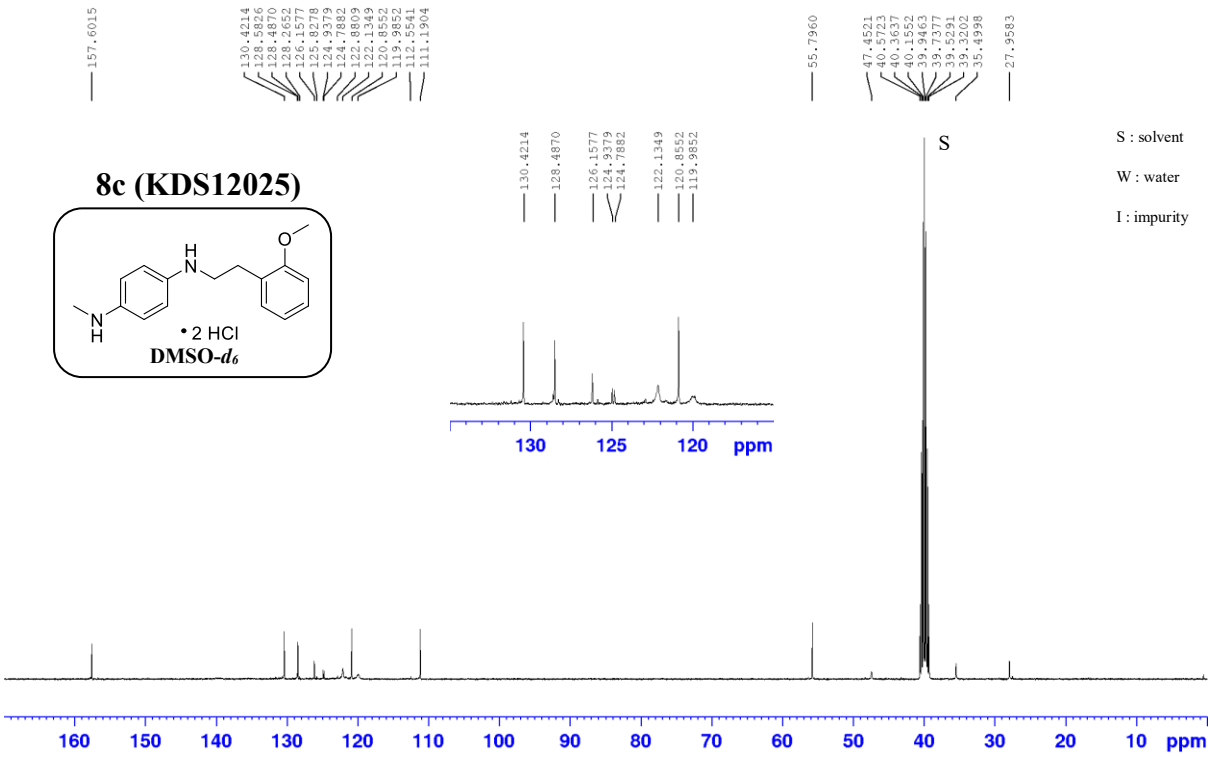
8c (KDS12025)
• 2 HCl
DMSO-d6
S : solvent
W : water
I : impurity
S
157.6015
130.4214
128.5826
128.4870
128.2652
126.1577
125.8278
124.9379
124.7882
122.8809
122.1349
120.8552
119.9852
112.5541
111.1904
55.7960
47.4521
40.5723
40.3637
40.1552
39.9463
39.7377
39.5291
39.3202
35.4998
27.9583
130.4214
128.4870
126.1577
124.9379
124.7882
122.1349
120.8552
119.9852
130 125 120 ppm
160 150 140 130 120 110 100 90 80 70 60 50 40 30 20 10 ppm

1168

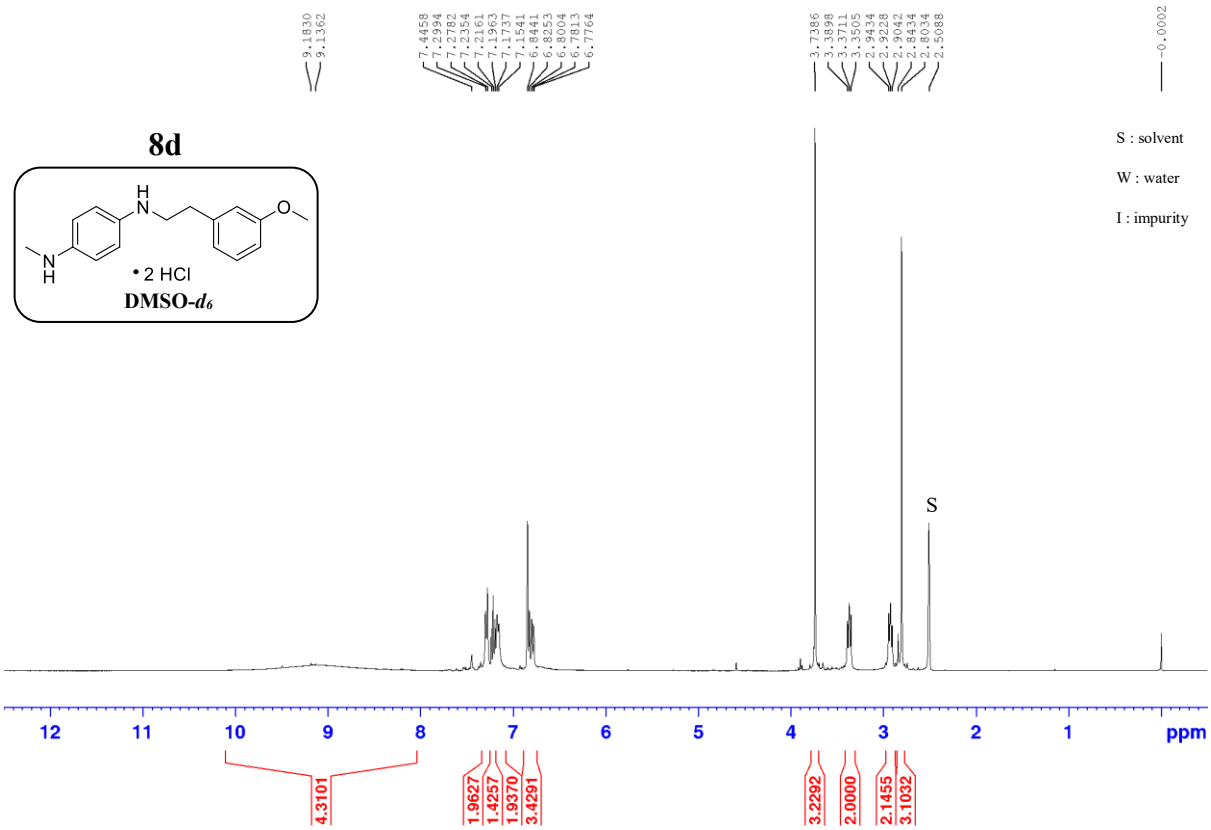
8d
• 2 HCl
DMSO-d6
S : solvent
W : water
I : impurity
S
ppm

1169

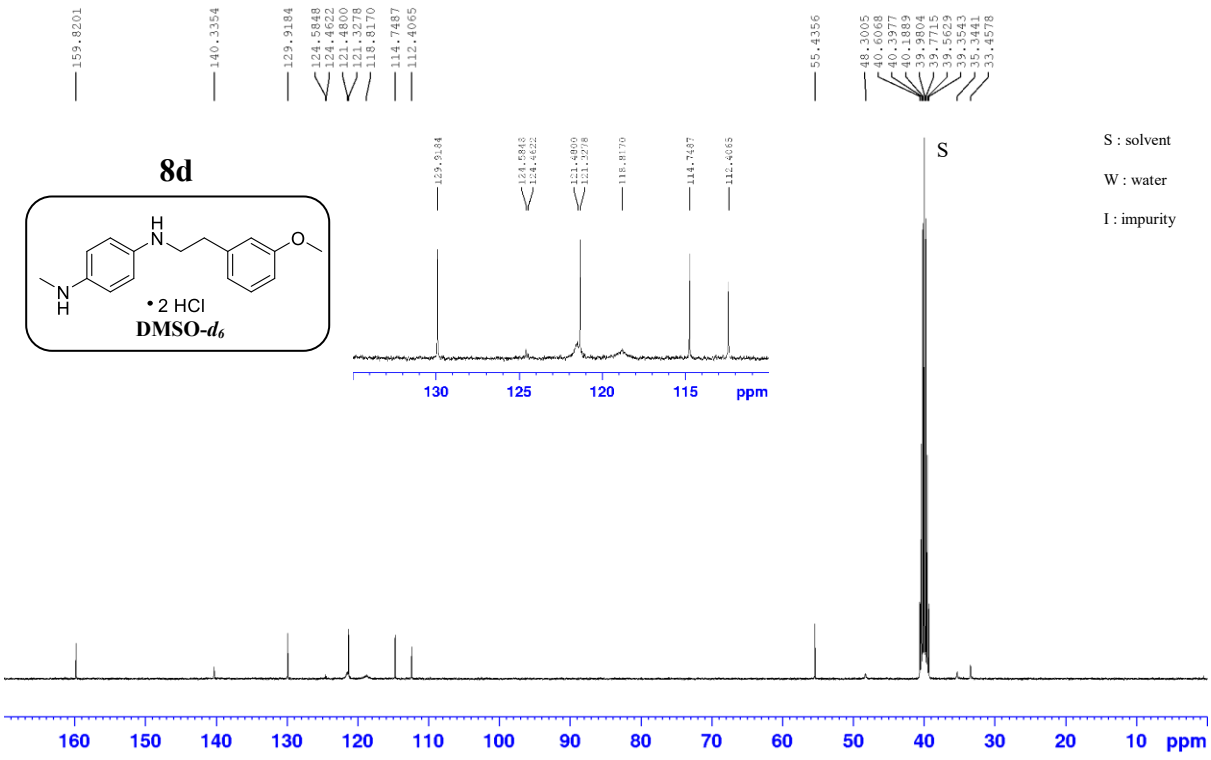
8d
• 2 HCl
DMSO-d6
S : solvent
W : water
I : impurity
S
ppm

1170

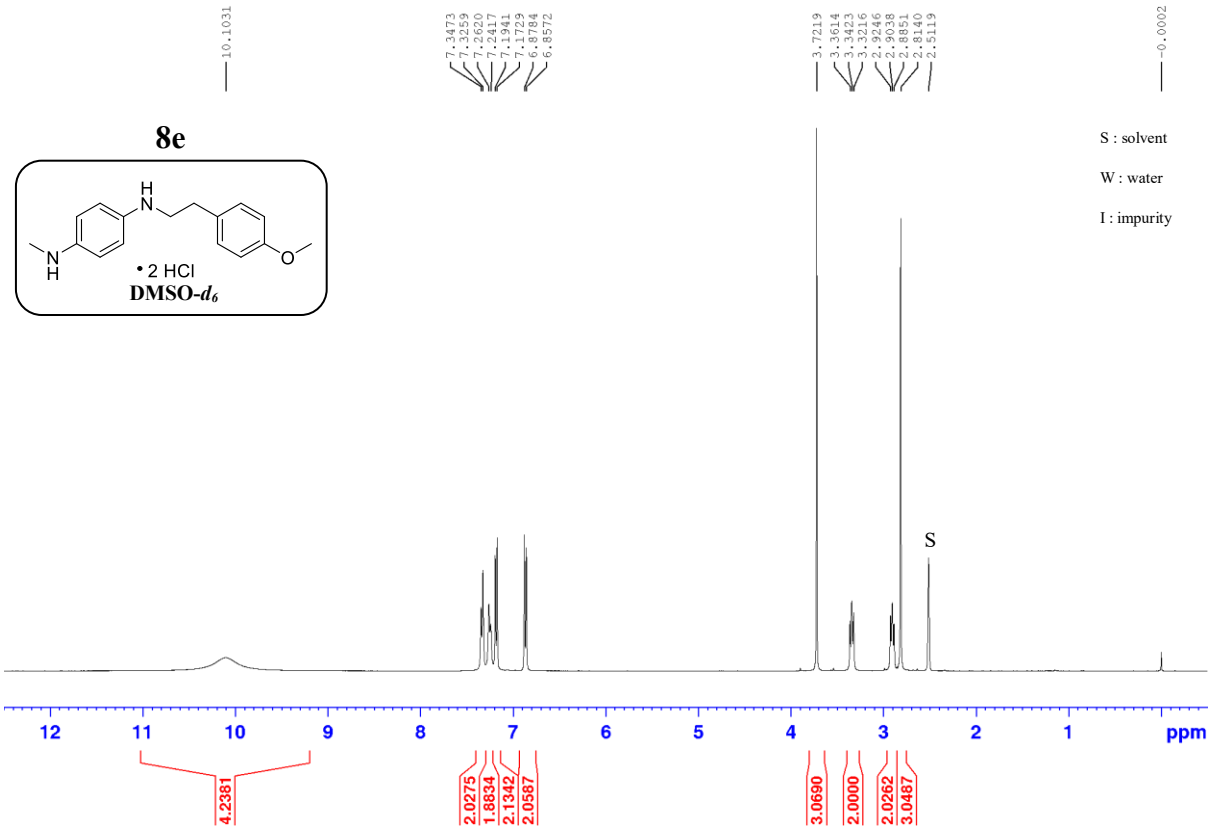
8e
• 2 HCl
DMSO-d_6
S : solvent
W : water
I : impurity
S
ppm

1171

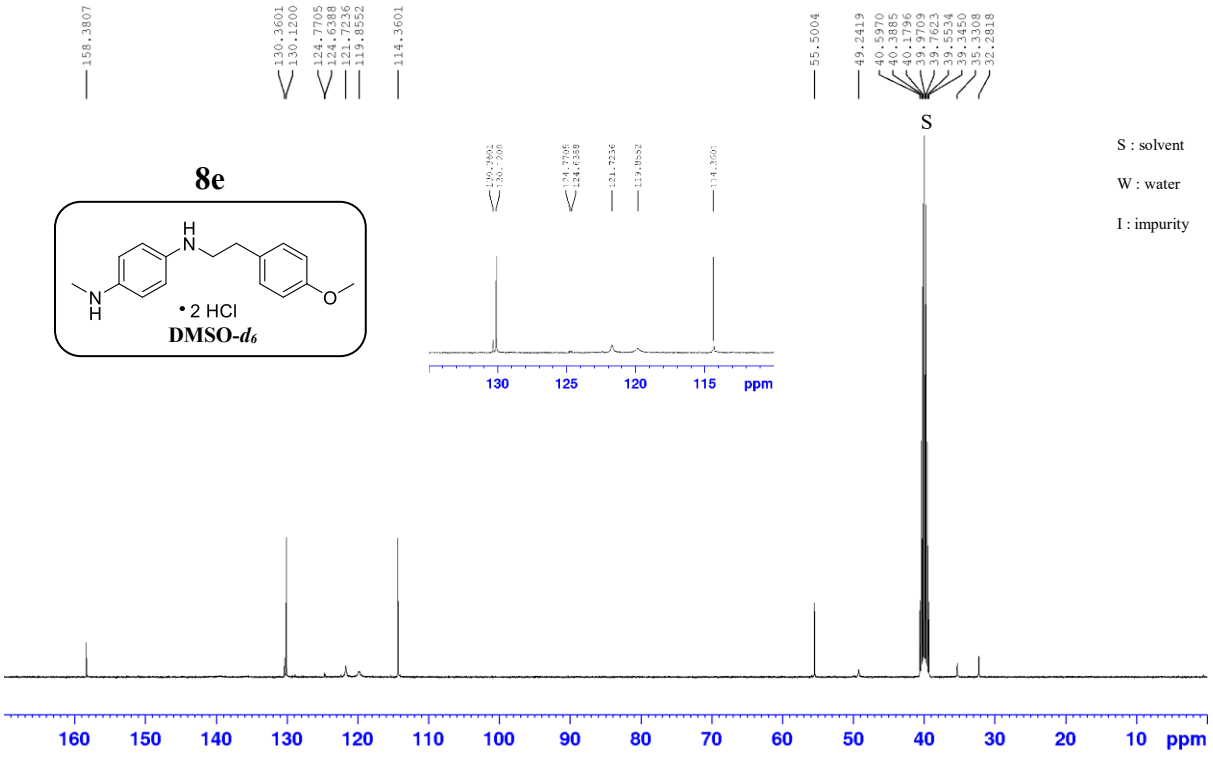
8e
• 2 HCl
DMSO-d_6
S : solvent
W : water
I : impurity
S
ppm

1172

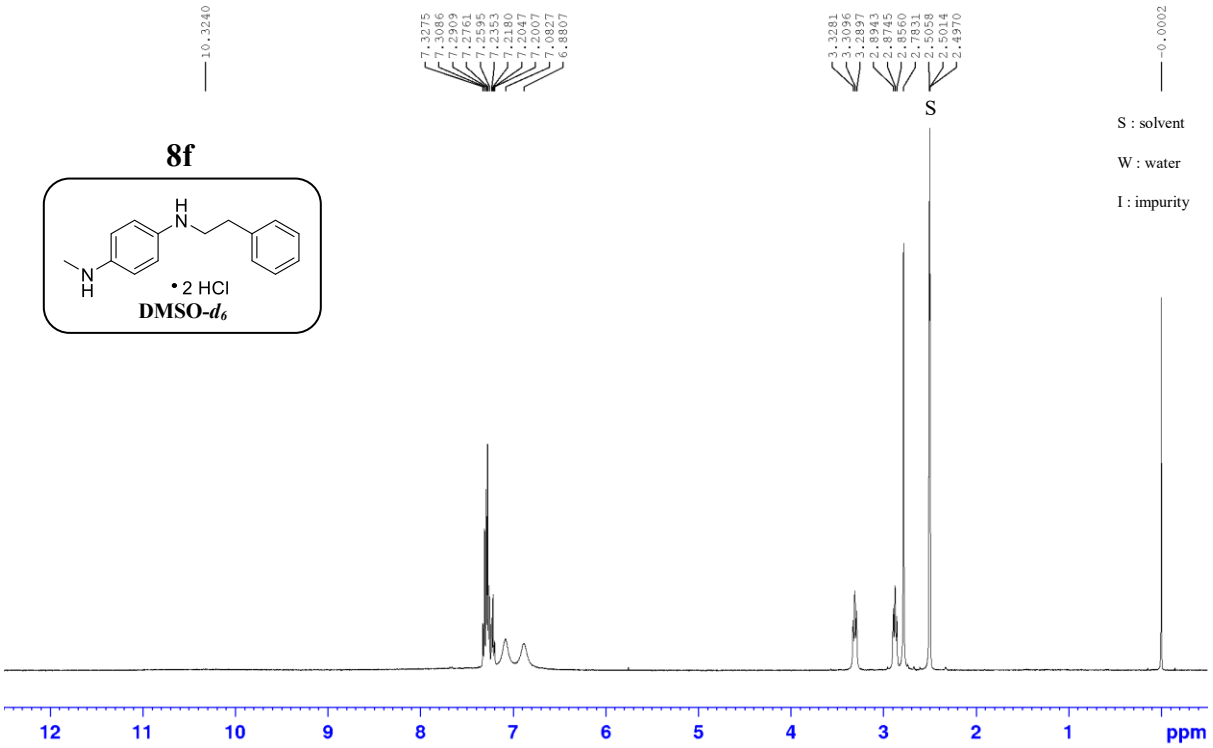
8f
• 2 HCl
DMSO-d_6
S : solvent
W : water
I : impurity
ppm

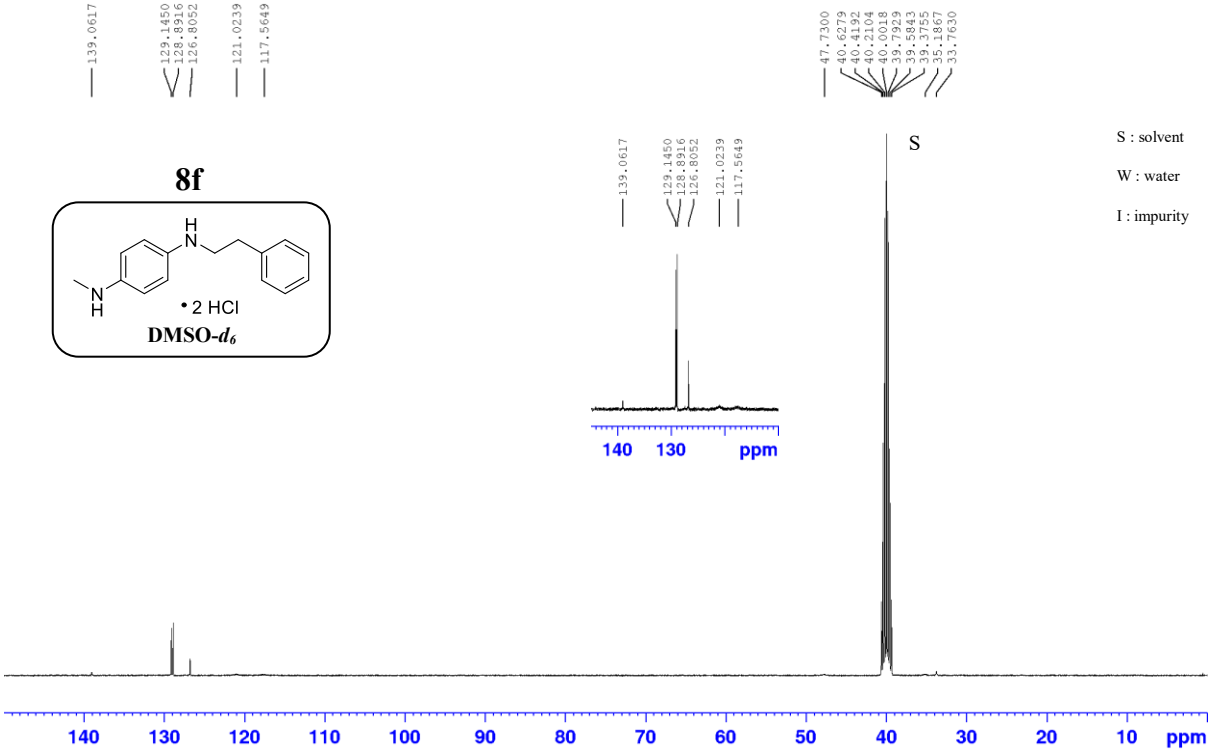
8f
• 2 HCl
DMSO-d_6
S : solvent
W : water
I : impurity
ppm

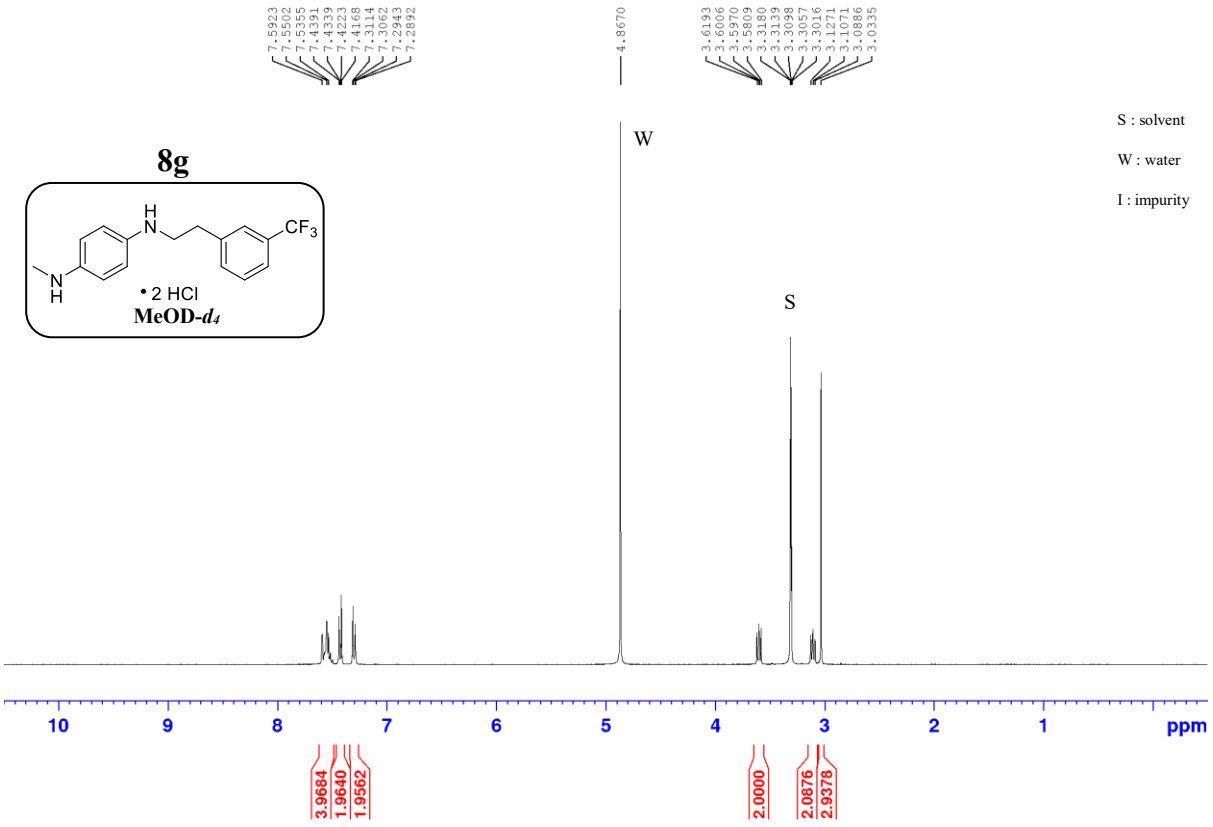
8g
H
N
CF3
N
H
• 2 HCl
MeOD-d4
7.5923
7.5502
7.5355
7.4391
7.4339
7.4223
7.4168
7.3114
7.3062
7.2943
7.2892
4.8670
3.6193
3.6006
3.5970
3.5809
3.3180
3.3139
3.3098
3.3057
3.3016
3.1271
3.1071
3.0886
3.0335
W
S
S : solvent
W : water
I : impurity
10
9
8
7
6
5
4
3
2
1
ppm
3.9684
1.9640
1.9562
2.0000
2.0876
2.9378

1176

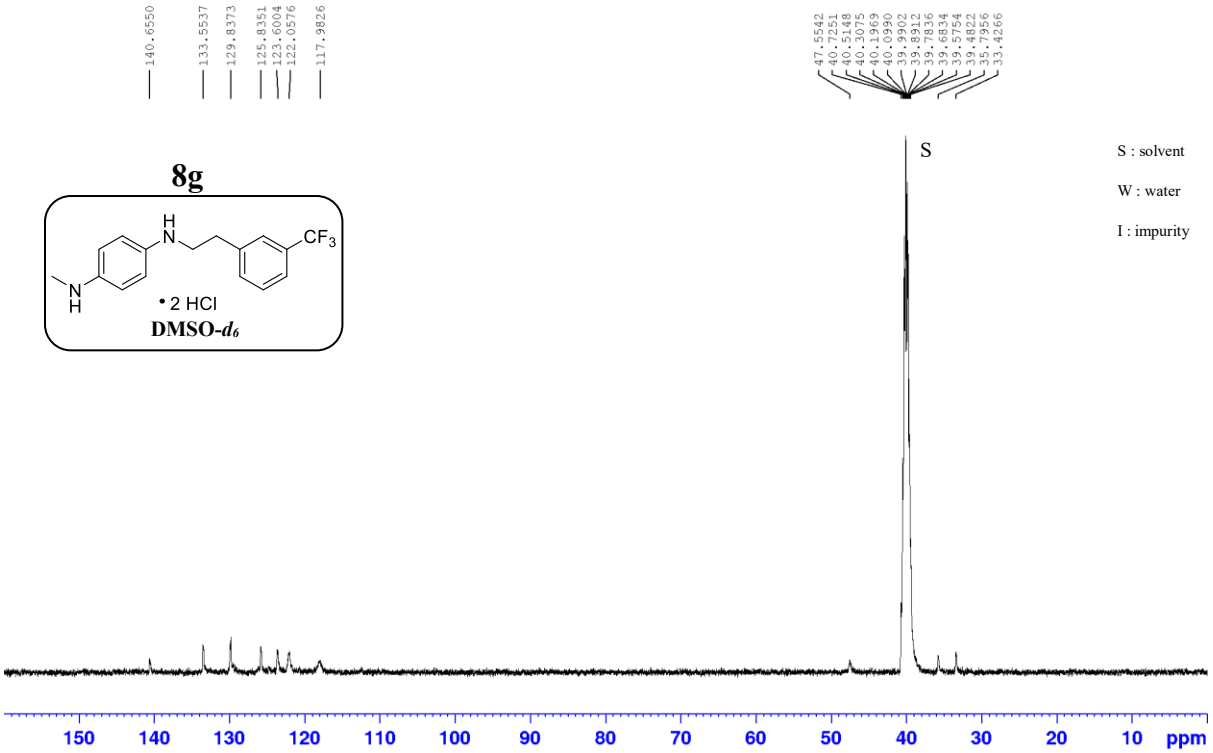
140.6550
133.5537
129.8373
125.8351
123.6004
122.0576
117.9826
47.5542
40.7251
40.5148
40.3075
40.1969
40.0990
39.9902
39.8912
39.7836
39.6834
39.5754
39.4822
35.7956
33.4266
8g
H
N
CF3
N
H
• 2 HCl
DMSO-d6
S
S : solvent
W : water
I : impurity
150
140
130
120
110
100
90
80
70
60
50
40
30
20
10
ppm

1177

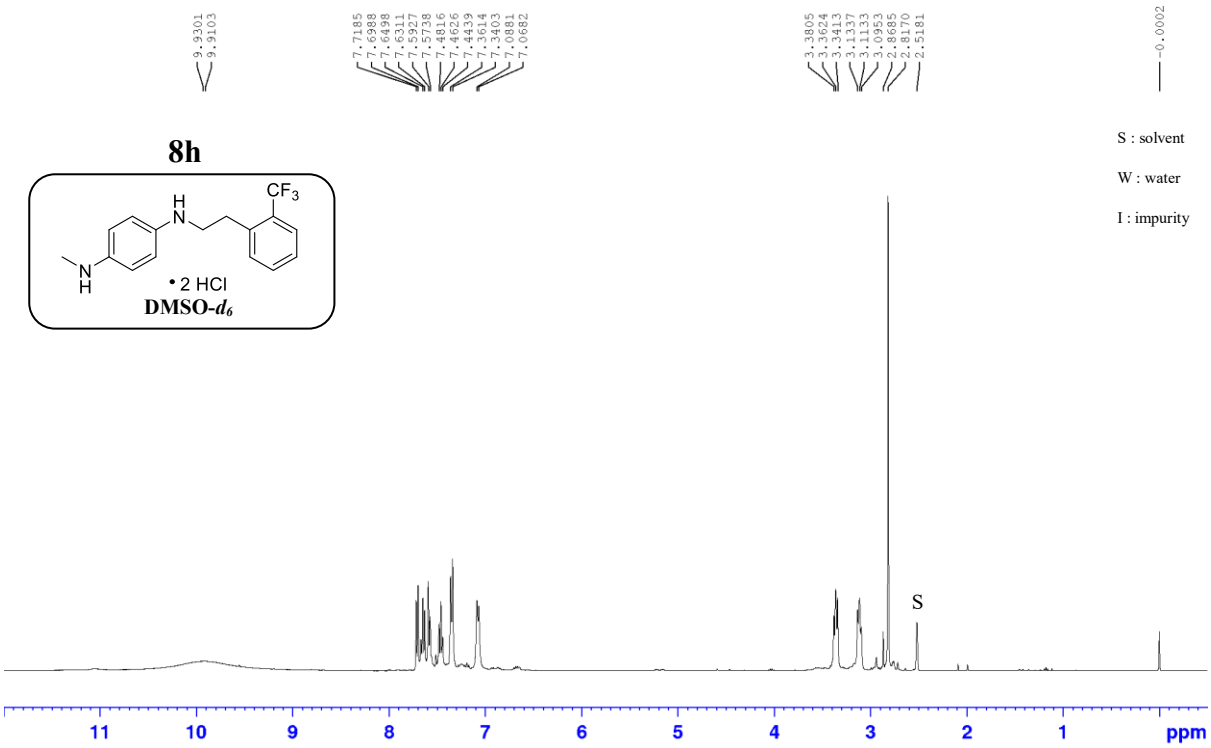
8h
CF3
H
N
N
H
• 2 HCl
DMSO-d6
S : solvent
W : water
I : impurity
S
ppm

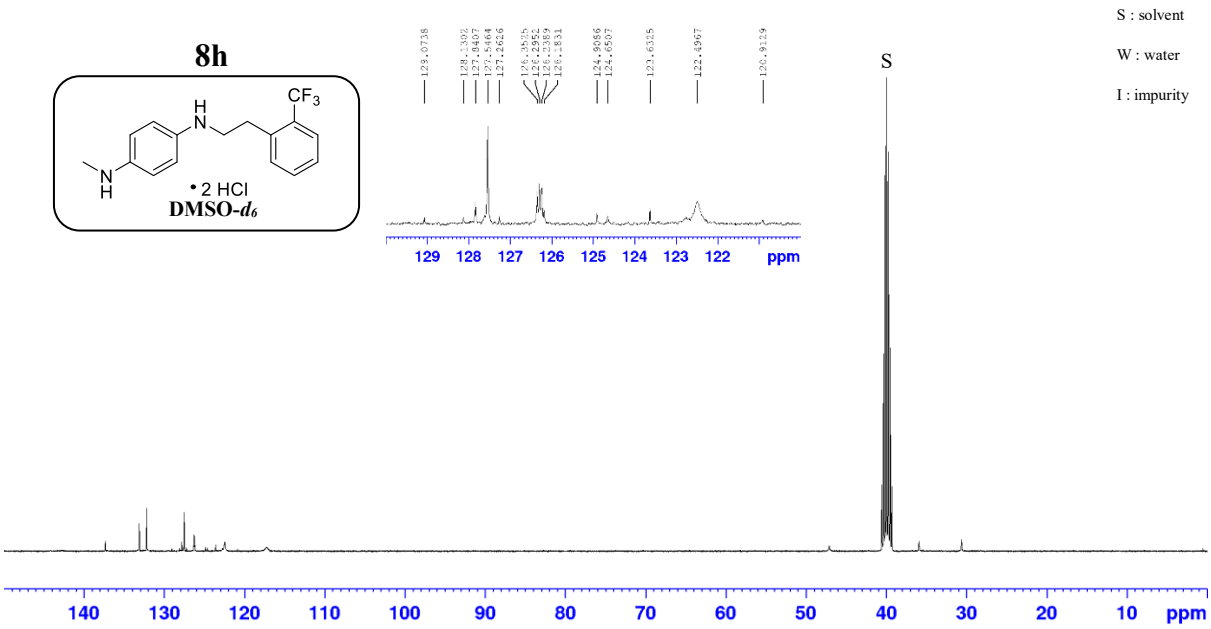
8h
CF3
H
N
N
H
• 2 HCl
DMSO-d6
S : solvent
W : water
I : impurity
S
ppm

HPLC Traces of synthesized compounds

Compound 7b

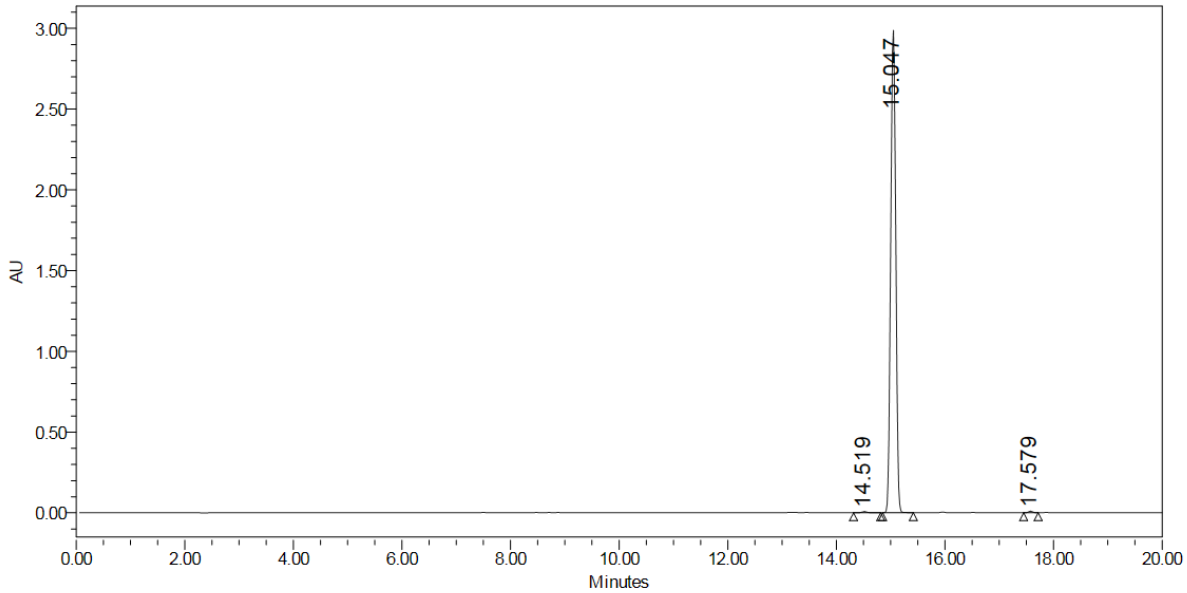

	RT	Area	% Area	Height
1	14.519	45807	0.24	6617
2	15.047	19362637	99.49	2981533
3	17.579	52501	0.27	9341

Compound 7c

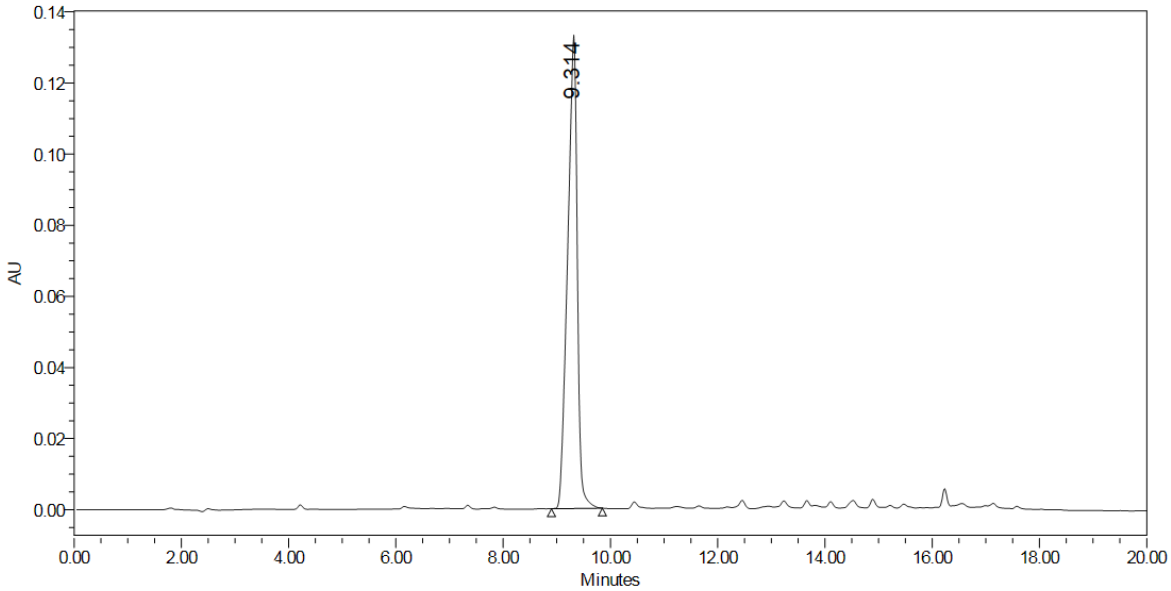

	RT	Area	% Area	Height
1	9.314	1659615	100.00	133056

Compound 7d

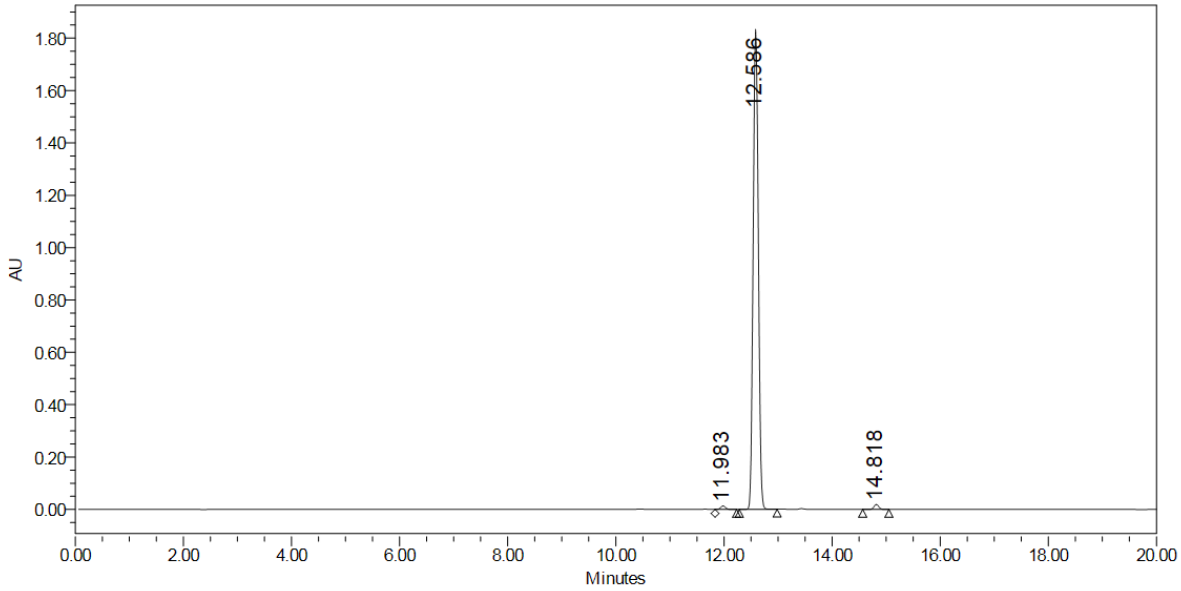

	RT	Area	% Area	Height
1	11.983	83559	0.68	13488
2	12.586	12136302	98.37	1830201
3	14.818	117815	0.95	18911

Compound 8a (KDS12017)

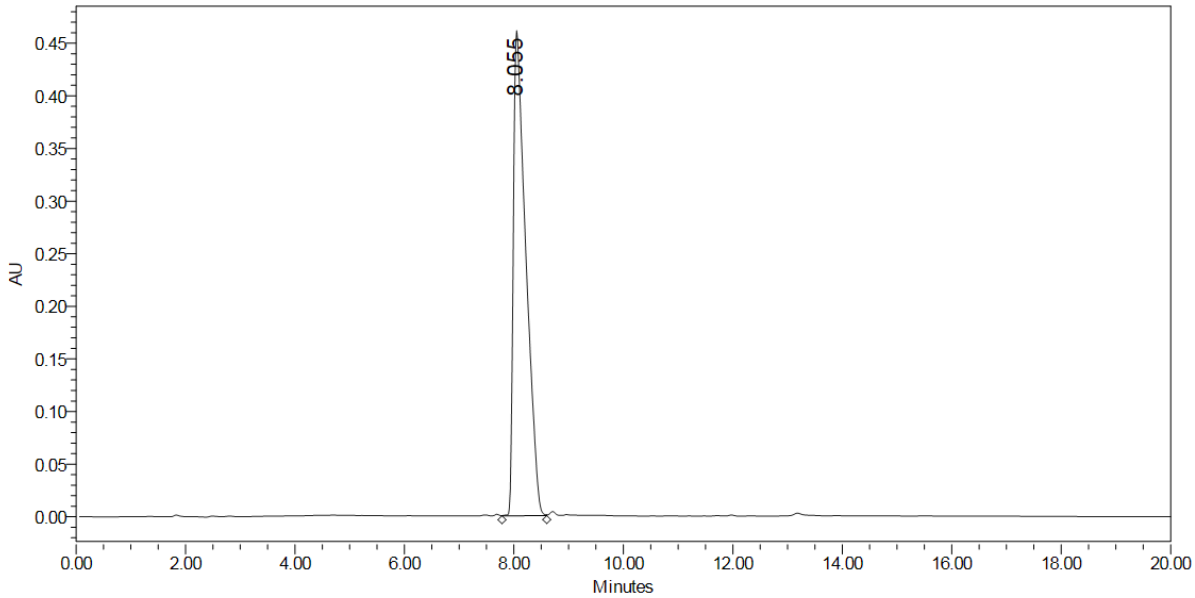

	RT	Area	% Area	Height
1	8.055	7308882	100.00	461824

Compound 8b (KDS12008)

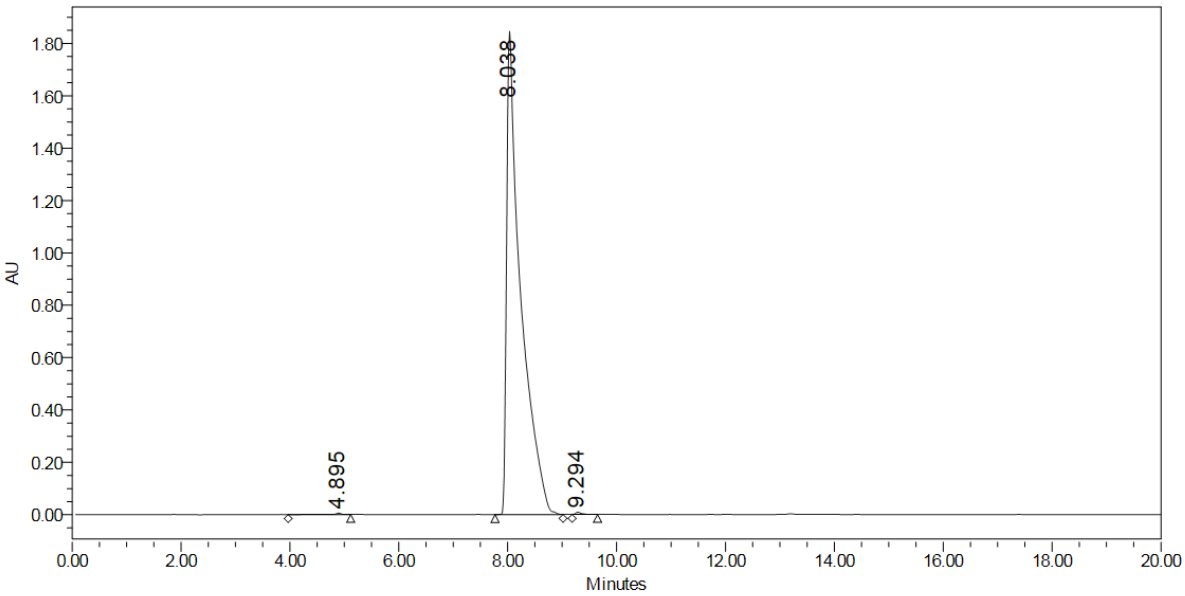

	RT	Area	% Area	Height
1	4.895	47509	0.14	4959
2	8.038	33161572	99.67	1848546
3	9.294	63231	0.19	8646

Compound 8c (KDS12025)

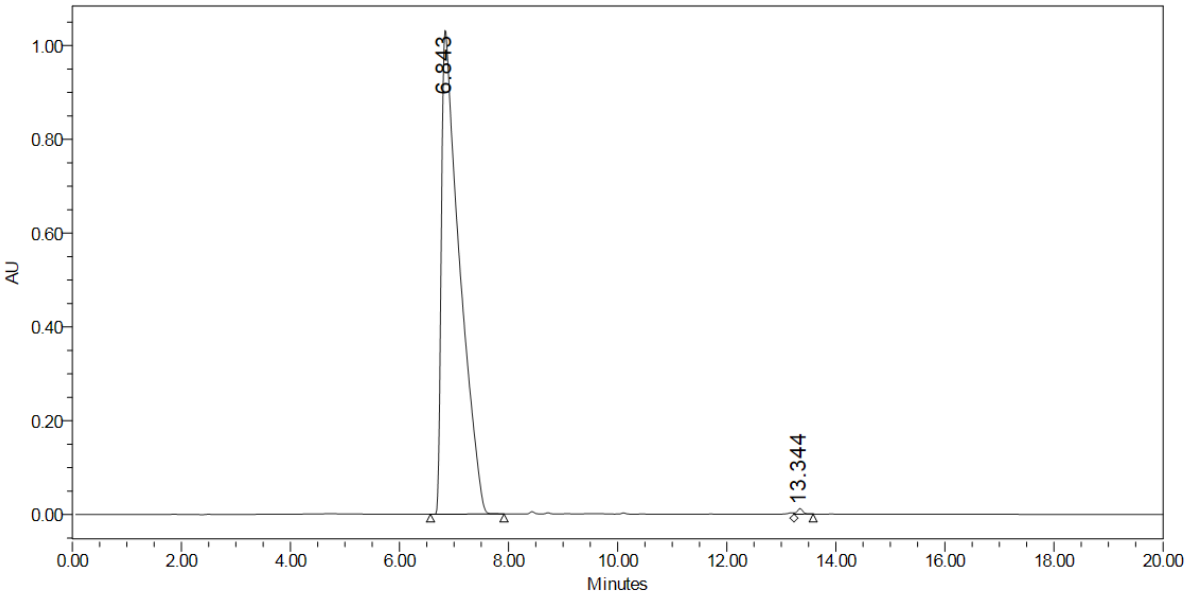

	RT	Area	% Area	Height
1	6.843	23825886	99.65	1037022
2	13.344	83202	0.35	11704

Compound 8d

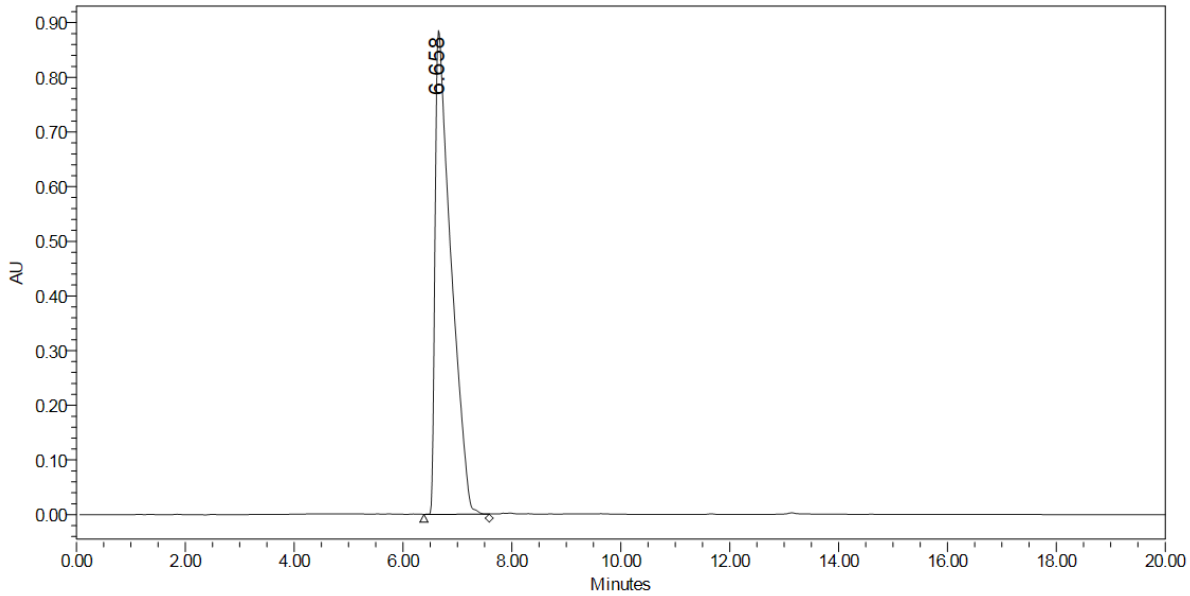

	RT	Area	% Area	Height
1	6.658	17921279	100.00	889249

Compound 8e

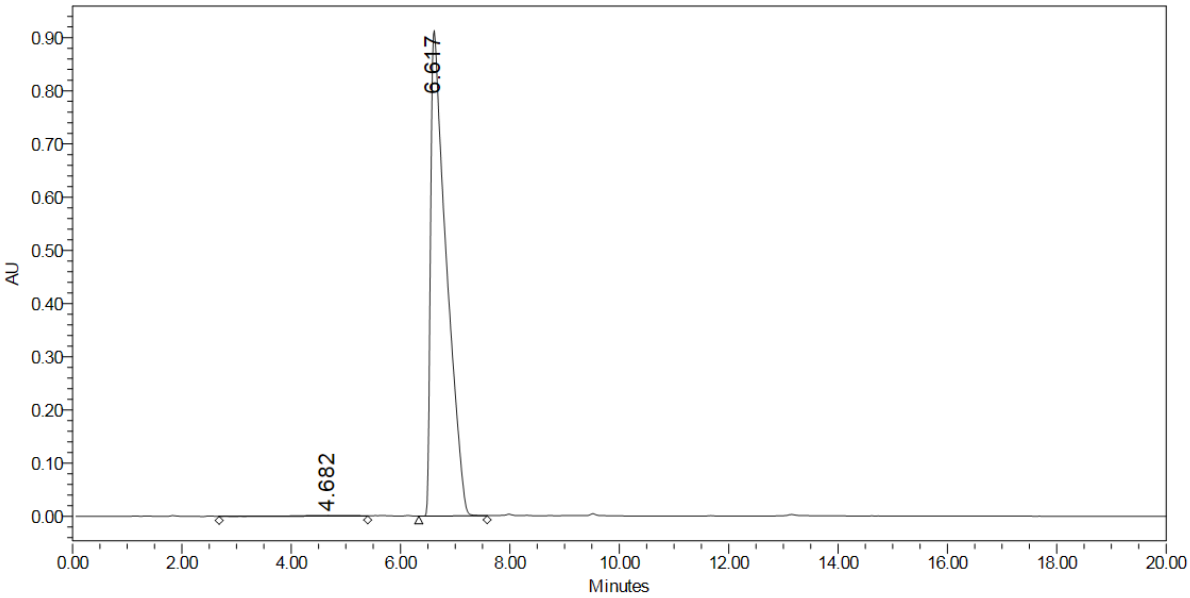

	RT	Area	% Area	Height
1	4.682	106520	0.58	1134
2	6.617	18193332	99.42	913108

Compound 8f

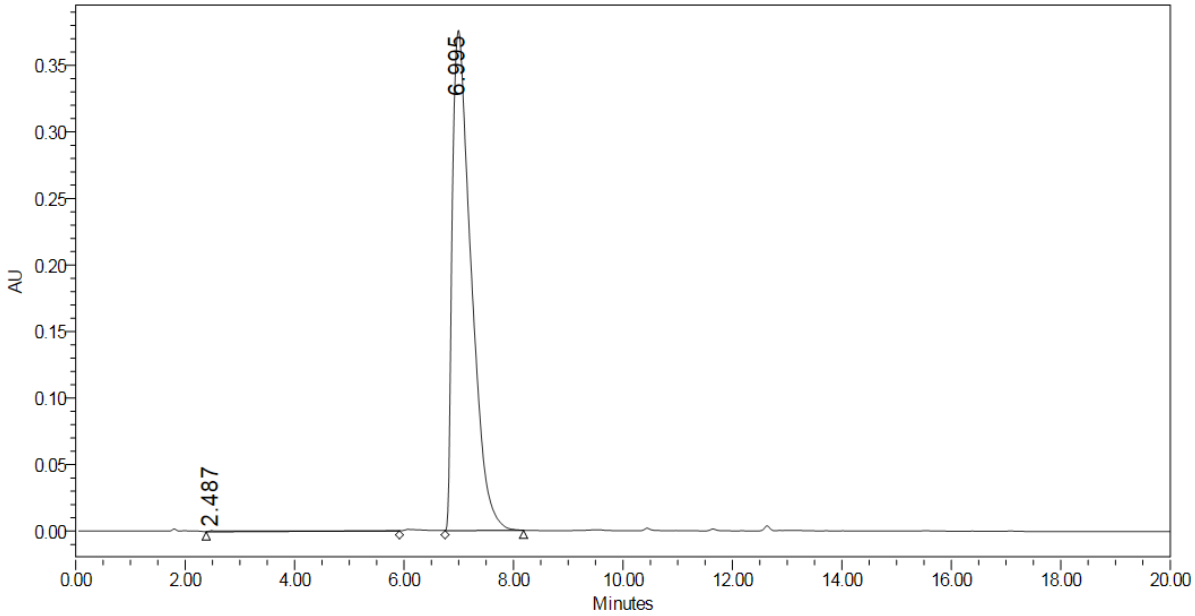

	Peak Name	RT	Area	% Area	Height
1	Peak1	1.502			
2		2.487	50422	0.56	775
3		6.995	8973832	99.44	376124
4	Peak2	10.350			

Compound 8g

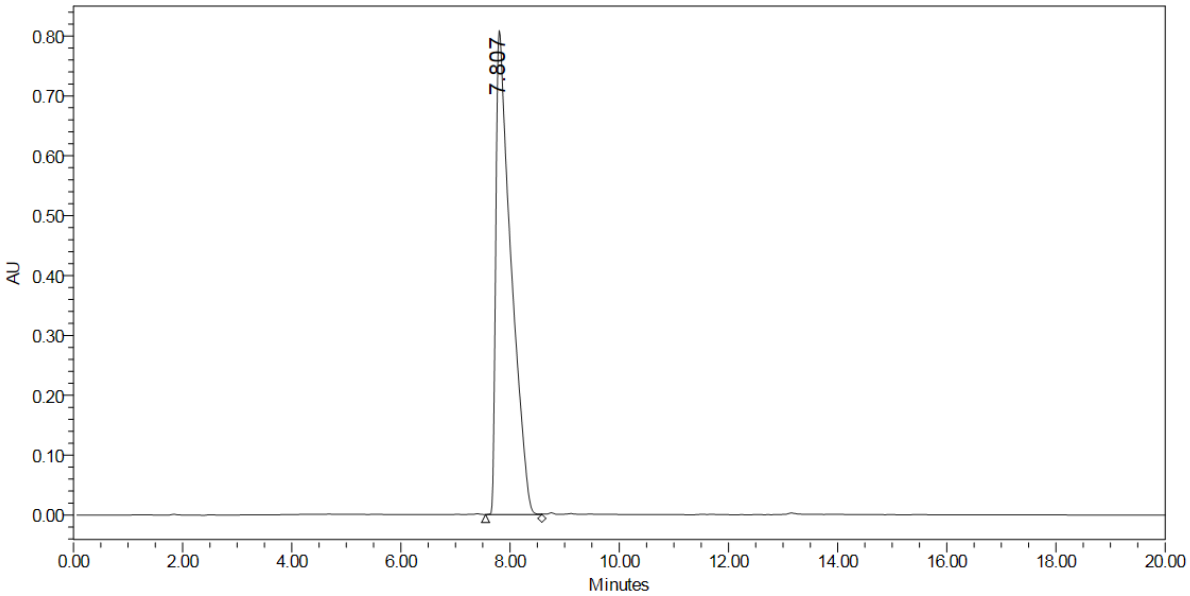

	RT	Area	% Area	Height
1	7.807	15565885	100.00	811441

Compound 8h

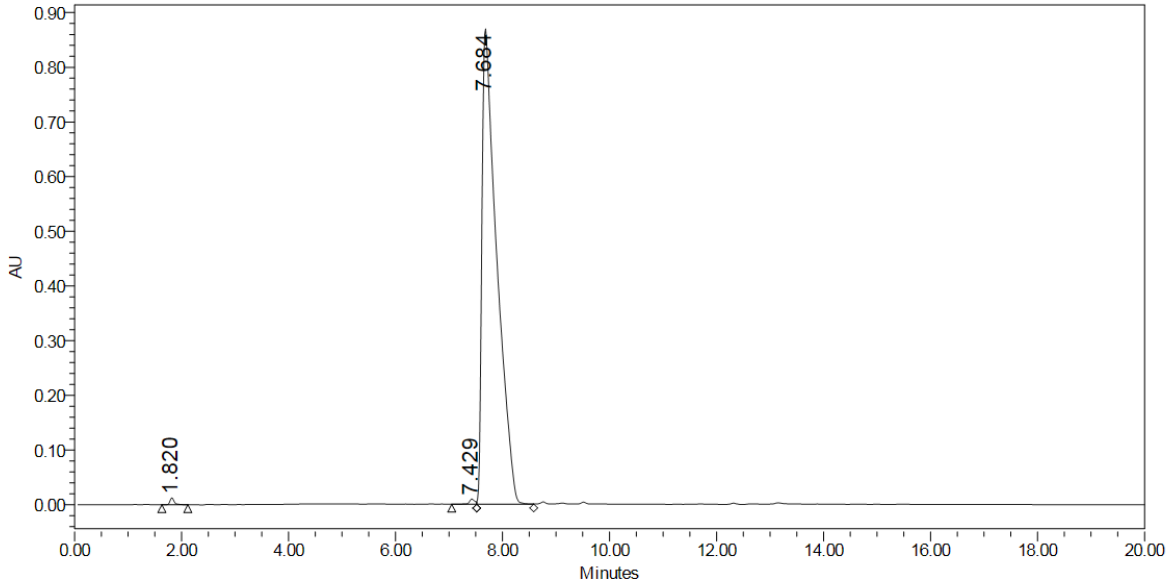

	RT	Area	% Area	Height
1	1.820	68874	0.41	12451
2	7.429	66757	0.40	9363
3	7.684	16689563	99.19	869503